crystals

MDPI

Review

Dislocations and Plastic Deformation in MgO Crystals: A Review

Jonathan Amodeo [1,*], Sébastien Merkel [2,3], Christophe Tromas [4], Philippe Carrez [2], Sandra Korte-Kerzel [5], Patrick Cordier [2] and Jérôme Chevalier [1]

1 Université de Lyon, INSA-Lyon, CNRS, MATEIS UMR5510, F-69621 Villeurbanne, France; jerome.chevalier@insa-lyon.fr
2 Université de Lille, CNRS, INRA, ENSCL, UMR 8207-UMET-Unité Matériaux et Transformations, F-59000 Lille, France; sebastien.merkel@univ-lille1.fr (S.M.); philippe.carrez@univ-lille1.fr (P.C.); patrick.cordier@univ-lille1.fr (P.C.)
3 Institut Universitaire de France, F-75005 Paris, France
4 Institut Pprime, UPR 3346 CNRS, Université de Poitiers, ENSMA, Département de Physique et Mécanique des Matériaux, SP2MI Bd Marie et Pierre Curie BP 30179, F-86962 Futuroscope Chasseneuil CEDEX, France; christophe.tromas@univ-poitiers.fr
5 Institute of Physical Metallurgy and Metal Physics, RWTH Aachen University, Kopernikusstr. 14, 52074 Aachen, Germany; Korte-Kerzel@imm.rwth-aachen.de
* Correspondence: jonathan.amodeo@insa-lyon.fr; Tel.:+33-(0)4-7243-8235

Received: 29 March 2018; Accepted: 10 May 2018; Published: 31 May 2018

check for updates

Abstract: This review paper focuses on dislocations and plastic deformation in magnesium oxide crystals. MgO is an archetype ionic ceramic with refractory properties which is of interest in several fields of applications such as ceramic materials fabrication, nano-scale engineering and Earth sciences. In its bulk single crystal shape, MgO can deform up to few percent plastic strain due to dislocation plasticity processes that strongly depend on external parameters such as pressure, temperature, strain rate, or crystal size. This review describes how a combined approach of macro-mechanical tests, multi-scale modeling, nano-mechanical tests, and high pressure experiments and simulations have progressively helped to improve our understanding of MgO mechanical behavior and elementary dislocation-based processes under stress.

Keywords: MgO; dislocations; mechanical properties; nano-mechanics; multi-scale modeling; extreme conditions

1. Introduction

MgO is a well-known crystalline ceramic, maybe the simplest one, and its mechanical properties were widely investigated during the second half of the 20th century, mainly at the macroscopic scale. In this review, we emphasize how more modern methods, e.g., multi-scale modeling, nano-indentation and high-pressure experiments, lead to significant advances in our understanding of the plasticity of MgO. For example, atomic scale simulations in MgO allow characterizing pressure, temperature and strain-rate controlled transitions in plasticity processes responsible for viscosity variations in the deep Earth. At the same time, recent experimental developments such as testing at the nano-scale allowed investigating dislocation nucleation processes in MgO, opening new routes toward ultra-hard ceramics fabrication. These recent and exciting technical developments allow theorists and experimentalists to work even more closely together.

The article presents past and current progresses on dislocation and plasticity understanding in MgO (and related ceramics) based on several technical points of view. An effort was made to parse various fields of applications such as mechanical engineering, theoretical physics, materials science as

WD EX1058
Western Digital v IP Bridge
Page 1

well as geosciences, equally represented through experimental and theoretical case studies. The article is organized as follows:

- In Section 2, basic knowledge on MgO plasticity is described based on an exhaustive literature review of macro-mechanical testing. Lattice structure and slip systems are introduced as well as the main mechanical properties of MgO based on constant strain-rate and creep experiments.
- In Section 3, we focus on multi-scale modeling of MgO plasticity. This section relies on atomic scale simulations (dislocation core modeling) and their implications for large scale simulations such as dislocation dynamics and crystal plasticity.
- In Section 4, recent improvements in nano-mechanical testing, i.e., nano-indentation, micro- and nano-compression, are introduced. Special attention will be paid on elementary dislocation processes occurring in the small interrogated volumes.
- In Section 5, the role of high pressure on dislocations and MgO plasticity is detailed. Based on both modeling and experimental approaches, we describe how pressure affects basic deformation processes in MgO with implications in both materials sciences and geosciences.

The knowledge on MgO mechanical properties recently reached a focal point in which dislocations properties at different scales play a key role. From the atoms to the polycrystal, experimental and numerical investigations enable multi-scale crossed-connections that drastically multiply the field of applications of this new knowledge to the entire class of ceramic materials.

2. Mechanical Properties of MgO Single Crystal: The Contribution of Macro-Mechanical Tests

MgO is an ionic ceramic which is mainly used for its refractory properties in furnaces and flame retardants as well as a compound for some technical ceramics for the construction industry (e.g., cements). Moreover, MgO is also a model material for the investigation of plastic deformation and dislocation mobility in ionic ceramics. The very first studies focusing on dislocation traces close to a micro-indent were performed in the 1950s [1]. These years marked the opening of a new field of research with the refined analysis of dislocation-based deformation processes in ionic crystals, especially those with relatively simple crystalline structure.

2.1. Lattice, Dislocations and Slip Systems in MgO

MgO atomic stacking is characterized by the B1 cubic crystalline structure (space group $Fm\overline{3}m$) that is also called the rock-salt (NaCl) structure. Its lattice parameter is about 4.21 Å at ambient conditions and its atomic structure is made of oxygen and magnesium atoms spread by half the diagonal of the cube. The B1 crystal structure can be described as two entangled anionic and cationic fcc sub lattices (see Figure 1a).

Unlike the widespread belief that ceramics, including MgO, are too brittle to deform by anything other than cracking, they may indeed also deform plastically by dislocation glide or climb. This controversial affirmation is particularly true in single crystals assuming both limited plastic and fracture strains. Furthermore, the *dense planes and directions* paradigm that usually rules slip system definition does not apply for oxides and especially not for the MgO B1 structure that is characterized by an alternative sequence of ionic and cationic {111} planes. In ionic crystals, an additional prerequisite is deduced from the impossibility of shearing planes that bring same charge sign ions close together. This explains why dislocation glide in MgO is localized in less dense {110} or {100} slip planes with ½<110> Burgers vectors, as shown Figure 1 [2–4].

Whatever the temperature range, there is a vast amount of valuable data about <100>-oriented single crystals available in the literature. This is due to {100} cleavage planes that facilitate such sample preparation. Hence, compression tests and critical resolved shear stresses (CRSS) focusing on {110} slip are often shown for a wide range of temperatures. It remains challenging, however, to obtain single-crystal deformation data for {100} slip for which sample preparation is more difficult.

WD EX1058
Western Digital v IP Bridge
Page 2

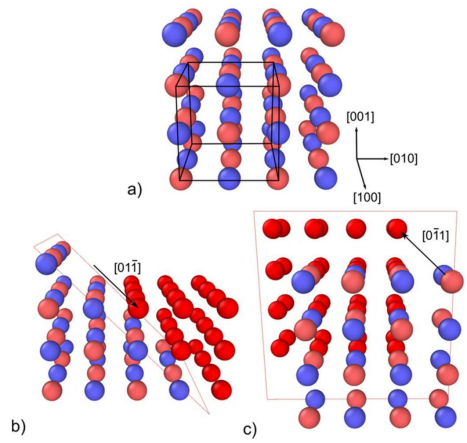

Figure 1. (**a**) Perspective view of the MgO crystalline structure. The unit cell is drawn with black lines and the crystal is oriented along the cubic orientation. (**b**,**c**) Illustrations of the shearing process for the (**b**) ½<110>{110} and (**c**) ½<110>{100} slip systems. The same orientation is used and the atoms displaced during the shearing process are labeled in red. Black arrows refer to typical Burgers directions.

Dislocations slip systems in MgO were investigated using ex situ atomic force and transmission microscopy. They are referenced in Table 1. In the study of Hulse and collaborators, the authors showed that CRSS are larger in ½<110>{100} than in ½<110>{110} slip systems for temperatures ranging from 300 K to 1500 K [5]. This study emphasizes that only four out of six ½<110>{110} slip systems are effective under <100> and <110> compression, with Schmid factors of about 0.5 and 0.25, respectively. Investigating the influence of orientation and anisotropy properties, the authors underline that the compressive yield stress is twice as high for orientations with 0.25 Schmid factors verifying the validity of the Schmid law for MgO. This study does not show any evidence of dislocation slip in ½<110>{111} slip systems. Schmid factors for {110}, {100} and {111} modes and <100>, <110> and <111> compression axis (CA) are shown Table 2.

Table 1. ½<110>{110} and ½<110>{100} slip systems in MgO.

Index	Plane	$\vec{b}$	Index	Plane	$\vec{b}$
1	$(\bar{1}10)$	$\frac{1}{2}[110]$	7	(001)	$\frac{1}{2}[110]$
2	(110)	$\frac{1}{2}[1\bar{1}0]$	8	(001)	$\frac{1}{2}[1\bar{1}0]$
3	$(0\bar{1}1)$	$\frac{1}{2}[011]$	9	(100)	$\frac{1}{2}[011]$
4	(011)	$\frac{1}{2}[01\bar{1}]$	10	(100)	$\frac{1}{2}[01\bar{1}]$
5	$(\bar{1}01)$	$\frac{1}{2}[101]$	11	(010)	$\frac{1}{2}[101]$
6	(101)	$\frac{1}{2}[10\bar{1}]$	12	(010)	$\frac{1}{2}[10\bar{1}]$

Table 2. Schmid factors in main ½<110>{110} and ½<110>{100} slip modes and additional ½<110>{111} for compression axis CA = <100>, <110> and <111>.

CA	½<110>{110}	½<110>{100}	½<110>{111}
<100>	0.5 for 4/6 systems	0 for all systems	$\sqrt{6}/6$ (~0.41) for 8/12 systems
<110>	0.25 for 4/6 systems	$\sqrt{2}/4$ (~0.35) for 4/6 systems	$\sqrt{6}/6$ (~0.41) for 4/12 systems
<111>	0 for all systems	$\sqrt{2}/3$ (~0.47) for 3/6 systems	$\sqrt{6}/9$ (~0.27) for 6/12 systems

Etched surface analyses were also performed to characterize slip localization [6–8]. In the study of Day et al. [7], dislocation slip is confined in a single slip system between room temperature and 1000 K. From 1000 K to 1400 K, two conjugate ½<110>{110} slip systems (with orthogonal slip planes)

WD EX1058
Western Digital v IP Bridge
Page 3

interpenetrate and produce the strain. This configuration is also mentioned in the work of Copley [8]. In both temperature regimes, the initial distribution of dislocations plays a key role on the primary slip plane activity. At higher temperatures, the authors mentioned the activity of both 90° and 60°/120° slip system configurations. In all configurations, TEM analyses show an increase of the dislocation density along the <111> directions, typical of {110} slip plane intersections [9].

Contrary to metallic fcc structures, very few studies mention ½<110>{111} dislocation slip in MgO single crystals [10,11]. On the other hand, dislocation cross-slip was observed in {112} and {122} planes during in situ TEM tests [12]. These observations were confirmed in nano-indentation tests [13] considering confined deformation at particularly high-stress under the indenter (see Section 4).

2.2. Critical Resolved Shear Stress (CRSS)

Hulse, Copley and Pask performed a set of compression tests on single crystals investigating the CRSS and deformation processes in both slip modes [5,8,14]. Temperatures investigated range from 100 K up to 1400 K for the ½<110>{110} slip systems. In their analysis, the authors discuss the role of thermally-activated processes (e.g., lattice friction, impurities) on CRSS variations. The reader can refer to Ref. [8] for a detailed overview of this work.

The study of Appel and Wielke focuses on CRSS measurements in the ½<110>{110} slip systems down to 4 K [15]. The authors emphasize that, even if impurities (especially iron) interact with defects restricting dislocation glide, they cannot explain alone the non-linear variations of CRSS with temperature and thus assume a Peierls, lattice-friction, mechanism to proceed. The lowest temperatures investigated lead to stresses of about 118 MPa (T = 4.2 K) and 132 MPa (T = 5.6 K). Extrapolating Appel and Wielke data, one can evaluate a Peierls stress of about 150 MPa in ½<110>{110}. While the uncertainty is of the order of a few tens of MPa close to 0 K, this study confirms this value as an approximate proxy of the Peierls stress for ½<110>{110} slip in MgO, as already proposed in previous studies [16,17].

Several additional studies addressed the effect of temperature on the CRSS for the ½<110>{110} slip systems [18–22] while only few datasets focus on ½<110>{100} [5,8,22]. These data are shown in Figure 2. Several interpretations can be made from this master plot. First, one can confirm Appel and Wielke [15] hypothesis stating that deformation is controlled by lattice friction at low temperature (T < 100 K) as most of the experiments show significant non-linear variations of the CRSS over few tens of MPa, which is the signature of a Peierls mechanism. Nevertheless, the data scatter observed at intermediate temperatures (100 K < T < 600 K) might be the sign of other thermally activated processes such as dislocation versus impurities interactions or precipitate hardening. This point will be discussed later. At high temperature (T > 600 K), forest dislocation interactions lead to a stress plateau of about 15 MPa at least up to 1900 K. Concerning the ½<110>{100} hard mode, besides wider stress variations, no conclusion can be made about ½<110>{100} Peierls stress from macro-mechanical tests. A simple guess larger than 1 GPa can be inferred from Barthel's data extrapolation.

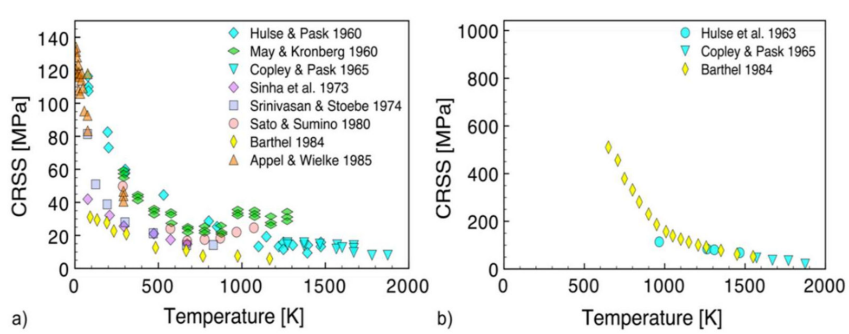

Figure 2. CRSS for (**a**) ½<110>{110} and (**b**) ½<110>{100} slip systems in MgO single crystal under compression. Details about impurity contents can be found in original articles and in Ref. [23].

WD EX1058
Western Digital v IP Bridge
Page 4

2.3. Temperature-Dependent Dislocation Microstructures

Based on the CRSS master plot in Figure 2, one can define two main deformation regimes for MgO single crystal. At low to intermediate temperatures, MgO deformation is in a thermally-activated, "bcc-like", regime characterized by wide CRSS variations for which both lattice and solute frictions influence the deformation. At high-temperature, the mechanical response of MgO is described by a "fcc-like" regime, where dislocation interactions lead to a stress steady-state (or weak variations). Based on the metallic alloys terminology, an athermal transition temperature T_a that emphasizes the transition between the thermally-activated regime ($T < T_a$) and the so-called athermal regime ($T > T_a$) is defined. For ½<110>{110}, T_a ranges from 600 K to 800 K depending on the experimental dataset. CRSS vary less rapidly for ½<110>{100} slip systems and T_a > 1300 K.

Dislocation microstructures developed during single crystal compression tests were characterized using in situ TEM [24,25]. At room temperature, straight and long screw dislocations are observed in both the {110} and the {100} slip planes [24,26]. Their velocity is assumed to follow a stress-exponent [16,27] or an Arrhenius-like dependency [28,29]. This dislocation microstructure is typical of high lattice friction materials. Edge dislocations are shorter and glide at higher velocity when compared to screw. In MgO, they are generally observed during the first stage of deformation similarly to α-iron [30], except in the case of dipoles formation [25]. Beyond the transition temperature, dislocations exhibit a viscous behavior typical of fcc metals as shown, e.g., in the work of Clauer and Wilcox [10]. Both dislocation microstructures are illustrated on Figure 3.

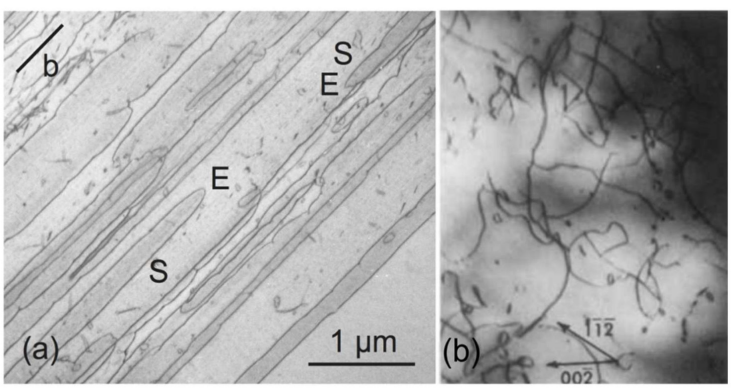

Figure 3. TEM micrographs of (**a**) room temperature dislocations extracted from a 45° shear band using the High-Voltage Electron Microscope (HVEM). Dislocations are elongated along the screw direction. S, E and b refers to Screw, Edge and to the Burgers vector respectively. Image reproduced from Ref. [26] with the permission of Springer Nature; (**b**) [110] thin section, 1400 °C. The dislocation curvature is more isotropic when compared to room temperature. Image reproduced from Ref. [10] with the permission of John Wiley and Sons.

2.4. On the Role of Impurities and Heat Treatments on CRSS and Dislocation Mobility

Several studies refer to the influence of point defects on CRSS in MgO [8,14,18,20,21]. Generally, the CRSS increase in the intermediate range of temperature is justified by the impurities oxidation state [21,31,32] and their spatial distribution [1,33,34], both parameters being intrinsically linked to the heat treatment processed before deformation.

In the study of Gorum and collaborators [33], the authors investigate the role of iron on ½<110>{110} CRSS. Three main results can be emphasized: (i) For an as cast sample including 10 ppm of iron, the CRSS is of about 40 MPa at room temperature. For a 30 ppm sample, it is 140 MPa and increases up to 180 MPa for a concentration of about 3000 ppm. Therefore, we can conclude that, without heat treatment, MgO CRSS depend strongly on the impurities content (at room temperature); (ii) A heat treatment at 2000 °C on a sample containing 3000 ppm of iron deformed at

WD EX1058
Western Digital v IP Bridge
Page 5

room temperature leads to lower CRSS when compared to an as cast sample that contains only 30 ppm of iron. Furthermore, it increases its ductility; (iii) A faster cooling rate after heat treatment decreases the CRSS while increasing the sample ductility.

Obviously, heat treatment and cooling rate control the spatial distribution of impurities in crystalline materials. A slow cooling rate allows the impurities to drift toward dislocation and pin them. With a faster cooling rate, impurities are maintained in solid solution which limits the impurity hardening effect. For ceramics, this process was discussed by Johnston and Gilman [1]. In addition, several studies emphasize the role of heating atmosphere during heat treatment [21,32]. Indeed, a reductive atmosphere (e.g., argon gas) will favor divalent ions that are known to have a weaker strengthening effect than trivalent impurities, merely obtained when the heat treatment is performed in air.

In the early 1970s, the group of Messerschmidt (Halle, Germany) did an impressive work quantifying the interaction between dislocations and point defects, especially to interpret observations made in the High-Voltage Electron Microscope (HVEM) [12,24,35–42]. Among others, a model for point obstacle crossing activation energy is proposed [37] as well as a comparison between TEM observations and calculation of point defect distance distribution [43]. For an exhaustive review of this work, the reader can refer to the book by Messerschmid [26].

Several sets of experiments were proposed by Singh and Coble to investigate stress and temperature dependency of dislocation velocity in MgO [16,27]. One concerns *pure* samples with about 100 ppm impurities (including 20 ppm of iron). *Pure* samples were all subjected to a preliminary 40 h heat treatment in air at 1300 °C. Then, some of the samples were again heated at 1200 °C for one week under a reductive atmosphere to decrease the content of trivalent cations. These last are referred to as "*Pre*" while others are called "*Pox*". Finally, successive micro-indentations tests were performed to measure dislocation velocity at room, 100 °C and 150 °C temperatures. Results can be resumed as follows. First, the velocity of edge dislocations is always larger than the one of screw dislocations which confirms the aforementioned TEM studies. At room temperature, "*Pox*" samples are characterized by a lower dislocation velocity than "*Pre*" samples, even for comparable trivalent Fe ions concentrations (respectively, 19 and 6 ppm). These results show that "*Pox*" samples already contain a sufficient amount of Fe^{3+} ions for dislocation pinning confirming Gorum's hypothesis about the non-linear dependency of the dislocation velocity regarding the concentration of trivalent ions [33].

2.5. Strain Hardening in MgO Single Crystal

Dislocation-point defects interactions, dislocation dipoles and more generally dislocation reactions can lead to strain hardening in MgO single crystals. Hulse and Pask have shown that MgO single crystal can deform plastically down to very low temperatures, measuring a fracture strain of about 6% at 77 K [14]. Surface analyses emphasize 90° shear bands that confirm the joint activity of two conjugate ½<110>{110} slip systems as already observed in Day and Stokes' work [7]. While the hardening coefficient $\frac{\theta}{\mu}$ (where θ and μ are, respectively, the stress strain derivative and the shear modulus) ranges from ~200 to 1100 when increasing temperature up to 1273 K (see Figure 4), it remains constant (for a given temperature) up to the fracture strain. Similar compression tests were performed by Copley and Pask between 1273 K and 1873 K, with <100> and <111> compression axes. <100> tests show a decrease of θ attributed to high-temperature restoring processes such as cross-slip and dislocation climb.

WD EX1058
Western Digital v IP Bridge
Page 6

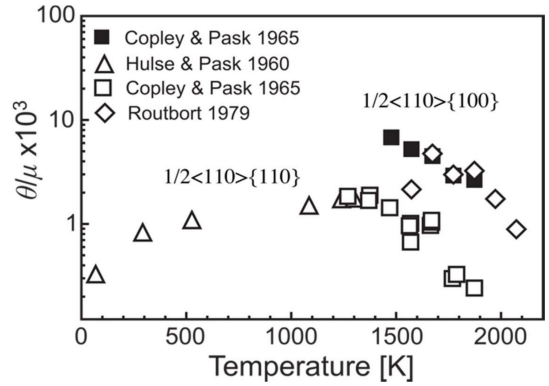

Figure 4. Strain hardening coefficient in MgO. White and black symbols refer to experimental data for the ½<110>{110} and ½<110>{100} slip modes respectively. Adapted from [8,14,44,45].

Up to highest temperatures, two conjugate ½<110>{110} slip planes control the deformation while four of the six slip systems have the same (maximum) Schmid factors. Therefore, it is assumed that two slip systems are surprisingly inhibited. On the other hand, dislocation interactions between 60°/120° slip systems are stronger than 90° reactions. The authors also refer to Kear's calculation about dislocation junction formation [46], i.e., two ½<110>{110} dislocations with 60°/120° oriented Burgers vectors can react and make a junction following, e.g., Equation (1).

$$\frac{1}{2}\left[\bar{1}01\right](101) + \frac{1}{2}\left[01\bar{1}\right](011) \rightarrow \frac{1}{2}\left[\bar{1}10\right](112) \quad (1)$$

The resulting dislocation is of edge character, aligned along one of the <111> directions and can eventually glide in {112} slip planes which were observed only under very high-stress conditions [13]. As dislocation junctions are obstacles to dislocation glide, shear bands observations can be interpreted by a joint process of a pair of conjugated slip systems producing deformation in the same time than making junctions, with remaining two least activated slip systems. While the decrease of θ at high temperature can be attributed to restoring processes, the similar trend at low temperature can only be justified by the weakening of the hardening processes.

<111> compression tests allow investigating strain hardening in ½<110>{100} slip systems. Results show higher value of θ when compared to {110} (5–10 times larger depending on temperature) but a similar trend against temperature variations (see Figure 4).

2.6. High-Temperature Creep of MgO

At high temperatures, solids can be deformed by creep, i.e., under a constant load, following the evolution of strain with time. The range of *high-temperatures* is conventionally considered to start at $0.5 \times T_m$ (T_m being the melting temperature). With a melting temperature close to 3100 K, MgO is a refractory material and some applications (material for crucibles) are a consequence of its stability (physical and chemical) at high temperature. Most creep tests were, as expected, performed at temperatures above $0.5 \times T_m$. However, very few were performed above $0.7 \times T_m$. Ruano and colleagues reviewed the creep behavior of MgO single crystals compressed along <100> [47]. Creep of MgO can be described by a power law with a stress exponent close to 5. A comparable behavior ($3.8 < n < 4.5$) was found for tensile creep tests of <110> single crystals between 1200 and 1500 °C [10]. Three-point bending tests on MgO single crystals lead to similar results with a slightly wider range ($4 < n < 7$, see [48]). It is to be noted that similar tests performed in Ref. [49] showed that the application of an electric field gives a transient acceleration of the creep rate. However, very few studies have considered explicitly the implication of charged species on the creep behavior. Recently, Mariani and collaborators [11] have shown using EBSD that dynamic recovery by sub-grain rotation is the main recrystallization mechanism in MgO single crystals deformed at

high strains. The activation enthalpy is usually reported to be in the range 320–400 kJ/mol. Under those conditions, the dislocation density ρ is found to scale with the applied stress σ following the equation $\rho \sim \sigma^m$ with $m = 1.4$ [50], or $m = 2.15$ [51]. At low stress (below 10 MPa) and usually above $0.6 \times T_m$, the creep rate of MgO single crystal may exhibit a stress dependence close to 1 [52]. Studies on polycrystals lead to comparable results with however a stress dependence closer to 3 [53–55]. In one case [54], a much smaller activation enthalpy was reported (213 kJ/mol) with a polycrystal characterized by a rather small grain size (12 μm). Given the importance of iron-bearing MgO (ferropericlase) in Earth sciences, several studies have also investigated the influence of this alloying element which does not seem to have a strong influence on creep properties in this temperature range, at least up to 20% content [56,57].

These parameters suggest that single crystal MgO deforms at high temperature through a dislocation creep mechanism. As described by Weertman, this creep regime involves dislocation glide, which controls the strain-rate by inducing recovery and strain mechanisms [58]. The recovery mechanism is usually controlled by climb of edge dislocations although Poirier pointed out that cross-slip of screw dislocations could also control recovery and creep [59].

MgO is one of the ceramic material for which mechanical properties were the more intensively studied in the mid-20th century. In the Section 3, we see how multi-scale simulations and modeling were able to recently propose theoretically-based clarifications for most of the mechanical behavior highlighted in experiments.

3. Multi-Scale Modeling of MgO Deformation

The numerical and multi-scale investigation of plastic deformation in MgO reflects a renewed interest in the field of both materials (nano-mechanics, ceramics applications) and applications in the Earth's sciences. These studies all rely on the basic MgO dislocation core properties, down at the atomic scale, which started to be described several decades ago, in the 1970s. In this section, we first outline dislocation core modeling, from cluster-based embedded models up to the more recent Peierls–Nabarro–Galerkin (PNG) approach. Then, a short section will focus on dislocation mobility and kink-pair modeling in MgO. The sensitivity of dislocation velocity to stress and temperature are discussed. To conclude, a final section focuses on grain-scale plasticity modeling using dislocation dynamics simulations, a meso-scale tool for the modeling of the collective behavior of dislocations.

3.1. Dislocation Core Modeling: Methods and Results

Over the last fifty years, only few studies focused on the dislocation (core) properties at the atomic scale in MgO. One of the issues lies in the choice of an accurate interatomic potential to describe the core configuration. Rigorous determinations often require the use of first-principles calculations. However, this choice was not always numerically tractable for studies of dislocations due to the long-range stress and strain field associated to these defects. Empirical potentials are thus often used to circumvent this limitation. In ionic materials, classically, the pair potential involves coulombic interactions (at long range), non-coulombic short-range interactions plus eventually polarization effects. In case of MgO, short range interactions are usually described through a Buckingham term (a semi-empirical description based on a Born-Mayer and a Van Der Waals term) [60]. In addition, as MgO is known to exhibit a strong deviation from the Cauchy conditions, $C_{12} = C_{44}$, most accurate potentials go beyond the description of central forces, using for instance a core-shell or a breathing shell model to allow a rigorous treatment of polarization effects (e.g., [61]). A review of the different methodologies used to model dislocation cores [62] shows that the three most common approaches were applied to MgO: cluster-based embedded models, fully periodic dipole models and the semi-continuum Peierls–Nabarro model. In the following, we review the literature according to these methods.

3.1.1. Cluster-Based Embedded Models

The earliest atomistic models of dislocation cores in MgO were proposed by Woo and co-workers at the end of the 1970s [17,63–65]. Woo and colleagues performed simulations on isolated edge dislocations

WD EX1058
Western Digital v IP Bridge
Page 8

in the ½<110>{110} slip systems. In their simulations, a straight edge dislocation is placed at a center of a cylindrical central region where atoms are free to relax during energy minimization. To ensure that the simulation corresponds to a single dislocation in an infinite crystal, an outer cylindrical region is added to the boundary. In this boundary region, the atomic positions are well defined and kept fixed to the solution of the dislocation displacement field given by linear anisotropic elasticity. Despite the various drawbacks of the cluster approach with rigid boundary, Puls and Norgett [64] succeeded in stabilizing an edge dislocation into two sets of symmetrical configurations corresponding to a core position in the minimum of the Peierls potential (as shown Figure 5) and to a metastable core located on the top of the Peierls potential. They were thus able to predict a Peierls energy barrier for a ½<110>{110} edge dislocation between 0.01 and 0.04 eV/b (depending on the choice of the potential used to perform the simulation) which corresponds to a reasonable Peierls stress estimation of a few hundreds of MPa.

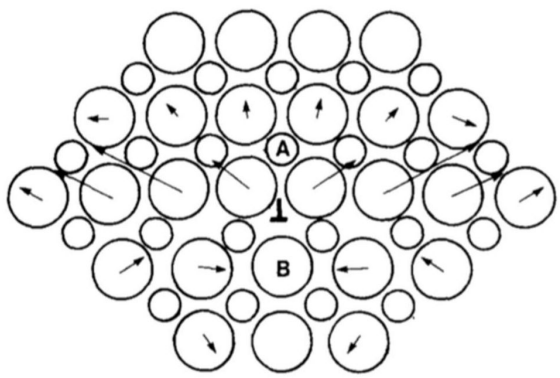

Figure 5. Atomic configuration of a 1/2<110> edge dislocation. Reproduced from [64] with the permission of AIP publishing.

Later, a similar cluster-based methodology was adopted by Watson [66] to simulate the atomic arrangement around different screw dislocations with <100> and ½<110> Burgers vectors. Motivated by the importance of dislocations in crystal growth, their study represents the first simulation of screw dislocations in ionic systems.

3.1.2. Periodic Dipole Model

In a periodic dipole model, a dipole of dislocations with opposite Burgers vectors is placed according to a periodically quadrupolar arrangement to minimize the residual strains in the simulation volume [67]. The fully periodic dipole model was used in MgO in the recent study of Carrez and colleagues [68] to take advantage of first-principles calculations. The ½<110> screw core structure is shown in Figure 6 using a so-called differential displacement map [69] to reveal the details of the atomic arrangement inside the screw core. As expected, due to the low critical shear stresses on ½<110>{110}, the screw core structure is found almost entirely spread in {110}. A close inspection of the atomic arrangement in the vicinity of the dislocation core shows that the spreading allows bringing oppositely charged ions on top of each other (see Figure 6). To further accommodate the O-Mg bonds, the screw core lying in a $(1\bar{1}0)$ glide plane is associated with a dilation state with an edge displacement component restricted to $(1\bar{1}0)$ (see Figure 7).

WD EX1058
Western Digital v IP Bridge
Page 9

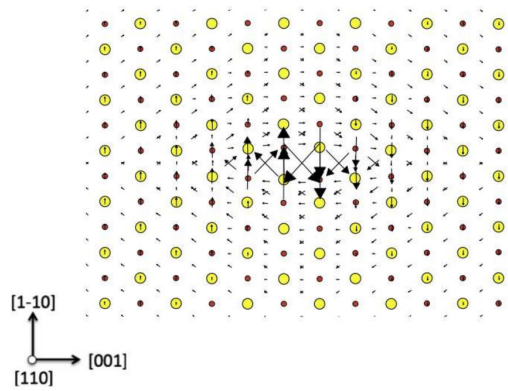

Figure 6. Differential displacement plot of ½<110> screw core at ambient pressure. As for a screw dislocation, most of the displacements are along the direction of the Burgers vector (i.e., along the [110] direction of the dislocation line), the dislocation core spreading can only be visualized by plotting arrows between pairs of neighboring atoms with lengths proportional to the magnitudes of their relative displacements along [110] as compared to ideal positions in the perfect crystal. Adapted from Ref. [68].

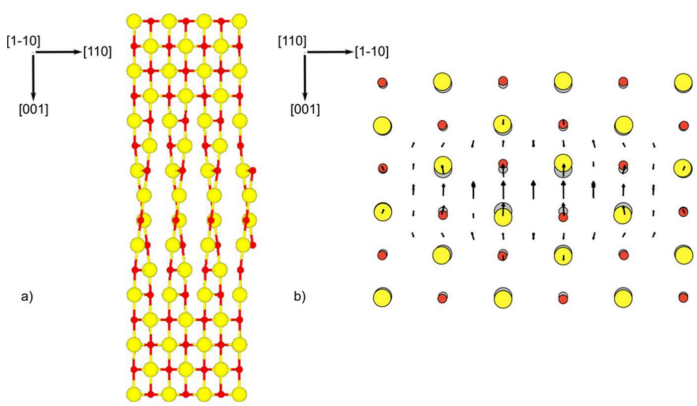

Figure 7. (**a**) Normal view to a screw dislocation line lying on a {110} glide plane. Only ions below and above the glide plane are shown; (**b**) Edge displacement field at the center of ½<110> screw dislocation core. Adapted from [68]).

3.1.3. Semi-Continuum Peierls–Nabarro Model

The Peierls–Nabarro (PN) model [70,71] is an efficient approach to describe dislocation cores incorporating the equivalent of an inelastic atomic energy instead of explicitly treating the atomic scale details of the core. In this model, a dislocation is viewed as a continuous distribution of infinitesimal dislocations ρ of elementary Burgers vectors db with $db = \rho(x)dx = (df/dx')xdx$, where f corresponds to the disregistry of the dislocation. In an elastically isotropic system, each infinitesimal dislocation creates a stress field which tends to extend the core. The equilibrium shape of the dislocation results then from the balance between non-elastic restoring force and the elastic ones described above. Whereas, in the original model, the restoring force used was an analytical sine function, Christian [69] demonstrated that it can be approximated to the gradient of the so-called generalized stacking fault (GSF) energy. Thus, atomistic effects are introduced in the PN model according to GSF calculations. The concept of the GSF energy (also called γ-surface) was initially introduced by Vitek [72] to systematically explore the stacking faults in bcc metals. The idea is to map out atomistic interaction energies across a shear plane as a function of any displacement. Corresponding to a rigid shear of two half crystals, one over the other, this type of calculation has a low CPU cost and is therefore feasible using first-principles simulations. It is worth noticing that repeating the

WD EX1058
Western Digital v IP Bridge
Page 10

same calculations with any empirical potential is also an interesting option to quantify the transferability of any empirical potential to the proper description of atomic displacements within dislocation cores.

GSF energies for {100} and {110} in MgO were computed using either first-principles calculations or several pairwise potentials [23,73,74]. In both planes, shear along ½<110> corresponds to the lowest energy path (Figure 8). According to first-principles calculations [23], the maximum unstable stacking fault energy along <110> ranges from 1.05 J/m^2 in {110} to 2.46 J/m^2 in {111}, with 2.18 J/m^2 in {100} in between.

In the PN model, the dislocation core width can be calculated from a balance between restoring forces derived from γ-surfaces and the elastic properties of the crystal. Thus, according to the respective γ-surface energies for {110} and {100}, the 1/2<110>{100} edge dislocation is characterized by a smaller core width than the one found for 1/2<110>{110} [23,74]. For the 1/2<110>{110} edge dislocation, solutions of the PN model lead to a wide spreading of the dislocation core [73,74] in agreement with the early atomic configuration suggested by Woo and collaborators [17,63–65]. This shows that, despite the various assumptions, the PN model leads to a good description of the dislocation core geometry in case of planar core configurations. To accurately model screw dislocation cores using the PN model, some of the intrinsic limitations like the need to focus *a priori* on a particular slip plane have to be overcome [75]. A modified version of the PN model, the Peierls–Nabarro–Galerkin (PNG) method [76], was applied in MgO to model the core structure of the screw dislocation with ½<110> Burgers vector [23]. In this model, core spreading in several planes can be considered simultaneously. Given this improvement, the screw core computed according to the PNG approach perfectly matches the atomistic configurations depicted above [68].

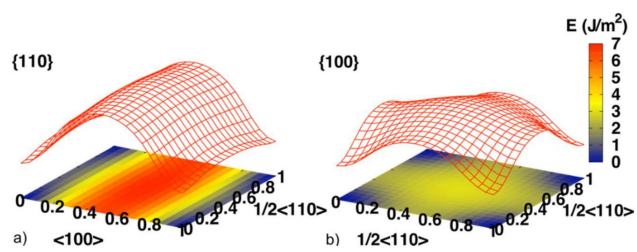

Figure 8. MgO γ-surface for (**a**) {110} and (**b**) {100} slip modes computed with first-principles. Adapted from [23].

One of the main achievements of the PN model is to provide reasonable estimates of dislocation core sizes (e.g., Ref. [77]). However, equally importantly, the PN approaches allow one to evaluate the Peierls stress. Classically in the PN model, the evaluation of the Peierls potential is performed by a discrete summation of the γ-energy corresponding to the disregistry function of the dislocation core solution of the PN equation (for instance [78]). The evaluation of the Peierls stress is however influenced by the numerical scheme used for the discrete summation. Consequently, the various stresses computed according to PN approaches in MgO agree with the order of magnitude but may show some discrepancies [15,18]. According to the most recent evaluation [23], the Peierls stresses for ½<110>{110} are 150 MPa for screw and 80 MPa for edge components. For ½<100>{100}, the Peierls stresses are 1600 MPa and 300 MPa for screw and edge components respectively. For the two slip systems, the estimation of Peierls stresses are consistent with the experimental determination discussed above and shown in Figure 2. Finally, as reviewed in Section 5, the introduction of γ-surfaces calculated from first-principles at high pressures enable investigations of the effect of pressure on the dislocation properties in MgO.

3.2. Dislocation Mobility in MgO

MgO is a material with reasonably high lattice friction, like for example in bcc metals (e.g., iron and tungsten). Therefore, below the athermal temperature T_a, dislocation glide is controlled by thermally-activated jumps of dislocation portions called kink-pairs, while phonon drag constrains dislocation velocity at higher temperatures.

WD EX1058
Western Digital v IP Bridge
Page 11

3.2.1. The Kink-Pair Mechanism

In the thermally-activated regime, the dislocation motion over the Peierls potential is assisted by the conjugate effect of stress and thermal activation (see, e.g., [79,80] for an extended description). During this process, the dislocation does not move as a straight line but through the nucleation of kink-pairs. The further propagation of the kinks along the dislocation line is responsible for the glide of the whole dislocation. The theoretical description of dislocation motion involving the kink-pair mechanism was successfully applied to the understanding of elemental deformation processes (see, for instance, [81]) in several materials, including bcc metals [82–89], covalent materials such as silicon [90–92] and ionic materials [93–95], including MgO [23].

The kink-pair nucleation process is usually associated with a critical change in enthalpy that has to be supplied by thermal activation under a given stress. The change in enthalpy ΔH_k, consisting of three contributions, follows the general equation:

$$\Delta H_k = \Delta_{elast} + \Delta W_p - W_\tau \quad (2)$$

The two positive contributions, ΔE_{elast} and ΔW_p correspond respectively to the increase of the elastic energy of the kinked dislocation line and to the increase of the Peierls energy due to the part of the line lying on the Peierls barrier. These quantities are balanced by the work of the applied stress τ. Several theoretical models, only differing by the treatment of the change in elastic energy, were proposed to evaluate the critical kink pair nucleation energy Δ_k^{crit}. Among these are the line tension (LT) model [29,96], the kink-kink interaction model [97] and the elastic interaction (EI) model [98,99]. Atomistic simulations can also be used to compute the critical nucleation enthalpy (e.g., [91]) or to evaluate the different energy components involved in the LT model (e.g., [89]). Nevertheless, such approaches have not been applied to MgO up to now. Instead, in Ref. [23], the EI model was used to numerically estimate the evolution of Δ_k^{crit} as a function of the applied stress.

The evolution of Δ_k^{crit} for screw components belonging to 1/2<110>{110} and 1/2<110>{100} is shown in Figure 9. The nucleation of a double-kink on a 1/2<110>{110} dislocation requires a lower energy when compared to 1/2<110>{100} which is consistent with the analysis of Takeuchi [4] based on experimental mechanical data. For slip on {110}, the isolated kink energy U_k (corresponding here to $0.5 \times \Delta_k^{crit}(\tau = 0)$) is 0.55 eV, in a rather good quantitative agreement with the activation energies of 0.2–1.0 eV, derived by the measurement of the Bordoni peaks and accounting for the possible scatter induced by impurities [100].

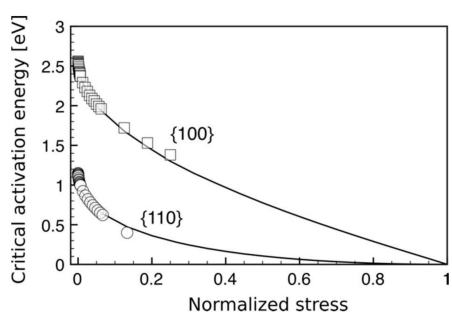

Figure 9. Kink-pair activation energy (EI model) for screw dislocation in MgO as function of stress (normalized by the Peierls stress). Adapted from [23].

More generally, the activation enthalpy for the kink-pair mechanism involves both nucleation and migration of kinks. However, only one of the two processes generally act as a limiting factor. In the case of MgO, according to the EI model, the kink Pairs widths are found to be larger than 50*b*. Such a large width is not compatible with sharp rectangular kink pairs but more probably accounts for both the kink pair width configuration plus the spreading of the two individual kinks [23]. It was then concluded that the individual

WD EX1058
Western Digital v IP Bridge
Page 12

kinks should be widely spread, bearing a low migration enthalpy barrier. Based on the Frenkel–Kontorova model (e.g., Ref. [101]), for an individual kink width larger than a few b, one can show that the migration energy would be at least of one order of magnitude lower than U_k. The kink-pair mechanism in MgO is then assumed to be controlled exclusively by the nucleation of the kink-pair. Nevertheless, there is still scope to improvement. With the rapid increase of atomistic simulation capabilities, the shape and energy of kinks could be determined by atomistic simulations following the recent scheme proposed in bcc metals or covalent materials (see [92,102–104] for instance).

3.2.2. Dislocation Glide Velocity

Based on the Guyot and Dorn formalism [29], the jump frequency of a dislocation in the thermally-activated regime ($T < T_a$) is defined by Equation (3).

$$\nu(\tau, T) = \frac{\nu_D b}{w^*(\tau)} \frac{L}{2w^*(\tau)} exp^{-\Delta H^*(\tau)/kT} \tag{3}$$

where $\nu_D b/w^*(\tau)$ is the oscillation frequency of a dislocation segment of length $w^*(\tau)$ and ν_D is the Debye frequency. $L/2w^*(\tau)$ refers to the number of nucleation sites for kink-pairs and the exponential term accounts for the kink-pair nucleation probability which can be either deduced from experimental data following an inverse engineering process or computed using atomistic simulation as described in the Section 3.2.1. Please note that this formalism is only valid when kink-pair nucleation is the limiting process when compared to kinks propagation along the line.

Equation (3) only refers to forward kink-pair jumps. However, at low stress (e.g., close to T_a), the kink-pair nucleation process can proceed either along the forward displacement direction or along the opposite one. In addition, it is obvious that Equation (3) does not go to zero at the zero-stress state. To solve both inconsistencies, Nabarro [105] proposed to integrate kink-pair backward jumps using a double-exponential equation leading to a new frequency definition:

$$\nu(\tau, T) = \frac{\nu_D b}{w^*(\tau)} \frac{L}{2w^*(\tau)} \left(exp^{-\Delta H^+(\tau)/kT} - exp^{-\Delta H^-(\tau)/kT} \right) \tag{4}$$

where $\Delta H^+(\tau)$ and $\Delta H^-(\tau)$ refer to forward and backward kink-pair activation energy, respectively.

Finally, based on Nabarro's work [105], the dislocation mobility in the thermally-activated regime is defined by reintroducing the Peierls potential periodicity a' (Equation (5)). This formulation applies specifically for each dislocation character and its validity for screw dislocations in MgO was confirmed by experimental measurements in the case of ½<110>{110} dislocations [16,23].

$$\nu(\tau, T) = a\prime \frac{\nu_D b}{w^*(\tau)} \frac{L}{w^*(\tau)} exp^{-\Delta H_0/kT} \sinh\left(\frac{\Delta H_0 - \Delta H^*(\tau)}{kT} \right) \tag{5}$$

On the other hand, beyond the athermal transition ($T > T_a$), lattice friction vanishes and the resulting dislocation structure is characterized by more isotropically shaped defects, as shown by TEM micrographs (see, e.g., Figure 3b). In this "fcc-like" regime, the velocity of dislocations is constrained by a viscous drag that is attributed to the interactions between dislocations, phonons and electrons (Equation (6)).

$$\nu(\tau, T) = \frac{b\tau}{B(T)} \tag{6}$$

where *B(T)* is a viscous drag coefficient generally in the range of 10^{-5} Pa·s in ionic crystals.

3.3. Grain-Scale Plasticity Modeling Using Dislocation Dynamics: On the Collective Behavior of Dislocations

3.3.1. Methods: 3D and 2.5D Dislocation Dynamics

Dislocation dynamics (DD) simulations are at the interface between atomic scale and continuum approaches. They provide the link between physics-based plasticity laws (continuum elasticity theory) and macroscopic deformation.

WD EX1058
Western Digital v IP Bridge
Page 13

In 3D simulations, the elementary unit is a dislocation segment or a node that bridges two dislocation portions, depending on the chosen approach [106,107]. Therefore, while atomistic simulations commonly refer to the nm-scale, DD simulations allow modeling volumes up to a few hundreds of μm^3 including large populations of dislocations. Many DD applications exist for the cases of nano-indentation [108], precipitation hardening [109–111], fatigue [112] or micropillar compression [113–115], all applied whatever the crystalline materials. Mainly, all DD codes follow similar calculation steps. After the definition of a starting configuration (including sample design, dislocation density distribution and mechanical setup), a stress or strain is applied. Then, forces between dislocations are computed (following iso- or anisotropic elasticity) and an effective stress is defined on each dislocation portion as the sum of each contributions, e.g., applied stress, line tension, lattice friction and neighboring stress fields. Finally, dislocations displacements are solved iteratively using a dislocation mobility law (see e.g., Equation (5) or Equation (6)) integrated using a simple time step that scales from 10^{-10} s up to approximately 10^{-6} s depending on the problem under study. As inputs, DD simulations generally refer to crystallography, temperature, elastic constants as well as dislocation core properties. The testing conditions are also obviously required. In the evolution of the dislocation microstructure under stress, data such as stress–strain curves, dislocation density evolution, plastic shear per slip mode as well as local stress maps are then easily obtained.

On the other hand, 2.5D simulations were developed in the early 90s [116–118] but are still used to investigate particular questions, such as dislocation organization, mobility or diffusion-assisted plasticity. In 2.5D DD simulations, dislocations are introduced as straight segments of constant length, all perpendicular to a reference plane giving rise to a quasi-2D projection. When compared to 3D simulations, local rules are introduced to describe dislocation multiplication, short-range interactions and junction formation to reproduce at best the 3D dislocation evolution but using a simplified and "cheaper" (in terms of CPU costs) framework. More details about 2.5D simulations can be found, e.g., in the recent study of Curtin and collaborators [119].

3.3.2. Dislocation Interactions Mapping

Dislocation contact reactions are one of the key processes to understand strain hardening. They can be computed using 3D-DD simulations based on Kroupa's force equation (see, e.g., Ref. [79]) that characterizes the attractive/repulsive character of the interaction $\vec{F_{12}}$ between two dislocations and the line tension equilibration equation calculated at the triple nodes which defines the (φ_1, φ_2) ensemble favorable to the junction formation (Equations (7) and (8)).

$$\vec{F_{12}} = \frac{\mu}{\left|\vec{l_1} \times \vec{l_2}\right|} \frac{\vec{R_{12}}}{R_{12}} \left\{ \frac{1}{2} \left(\vec{b_1} \cdot \vec{l_1}\right) \left(\vec{b_2} \cdot \vec{l_2}\right) - \left(\vec{b_1} \times \vec{b_2}\right) \cdot \left(\vec{l_1} \times \vec{l_2}\right) + \frac{1}{1-\nu} \left[\left(\vec{b_1} \times \vec{l_1}\right) \cdot \frac{\vec{R_{12}}}{R_{12}} \right] \left[\left(\vec{b_2} \times \vec{l_2}\right) \cdot \frac{\vec{R_{12}}}{R_{12}} \right] \right\} \quad (7)$$

where $\vec{l_1}$ and $\vec{l_2}$ refer to unit line vectors of dislocations 1 and 2, respectively; $\vec{b_1}$ and $\vec{b_2}$ are Burgers vectors; $\frac{\vec{R_{12}}}{R_{12}}$ is a unity vector along the force direction (i.e., along the shorter distance between the two dislocations); and ν is the Poisson ratio.

$$f(\beta_j) b_j^2 = f(\beta_1) b_1^2 cos(\varphi_1^*) - f'^{(\beta_1) b_1^2} sin(\varphi_1^*) + f(\beta_2) b_2^2 cos(\varphi_2^*) - f\prime(\beta_2) b_2^2 sin(\varphi_2^*) \quad (8)$$

where $f(\beta_j) = 1 - \nu cos^2(\beta)$ and β is the dislocation angle character.

These two equations lead to the definition of three configurations, i.e., the repulsive state, the crossed attractive state and the junction state. In addition, attractive dislocations with the same Burgers vector can lead to collinear annihilations. These simulations are driven by elastic energy minimization and no applied stress is imposed. More technical details on dislocation reactions can be found in [79]. The results of dislocation interaction mapping are independent of parent dislocations lengths and the junction region (made of φ_1 and φ_2 favorable configurations) is increased for energetically favorable configurations (Franck criterion). Finally, the junction strength τ_j scales with $\mu b / l_j$ (with l_j the junction arm length) depending on (φ_1, φ_2). Interactions maps were computed

WD EX1058
Western Digital v IP Bridge
Page 14

for a wide range of materials as, e.g., in fcc and bcc metals [120–122], hcp structures [123,124], ice [125] and minerals like olivine [126].

Figure 10, based on MgO slip system analysis, ½<110>{110} and ½<110>{100} dislocations lead to eight distinct types of interactions (see [45] for more details):

- Three maps for the {110} mode (self-interaction + {110} junction + {110} crossed/repulsive states): These reactions were investigated in Ref. [127] and show the possible formation of edge ½<110> junctions between dislocations in 60°/120° oriented slip systems. Junctions are oriented along <111> and belong to {112} slip planes. These dislocations could possibly justify {112} dislocation slip observed during nano-indentation tests (see Section 4). Ninety-degree oriented slip systems only lead to crossed or repulsive states.
- Two maps (plus self-interactions) for the {100} mode ({100} junctions + coplanar interactions): Coplanar interaction can lead to the formation of dislocation dipoles and only 90° oriented {100} slip systems can make ½<110>{110} edge junctions oriented along the <100> directions.
- Three *crossed* maps that involve one slip system from each {110} and {100} mode (collinear interactions + *crossed* junctions + crossed/repulsive states): Collinear annihilations can occur if dislocations with identical Burgers vectors interact what is the case for six combinations of slip systems. Collinear annihilation is the reaction promoting the strongest of all possible forest strengthening mechanisms [128,129]. Mixed junctions with ½<110> Burgers vectors can be made out of 60°/120° oriented slip systems.

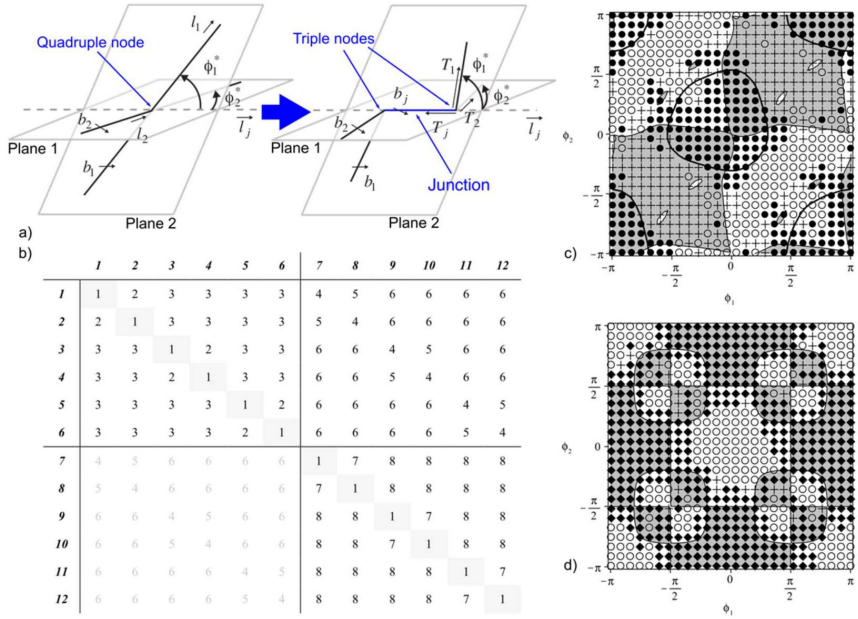

	1	2	3	4	5	6	7	8	9	10	11	12
1	1	2	3	3	3	3	4	5	6	6	6	6
2	2	1	3	3	3	3	5	4	6	6	6	6
3	3	3	1	2	3	3	6	6	4	5	6	6
4	3	3	2	1	3	3	6	6	5	4	6	6
5	3	3	3	3	1	2	6	6	6	6	4	5
6	3	3	3	3	2	1	6	6	6	6	5	4
7	4	5	6	6	6	6	1	7	8	8	8	8
8	5	4	6	6	6	6	7	1	8	8	8	8
9	6	6	4	5	6	6	8	8	1	7	8	8
10	6	6	5	4	6	6	8	8	7	1	8	8
11	6	6	6	6	4	5	8	8	8	8	1	7
12	6	6	6	6	5	4	8	8	8	8	7	1

Figure 10. Interaction between dislocations in MgO modeled using DD simulations: (**a**) dislocation reaction scheme leading to a junction; and (**b**) interaction matrix between ½<110>{110} and ½<110>{100}. Indices refer to slip systems as described Table 1. Numbers inside the matrix refer to each type of reaction i.e., 1 is self-interaction; 2 and 3 are, respectively, {110} junctions and {110} crossed/repulsive states; 7 and 8 are, respectively, {100} coplanar interactions and junctions; 4 refers to collinear interactions; and 5 and 6 refer to {110} + {100} junctions and crossed/repulsive states that involve both slip modes. (**c**,**d**) Example of dislocation reaction maps ({110} junction and collinear interactions). Black lines refer to the elastic solution for dislocations interaction based on Equations (7) and (8). White and grey regions describe repulsive and attractive areas. Symbols are DD simulation results where crosses are attractive crossed-states, circles refer to repulsive states, filled circles are junctions and filled diamond are annihilations.

WD EX1058
Western Digital v IP Bridge
Page 15

3.3.3. Grain-Scale Deformation: On the Role of Temperature on MgO Single Crystal Flow

Only few DD studies were performed to investigate oxides' deformation. In addition to the work of Cordier's group for mineral physics applications [23,45,126,127,130–132], one can refer to the work of Chang and coworkers who investigated the plastic deformation of <111>-oriented LiF micropillars from room temperature up to 600 K [113]. In this study, DD simulations predict a size-dependent flow stress in the micrometer-size regime ("*smaller is stronger*") in good agreement with experimental results [133], see also Section 4.5.

In MgO, Amodeo and collaborators investigated the deformation of bulk MgO single crystal using DD simulations [23,45]. In Ref. [23], the authors used the multi-scale approach described in Sections 3.1–3.3 to build a model able to mimic single crystalline compression tests for a large range of temperatures. 3D-periodic micrometer-sized sample were modeled including two dislocation distributions. In the thermally activated-regime, as the CRSS is believed to be intrinsically controlled by the velocity of long screw dislocations (Equation (5)), the simulation cells include only a single infinite (i.e., periodic) screw dislocation, the cell volume being tailored according to a reasonable initial dislocation density of 10^{12} m^{-2}. Only single slip configurations were tested under compression at $\dot{\varepsilon} = 10^{-4}$ s^{-1} for $T < T_a$. Within the athermal regime ($T > T_a$), simulations are performed in larger simulation cells including an initial dislocation microstructure made of several dislocation sources ($\rho = 10^{12}$ m^{-2}) equally distributed between each slip system. Two sets of orientations were tested to activate glide on the {110} and {100} planes independently.

As shown Figure 11, the conclusions of the study show that this atomistically-informed DD approach can be used to describe bulk incipient plasticity in MgO single crystal, especially when compared to pure (or heat-treated) samples. Modeled CRSS vs. temperature curves are in good agreement with experimental data for the two slip modes, including the both thermal and athermal deformation regimes. While this study appears as one of the first *full-numerical* model of single crystal plasticity (no experimental parameterization), one can miss: (i) the lack of solute hardening processes in the model which are known to strongly influence MgO plasticity at intermediate temperatures; and (ii) the distinction made between {110} and {100} modes in bulk simulations (no multi-mode configuration tested).

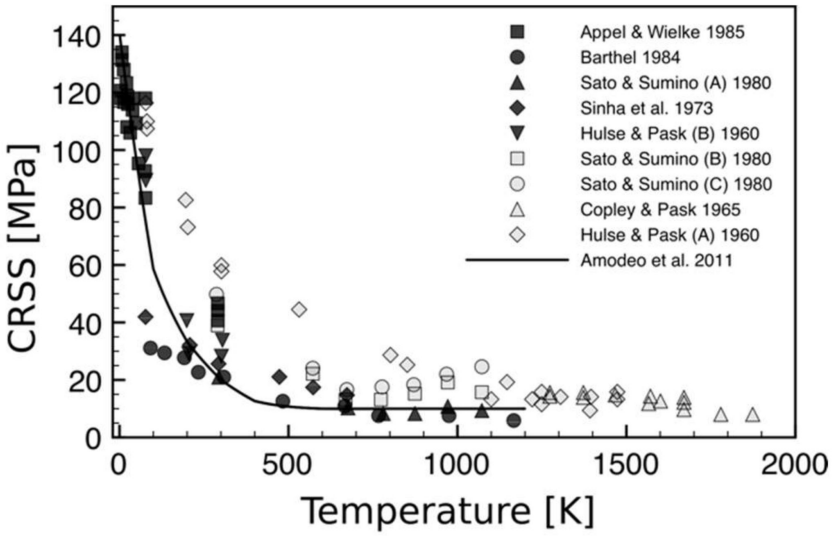

Figure 11. CRSS for 1/2<110>{110} slip systems. Comparison of the multi-scale model of Amodeo et al., 2011 (black line) [23] and experiments (symbols). The model is in better agreement with data found in pure or heat-treated MgO (black symbols). Adapted from Ref. [23].

Finally, strain-hardening of MgO single crystals at high-temperature was investigated using a similar DD simulation setup [45]. As in the case of fcc metals, MgO forest hardening is ruled by a Taylor type

equation (Equation (9)) with moderated hardening coefficients α of about 0.24 and 0.28 respectively for {110} and {100} slip modes. Such values are attributed to harder reactions as the 60°/120° {110} junction and the {100} junction (see Figure 10).

$$\tau_f = \alpha \mu b \sqrt{\rho} \tag{9}$$

Strain-hardening rates were also computed and show a satisfactory agreement with experiments [8,14,44] at 1000 K and 2000 K for both slip modes. Again, no multi-mode configurations between slip modes were investigated.

3.3.4. Creep Modeling

Weertman creep based on dislocation glide and climb was recently modeled using DD. Due to the additional computational cost associated with modeling diffusion, the models used are usually based on 2.5D simulations [131,134]. An illustration is presented in Figure 12. Reali and collaborators [132] used this approach to model creep in MgO. The chosen reference plane was (111) that contains the glide and climb directions of the two investigated slip systems (with Burgers vectors $\frac{1}{2}\left[01\overline{1}\right]$ and $\frac{1}{2}\left[\overline{1}01\right]$, gliding in (011) and (101) respectively) [132].

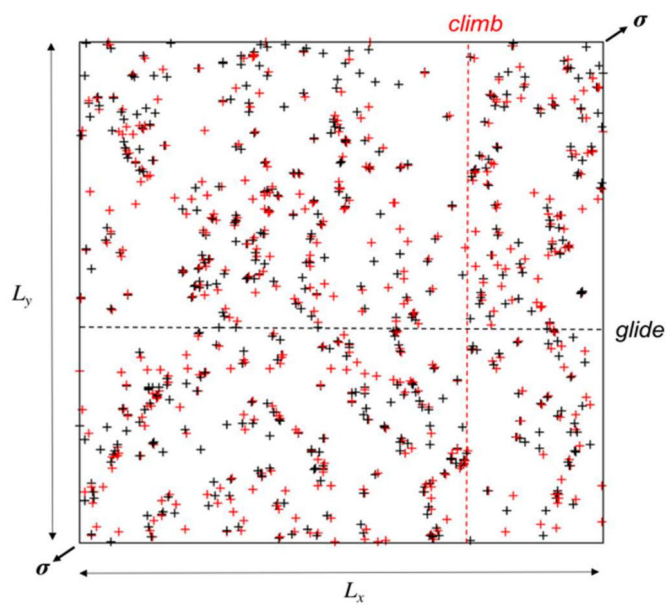

Figure 12. 2.5D-DD simulations. Black and red crosses refer to dislocations with opposite Burgers vectors.

The mobility of dislocations is determined by ascribing them relevant velocity laws. In MgO 2.5-DD simulations, Equation (6) (viscous drag equation) is used to describe the glide mobility of dislocations in the athermal regime while the climb velocity is described by the following equation:

$$v_{climb} = \eta \frac{D}{b}\left[\exp\left(\frac{\tau_c \Omega}{k_B T}\right) - \frac{c_\infty}{c_0}\right] \tag{10}$$

where η is a factor which depends on the geometry of the flux field; D is the diffusion coefficient of the species which controls the process; Ω is the activation volume for self-diffusion; τ_c is the effective stress resolved in the climb direction; c_∞ is the vacancy concentration far from the dislocation lines; and c_0 is the intrinsic vacancy concentration at the temperature T considered. For more technical details, the reader is invited to refer to Boioli and Reali's studies [131,132].

WD EX1058
Western Digital v IP Bridge
Page 17

A major difficulty of these simulations is to handle two very different kinetics: the one of glide and the one of climb. Both are associated with a characteristic time step. First, stress is applied and only glide is allowed, all glide events being resolved using the time step for glide (which is the smallest). The corresponding plastic strain is calculated. However, with glide only, the microstructure rapidly reaches a quasi-equilibrium situation and plastic strain cannot proceed any further. Then, the mobility is set to climb using the longer climb time step until at least one dislocation has climbed over a distance b. The simulation is then switched back to glide and the process is repeated. Activation of climb allows recovery processes such as annihilation, which in turn allow some dislocations to be freed and glide again until a new jammed configuration is reached. The repetition of these processes leads to a steady-state process, as shown by a constant rate of plastic strain evolution and a constant dislocation density. As usually assumed in Weertman creep, these results demonstrate that the contribution of climb to the total plastic strain is negligible, although this process controls the creep rate.

The creep rate being controlled by climb, it depends critically on the diffusion of the slowest species. In MgO, it is usually assumed that oxygen diffusion is the slowest. The simulations presented here were performed with the oxygen self-diffusion coefficients of Yoo and collaborators (i.e., 5.2×10^{-20} m^2/s at 1700 K) [135]. The creep results are presented in Figure 13 where the plastic strain rate is plotted versus strain and reciprocal temperature. These results show that the 2.5D-DD model predicts a creep behavior which follows a power law of the type:

$$\dot{\varepsilon} = \dot{\varepsilon}_0 \sigma^n \exp\left(-\frac{E}{k_B T}\right) \tag{11}$$

with $n = 2.9$, and $E = 300$ kJ/mol which is in excellent agreement with experimental results.

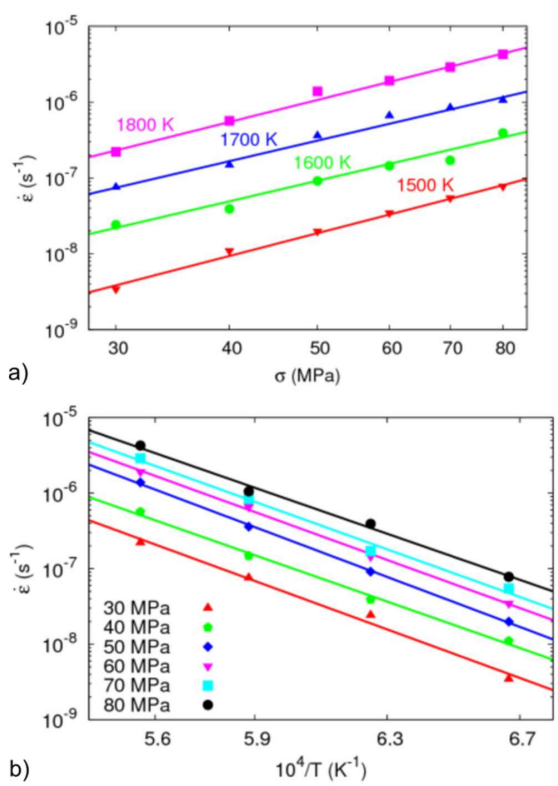

Figure 13. Results of 2.5D-DD simulation of creep in MgO: (**a**) creep strain-rates as a function of stress; and (**b**) creep strain-rates as a function of reciprocal temperature. Adapted from [132].

WD EX1058
Western Digital v IP Bridge
Page 18

MgO is one of the top most advanced ceramics in terms of multi-scale modeling of mechanical properties and dislocation-based processes. Specific attributes that are crucial to explain plastic deformation such as dislocation core, mobility and interactions were investigated using the more modern modeling approaches (atomistic simulations, dislocation dynamics, and FEM), for a wide set of PT conditions. While simulation and modeling approaches highlighted prior experimental observations, it allows today opening new routes describing the mechanical behavior of MgO under extreme conditions, at the limit of experimental capabilities. In the Section 4, we see how miniaturizing mechanical tests recently brought additional perspectives on the elementary deformation processes of MgO.

4. Nano-Mechanical Testing of MgO

Nano-indentation testing is widely used for the determination of local mechanical properties such as hardness and elastic modulus [136–139]. Thanks to the accurate control of the force and displacement of the indenter tip, this technique is also used to induce local plastic deformation and obtain load–displacement curves. For nanometer sized indents, the plastic deformation mechanisms can be analyzed in terms of individual dislocations. Nano-indentation tests also allow to study dislocation nucleation, since the volume involved during a nano-indentation tests is often small enough to be free of pre-existing defects and thus of potential dislocation sources. MgO can be considered as a model material for this kind of approach because of its reduced number of slip systems, and because single crystals can be easily cleaved along a (001) plane (as mentioned in Section 1), providing well oriented and very flat surfaces suitable for nano-indentation tests. There is also an extensive literature on plastic dislocation structures generated during conventional micro-indentation tests in MgO.

In the following, a short review on micro-indentation in MgO is first presented to describe the general dislocation organization around an indent. A second part describes the elementary dislocation mechanisms in MgO around a nano-indentation imprint through slip line or etch pits analysis at the nanometer scale. In the third part, dislocation nucleation is considered thanks to spherical nano-indentation. The fourth part describes how the analysis and modeling of simple dislocation pile ups nucleated during a spherical nano-indentation can be used to determine mechanical properties of the material such as the lattice friction stress. Finally, the last part is dedicated to micro-compression tests performed with a nano-indenter equipped with a flat punch on micropillars and nanocubes.

4.1. Micro-Indentation in MgO

Since MgO and relatives such as LiF or KCl are brittle at room temperature, micro-indentation test was used early in the 1950s to introduce local plasticity [140,141]. The first analyses of the dislocation structure around the indent were carried out by Keh [142] and Newey [143]. They used chemical etching to produce etch pits on the surface at the emergence points of the dislocations. These micrometer size etch pits were then observed by optical microscopy (Figure 14). These initial studies were then followed by TEM studies [144] to identify the Burgers vector of the dislocation, as well as their organization in the volume around the indent. The dislocations are organized along a height rosette arms pattern as shown in Figure 14. The four arms oriented along the <110> directions correspond to dislocation half loops lying in $\{110\}_{90}$ planes perpendicular to the surface. Since these dislocations emerge with a pure edge character and a Burgers vector parallel to the surface, their propagation does not produce any visible surface deformation around the indent. The four other arms oriented along the <100> directions correspond to dislocation half loops lying in $\{110\}_{45}$ planes inclined at 45° from the surface. For these ones, the dislocations emerge with a screw character, so that their propagation gives rise to slip lines at the surface associated to a downward material displacement. The surface deformation associated with these slip lines was analyzed using SEM by Armstrong and Wu [145] and by Chaudhri [146]. At the intersection of different rosette arms, dislocations reaction, according to Equation (1), are reported by Keh [142,147]. These reactions lead to the formation of a Lomer lock supposed to be sessile for the aforementioned reasons. This obstacle to further dislocation propagation was associated with crack opening in $\{110\}_{45}$ planes by Keh [147] and Hammond and Armstrong [148].

WD EX1058
Western Digital v IP Bridge
Page 19

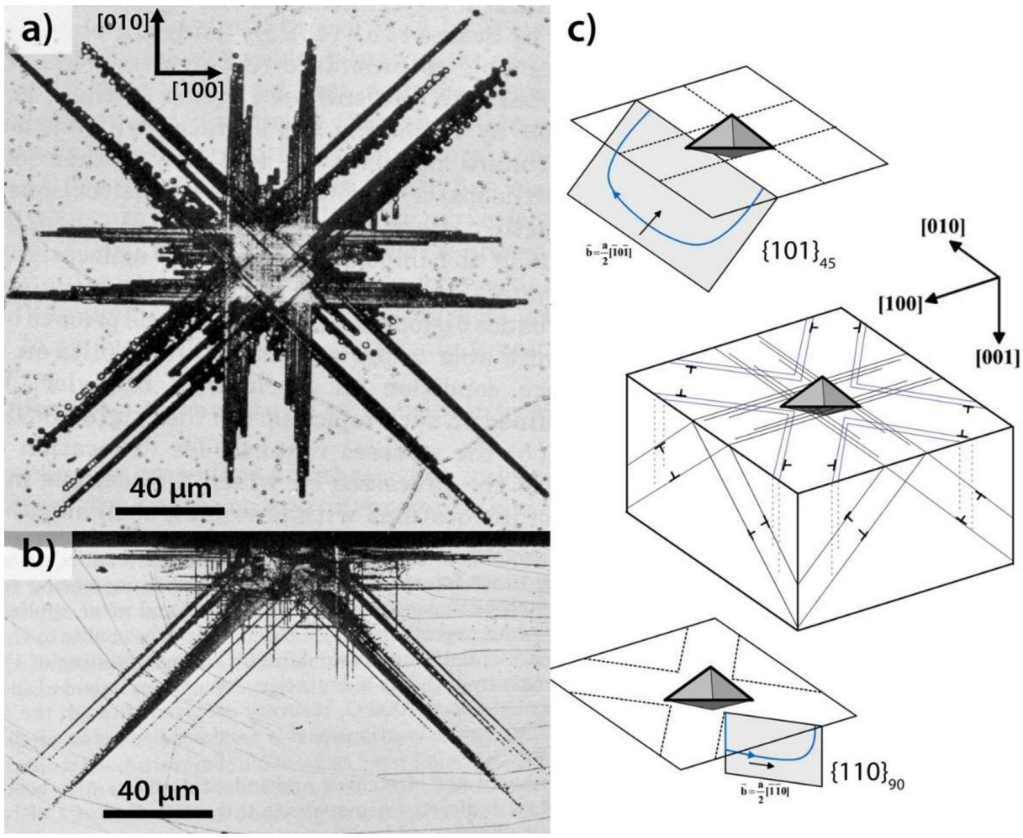

Figure 14. Dislocation structure around a Vickers micro-indentation in a (001) MgO surface. (**a**) Optical microscopy image of the etch pits pattern. The dislocations are organized in a rosette arms pattern (from Keh [142]). (**b**) Etch pits pattern in cross section in a (010) plane (from Keh [142]). (**c**) Schematic representation of the rosette arms dislocation structure (from Gaillard [149]). Images (**a**,**b**) are reprinted with permission from AIP Publishing.

4.2. Nano-Indentation: Analysis of Elementary Deformation Mechanisms

The analysis of dislocation structures around an indent has gained a renewed interest since the development of the nano-indentation technique in the 1990s. The increased sensitivity of load and displacement control of the indenter tip allowed inducing very small amount of dislocations in the material. Tromas et al. [150] used Atomic Force Microscopy (AFM) to observe the rosette arms around a nano-indentation imprint. The accuracy of the AFM allowed to observe individual slip lines in the <100> direction. Furthermore, its ability to measure heights at the sub-nanometer scale was used to determine the exact number of dislocations involved in the slip lines, since for a single dislocation the slip line height corresponds to the projection of the Burgers vector along the normal to the surface. Similar slip line analyses around indents were performed in other materials with the rock-salt crystal structure. In particular, Bennewitz and collaborators [151,152] produced and characterized atomic-scale plastic deformation by means of atomic force microscopy in ultra-high vacuum (UHV) on (001) surfaces of Potassium Bromide (KBr) single crystals.

Figure 15 presents a comparison between the slip lines at the surface around a Berkovich indent (triangular shape pyramid) observed by AFM and the dislocation structure in the volume observed by TEM [153].

These two observations are complementary since the slip lines only show the track left at the surface by the emergence and the propagation of the dislocations. Interestingly, this feature provides an access to the history of the dislocations, because the slip lines reveal the path that was followed by the dislocations.

WD EX1058
Western Digital v IP Bridge
Page 20

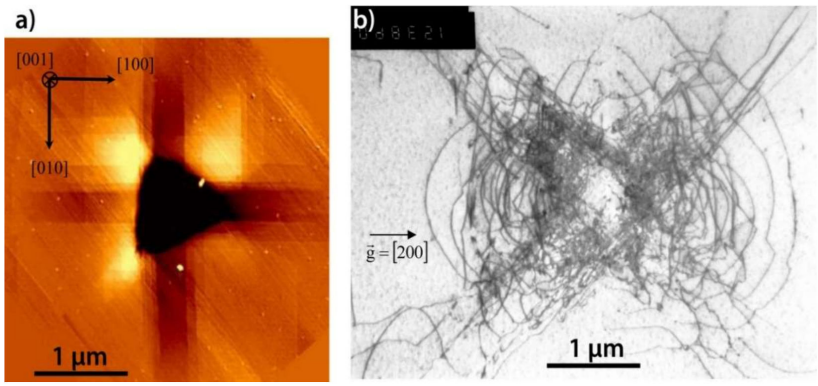

Figure 15. (**a**) AFM image; and (**b**) TEM image of two 3 mN Berkovich nano-indentation imprints in a (001) MgO surface. The scale and the orientations are the same for both images. The AFM image reveals the slip lines due to the emergence and propagation of dislocations while TEM reveals the dislocation structure in the volume.

Following this property, Tromas and collaborators observed an isolated slip line with a three-stages behavior around a Berkovich indent [13]. This line, which originates from a <100> rosette arm, is first deflected at 26° along a <120> direction over a short extent, before deviating again to propagate along a <010> direction perpendicular to its initial rosette arm (Figure 16). This threefold path was explained by the following mechanism. A screw dislocation gliding in a $\{101\}_{45}$ plane along the <100> direction reacts with a second dislocation gliding in a $\{110\}_{90}$ slip plane along a <110> directions. These two dislocations form a junction along a <111> direction according to Equation (1). Due to the high stress induced by the indenter, this segment glides in a {211} plane, leaving a slip line along a <120> direction at the surface, before cross-slipping into its natural $(011)_{45}$ slip plane. The dislocation can then easily glide in this new slip plane, leaving at the surface a slip line along a <010> direction perpendicular to the initial rosette arm (see Figure 16). Thus, this observation shows that the junction resulting from Equation (1) is not truly sessile and that the <110>{211} slip systems can be activated at room temperature in MgO. Furthermore, after the cross slip, while the dislocation segment reached its easy slip plane, its extremity is still pinned at a triple node formed by the two parent dislocations. Tromas and colleagues showed that this configuration leads to the activation of a spiral source ensuring the plastic deformation required for the indenter penetration [13].

Slip line analysis can thus provide detailed information about complex dislocation mechanisms that would be difficult to reveal by TEM. The drawback of this approach is that only four of the eight rosette arms can be observed, since the dislocations in the <110> directions do not produce any slip line. Furthermore, the slip lines do not provide direct information of the 3D organization of the underlying dislocation structure. Gaillard and collaborators [154] adapted the etch pits method of Gilman and colleagues [155] and Shaw and collaborators [156] at the nanometer-scale. By an accurate control of the etchant concentration and of the etching time, they produced nanometer-scale etch pits at the emergence points of the dislocations and observed them by AFM. This technique was repeated sequentially in a same area after successive chemo-mechanical polishing (CMP) stages. This so called nano-etching technique consists thus in a kind of dislocation tomography, allowing to reconstruct, layer by layer, the 3D dislocation structure. Figure 17 shows the etching patterns obtained at the surface and after successive CMP stages around a 80 mN Berkovich indent. The eight rosette arms are observed and each individual dislocation can be resolved. The dislocation reactions at the intersection of the rosette arms are also identified by following two etch pits along the successive CMP stages. These two etch pits progressively combine to form a single one, which is then always localized along the same <111> direction. The presence of Lomer junctions is also characterized by high etch pits concentration in the adjacent rosette arms, due to dislocation pile ups induced by these junctions.

WD EX1058
Western Digital v IP Bridge
Page 21

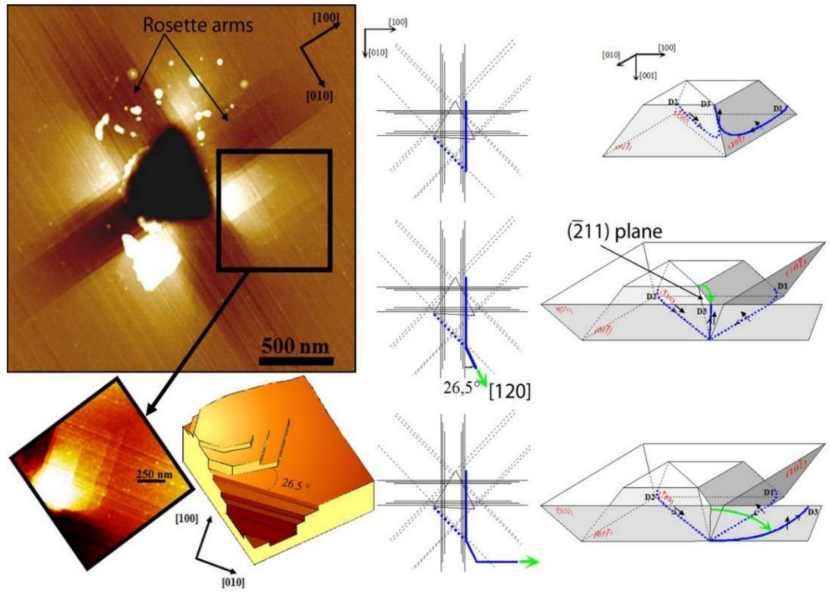

Figure 16. On the left side: AFM image of a 2.6 mN load Berkovich indent in a (001) MgO surface. A three-stages slip line is observed (enlarged view and schematic at the bottom). This trace shows the complex path followed by a dislocation segment gliding in a (211) plane and then cross slipping in a (011) plane (right side).

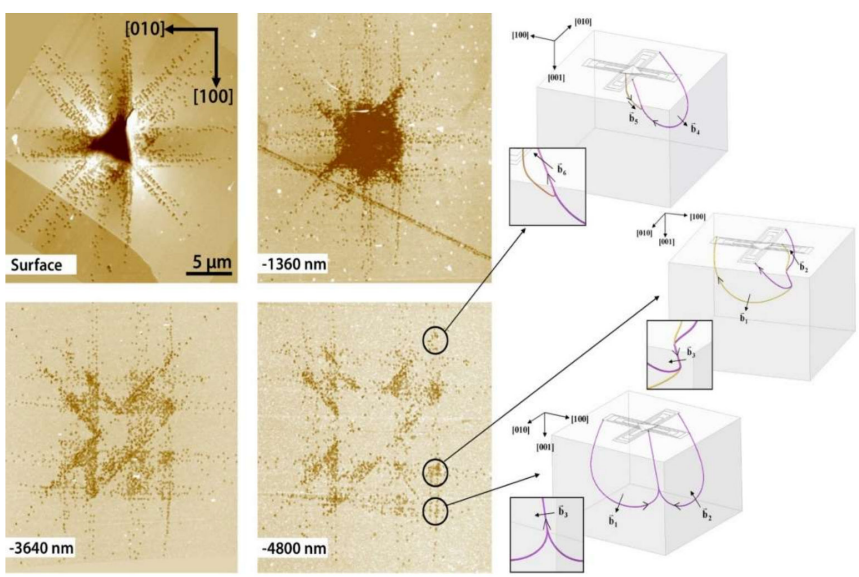

Figure 17. Left side: Successive AFM observations of the nano-etching pattern produced around an 80 mN nano-indentation in MgO at the surface and after chemo mechanical polishing at −1360 nm, −3640 nm and −4800 nm below the initial surface. Right side: Different junctions resulting from interaction between dislocations from different rosette arms (from Gaillard [149]).

In MgO, as in many other materials, an indentation size effect (ISE) is observed. This significant increase of the measured hardness for small indentations is often explained based on the Nix and Gao (NG) model [157] that relies on the concept of geometrically necessary dislocations (GND). In the NG model, the GNDs are contained into a hemispherical plastic zone with a radius equal to the contact radius. However,

WD EX1058
Western Digital v IP Bridge
Page 22

Feng and collaborators [158] observed that for a penetration depth lower than 200 nm, the NG model overestimates the hardness in MgO. Following the work of Gaillard and colleagues [154], they applied the nano-etching method to reveal dislocations around the indent and determine the size of an effective plastic zone. Then, they have shown that the plastic zone radius was higher than the contact radius for low penetration depth. They thus proposed a correction for the NG model to take into account the non self-similarity of the plastic zone for low penetration depth. This result was strengthened by the work of Huang and collaborators [159], even if they conclude that, for penetration depth as low as few nanometers, the model is no longer valid since hardness measurements are scattered because of discrete dislocations events. In 2009, Sadrabadi and coworkers [160] proposed a similar study of the ISE by nano-etching in CaF_2, another ionic crystal. Indentation size effect in MgO was also studied as a function of the temperature [161] and after ion irradiation [162].

4.3. Incipient Plasticity: Pop-In and Dislocation Nucleation

In the nano-indentation load–displacement curves, the first plastic event in load-controlled experiment is characterized by a pop-in phenomenon, i.e., an abrupt increase in the penetration depth [163–168]. In MgO, if the pop-in appears at different loads, it always makes the transition from an elastic behavior to an elasto-plastic regime characterized by a master curve. This is clearly illustrated by Figure 18 where different nano-indentation curves obtained with a Berkovich indenter in a (001) oriented MgO single crystal are superimposed. This phenomenon, which is observed in many different materials, has aroused a great interest since it is commonly associated to homogeneous nucleation of dislocations. It also must be pointed out that the nanometer scale volumes of material involved in these nano-indentation experiments are very well suited for mesoscopic and atomistic simulations [169–171].

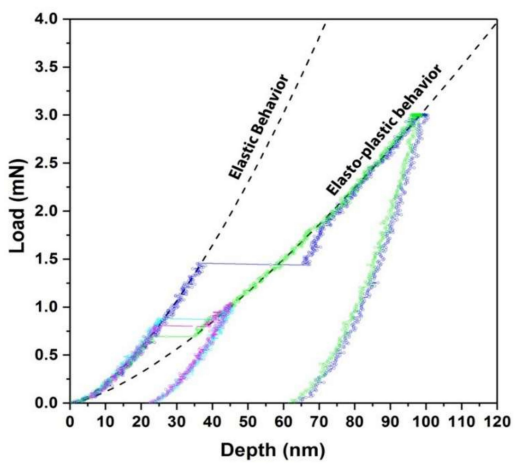

Figure 18. Superposition of nano-indentation curves in MgO (Berkovich indenter). A pop-in, which can appear at different loads, characterizes the transition from an elastic behavior to an elasto-plastic behavior.

Gaillard et al. [172] applied the nano-etching technique to study the dislocation structures nucleated during nano-indentation tests that are stopped just after the pop-in in both MgO and LiF. They first used a Berkovich indenter. In this case, they report that the dislocations are concentrated in a small volume below the contact area between the indenter and the surface. They concluded that, since a high number of dislocations are nucleated at the same time during the pop-in, dislocation interactions leading to Lomer locks should be enhanced, which impedes the dislocation propagation in the conventional rosette arm distribution. However, even if few dislocations are nucleated during the pop-in, their concentration is still high when using a Berkovich indenter because of the sharpness of the pyramidal tip. For a more accurate analysis of the dislocation nucleation phenomenon, Tromas and colleagues [153] used spherical indenters with radius of curvature of few micrometers.

In that case, the pop-in appears at very low penetration depth compared to the radius of the indenter. The ratio of the contact area over the penetration depth is thus higher than in the case of a Berkovich indenter. The dislocations structures nucleated during the pop-in with a spherical indenter are thus extremely simple since they are limited to only one or two pile ups of few dislocations. In this configuration, there are no (or few) dislocation reactions. Furthermore, the elastic contact between a sphere and a plane is well described by the Hertz law [173,174], and the stress field distribution can be determined analytically [175]. The dislocation structure can thus be compared to the stress field generated by the indenter at the beginning of the pop-in, when they were nucleated (Figure 19). From this comparison between the dislocation organization below the contact area and the mapping of the resolved shear stress acting on the activated slip systems, Tromas and colleagues concluded that these initial dislocation pile ups are nucleated at the point of maximum resolved shear stress, that is along the indentation axis at a depth of $0.44 \times a_c$, where a_c is the contact radius for the 1/2<110>$\{101\}_{45}$ slip systems, and at a radial distance of $1.1 \times a_c$ from the indentation axis and a depth of $0.65 \times a_c$ for the 1/2<110>$\{101\}_{45}$ slip systems [153].

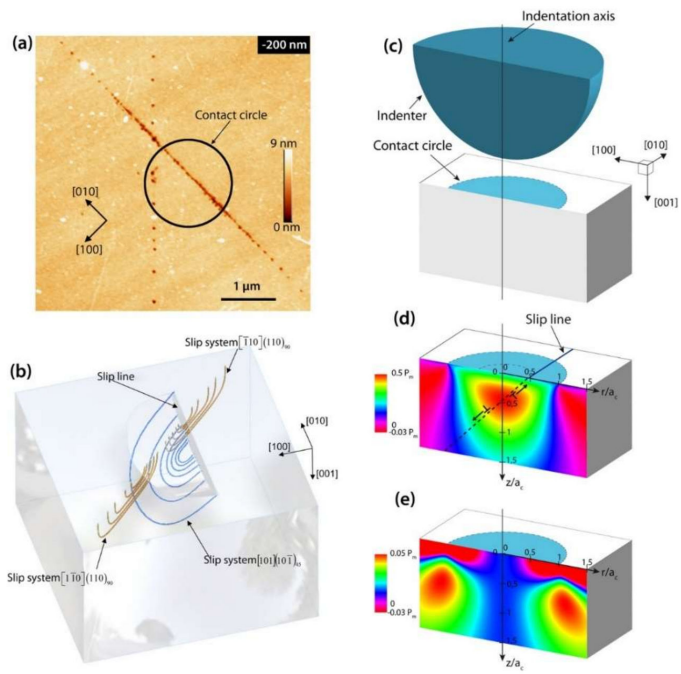

Figure 19. (**a**) Nano-etching pattern, after removing a layer of 200 nm by CMP, of a spherical nano-indentation stopped after the pop-in; (**b**) schematic of the corresponding dislocation structure; and (**c**–**e**) schematic representation of the resolved stress field (Equation (12)) in the slip systems <110>$\{110\}_{45}$ (**d**) and <110>$\{110\}_{90}$ (**e**). The stress field is presented in a plane of cross section (010) containing the indentation axis. The contact circle is represented in blue.

While it is admitted that the pop-in phenomenon corresponds in many materials to dislocation nucleation, there is still a debate on its nature: homogeneous or heterogeneous? The question is thus to answer if the nucleation process is favored by pre-existing defects or not. The experimental difficulty is thus to find a model material where the pre-existing defects can be accurately controlled and characterized prior to indentation. As developed before, MgO single crystals can be easily cleaved, with a simple hammer and a fine blade, providing flat and well oriented (001) surfaces. Under certain conditions, cleavage can also generate a high dislocation density in a very thin surface layer [176–181]. According to the previous work of Gilman and colleagues in LiF and MgO [179,180], Montagne and collaborators [182] used "slow" cleavage in MgO to generate dislocations in the subsurface, the dislocation density being measured by

WD EX1058
Western Digital v IP Bridge
Page 24

nano-etching. The surface was then carefully polished by CMP to reach regions with different dislocation density. With this method, it was thus possible to prepare flat (001) MgO surfaces with a controlled density of (pre-existing) dislocations. By performing spherical nano-indentation, they observed that the existence of pre-existing dislocations in the contact area between the indenter and the surface decreases the pop-in load. Dislocation nucleation is thus promoted by pre-existing dislocations. However, after a careful analysis of the dislocation structures by nano-etching, they showed that the effect of pre-existing dislocation was more complex than expected (see Figure 20). Indeed, the dislocations nucleated during the pop-in do not result from dislocation source activation or reactions with pre-existing dislocations. Furthermore, the organization of the dislocation structures during the pop-in is still consistent with a nucleation event at the point of maximum resolved shear stress, independently of the pre-exiting dislocations positions. They suggest that the influence of pre-existing dislocations should be linked to their displacement in the indenter stress field during the nano-indentation test.

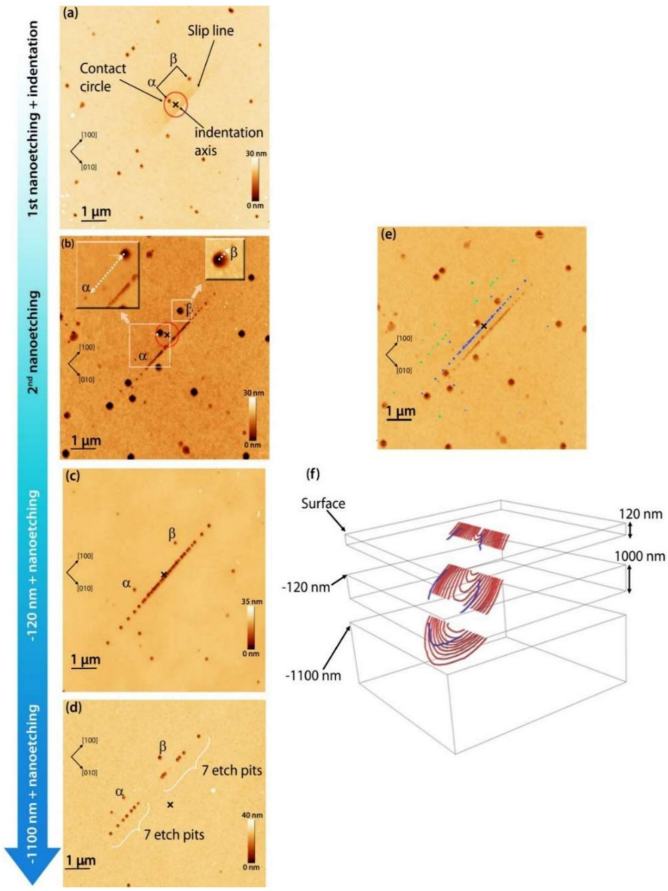

Figure 20. (**a**) Initial surface first etched to reveal pre-existing dislocations and then indented with a spherical indenter. The indentation was stopped after the pop-in; (**b**) Second etching on the initial surface to reveal the dislocations nucleated during the indentation. The pre-existing dislocation are clearly identified by bigger etch pits; (**c**) New nano-etching obtained after removing a layer of 120 nm by CMP; (**d**) New nano-etching after removal of a 1100 nm total layer. The pre-existing dislocation half loop $\alpha\beta$ does not interact with the dislocations nucleated during the pop-in. However, this initial half loop extends in the indenter stress field; (**e**) Superposition of the successive polishing and nano-ecthing stages; (**f**) Schematic representation of the dislocation structure. Images are adapted and reproduced from Ref. [182] with permission from Elsevier.

WD EX1058
Western Digital v IP Bridge
Page 25

4.4. Determination of the Lattice Friction Stress through the Dislocation Structure around a Spherical Indent

The complete analysis of individual dislocation positions in the indenter stress field can be used to measure specific mechanical properties of MgO. Gaillard and collaborators [183] performed spherical nano-indentation test in MgO, stopped just after the pop-in. They obtained very simple dislocation structure limited to two pile ups of few dislocations: a first one oriented along a <110> direction corresponding to dislocations emerging with an edge character, and a second one oriented along a <100> direction corresponding to dislocations emerging with a screw character. The structure consisted in dislocation half loops pile-up, so that the etch pits could be paired for each pile up. Then, similar pile-ups were analytically modeled considering that the stress acting on each dislocation is the sum of the external applied stress τ_a, the stress due to other dislocations in the pile-up τ_i, the image forces stress due to the surface τ_{im} and the lattice friction stress τ_f.

The external applied stress τ_a is the spherical indenter stress $\overset{=}{\sigma}^{ind}$ resolved on the dislocation slip system, $\overset{=}{\sigma}^{ind}$ being calculated by Hanson [175], Equation (12).

$$\tau_a = \sigma\left(\vec{b}, \vec{l}\right) = \frac{\vec{b}}{\|\vec{b}\|} \cdot \overset{=}{\sigma}^{ind}(x, y, z) \cdot \vec{n} \tag{12}$$

The stress due to other dislocations in the pile-up τ_i is defined by

$$\tau_i = \sum_{j \neq i}^{n} \frac{A}{x_i - x_j} \tag{13}$$

where x_i is the position of the dislocation i and A is defined by Equation (14):

$$A = \frac{\mu}{2\pi}\left(\cos^2\theta + \frac{\sin^2\theta}{1-\nu}\right) \tag{14}$$

with θ the angle between the Burgers vector $\vec{b}$ and the line direction $\vec{l}$ of the dislocation [184].

The Lattice friction stress τ_f is the parameter to be determined. This is thus a free parameter which is adjusted by comparing the analytical calculation and the experimental observations of the dislocation pile-up. At the equilibrium:

$$\tau_a(x_i) + \tau_{im}(x_i) - \tau_f + \sum_{j \neq i}^{n} \frac{A}{x_i - x_j} = 0 \tag{15}$$

In their calculation, Gaillard and coworkers introduced successively pairs of dislocation with opposite Burgers vectors to model dislocation half loop, at the point of maximum resolved shear stress, i.e., where they are supposed to nucleate according to the work of Tromas et al. [153]. Once all the dislocations were introduced in the calculation, the indenter stress field is progressively decreased to model the indenter unloading, and the pile-up relaxation is calculated. Finally, the calculated dislocation positions in the pile-ups are compared to dislocation etch pits (see Figure 21). This calculation was performed for different lattice friction stress values, until the calculated pile up length fits with the experimental observations. The lattice friction stress in MgO at room temperature is 65 MPa for edge dislocations and 86 MPa for screw dislocations i.e., values in the same range than {110} experimental CRSS measured under compression [14,18,21].

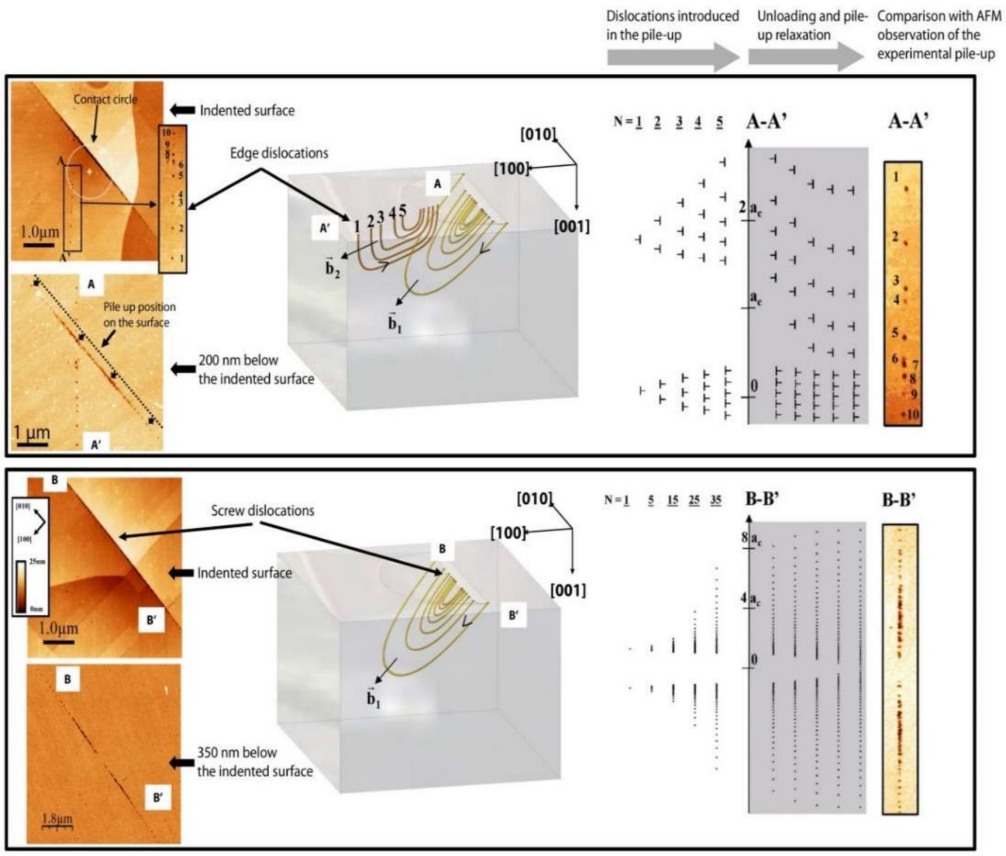

Figure 21. Dislocation structure induced by spherical nano-indentation in MgO stopped just after the pop-in: (**top**) analysis and modeling of a pile up of edge dislocations; and (**bottom**) analysis and modeling of a pile up of screw dislocations. Images are adapted and reproduced from Ref. [183] with permission from Elsevier.

4.5. Plasticity in MgO and Other Ionic Crystals Studied by Micro-Compression

Indentation of MgO was used extensively to study its deformation mechanisms. However, although brittle fracture can be suppressed owing to the confining pressure [185,186], there are certain drawbacks. The most important one is that it is not possible to directly distinguish the contributions of the soft ½<110>{110} slip systems and the hard ½<110>{100} slip systems unless a modeling approach is used in conjunction with experiments on different crystal orientations [187]. The reason for this is that the three-dimensional deformation underneath the indenter requires deformation on several independent slip systems. The magnitude of the hardness often corresponds most closely to the estimate of the room temperature hardness of the hard slip system, justified as this system may be the limiting component in achieving the required deformation [188]. In contrast, the slip traces observed at the surface belong to the soft slip system [145], which appears to accommodate the majority of the deformation. Therefore, the hard slip system may only be identified by TEM, where the sample preparation and large dislocation densities in indentation render such observations difficult [188]. Deformation after indentation in the hexagonal and therefore intrinsically anisotropic GaN as well as in MgO are shown in Figure 22 to illustrate this effect.

WD EX1058
Western Digital v IP Bridge
Page 27

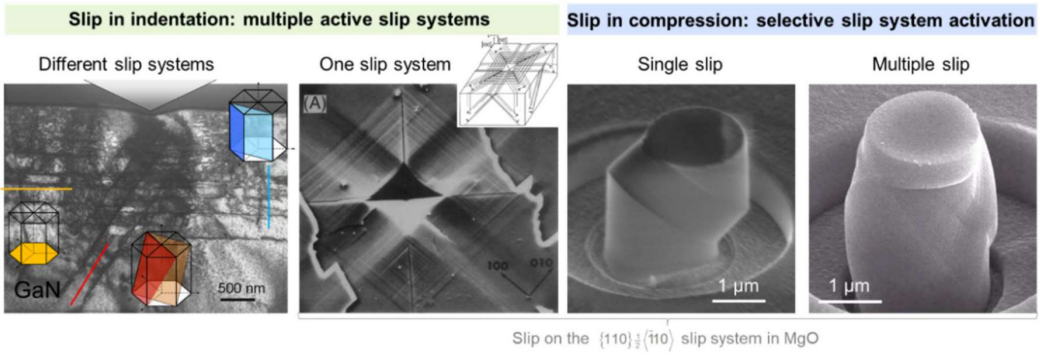

Figure 22. Geometry of slip in indentation and micro-compression. In indentation, multiple slip systems are always required and may result in the activation of several equivalent (e.g., in MgO [145] or very different systems, GaN [189]). In micro-compression, as in any single crystalline compression test, both single (here MgO near [001]) and multiple slip orientations (here MgO aligned with [110], see Ref. [190]) may be interrogated. Images are adapted and reproduced with permission from K. McLaughlin [189], John Wiley and Sons, Inc. [145] and Cambridge University Press [190].

The simplest approach to avoid this issue is to change the test geometry and use uniaxial stresses on single crystals instead. In uniaxial compression, CRSS on the individual slip mode may then be obtained, as collated in Figure 2 from macroscopic tests. Unfortunately, this approach is limited to conditions in which plastic deformation by dislocation glide is favored over cracking. For compression along soft directions, in which the ½<110>{110} slip systems are activated, this is nearly always the case. In contrast, in the hard direction near a [111] compression axis, where the Schmid factor on the soft system diminishes, the uniaxial stress has to be increased until the CRSS of the ½ <110>{100} system is exceeded. At low temperatures, this is normally preceded by the occurrence of fracture, such that no CRSS for dislocation glide can be obtained. In Figure 2, this is evident from the lack of data without cracking below 650 K [3,5]. In recent years, a new approach in mechanical testing has emerged, which overcomes this challenge of suppressing brittle fracture at low temperatures: the down-scaling of samples to the micrometer range in the so-called micro-compression technique [191,192]. As a general trend, the idea is to test samples with a size lower than that of the plastic zone to favor ductility before failure. More precisely, in uniaxial tests at small scales, cracking is suppressed due to two reasons [193]: (i) small samples are statistically less prone to contain critical pre-existing flaws or these would be more easily visible prior to testing; and (ii) where no pre-existing cracks exist, these have to be nucleated and extended in order for fracture to occur. Analyses of the second point have shown that indeed, fracture is often suppressed in small specimens and that if it does occur it is where slip bands intersect (Figure 23) [190,193–195]. This is also seen in macroscopic observations of deformed MgO [196] (Figure 23) and the geometry of slip then determines the nucleation of cracks. It can be shown that a size effect exists where a crack splitting a pillar through the middle and that this may be exploited to suppress unstable crack growth [193,194,197]. The most favorable condition for this is single slip [193]. However, even where this cannot be achieved or multiple slip conditions are reached, a size effect is nevertheless observed, resulting effectively in a substantial reduction of the brittle-to-ductile transition temperature with size, i.e., the competition between deformation by cracking and dislocation glide is shifted in favor of the latter. In testing micropillars at different temperatures, this was shown on $MgAl_2O_4$ spinel [198], where plastic deformation was achieved more than 1000 °C below the macroscopic brittle to ductile transition temperature. The yield stress required to initiate substantial dislocation glide in small volumes increases as the size decreases towards and below the μm regime [199]. However, this increase is relatively small in intrinsically hard materials [200–202] and the critical stress for cracking increases more sharply [193,197].

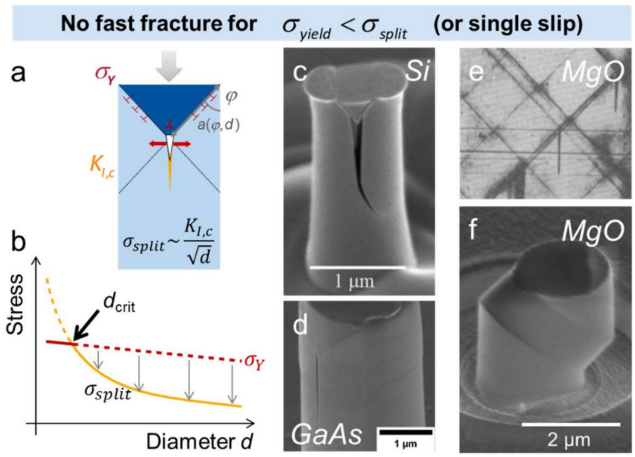

Figure 23. Suppression of unstable fracture in micropillars: (**a**) schematic drawing of the model relating size, slip geometry and the splitting stress; (**b**) the size effects on critical stresses for a typical hard crystal showing a transition from failure to plastic deformation; and an experimental geometry of this type in (**c**) silicon and (**d**) GaAs as well as (**e**) at slip band intersections in macroscopic experiments in MgO. In single slip orientation fracture can then be suppressed to the largest diameters, shown here for MgO in (**f**). Figures in (**c**) [195], (**d**) [193], and (**e**) [196] reprinted with permission from Wiley, Taylor & Francis and Springer.

The micro-compression technique is therefore exceedingly powerful in resolving the deformation mechanisms at temperatures below the macroscopic brittle to ductile transition temperature in brittle materials, such as MgO, and also those which are difficult to obtain in bulk form, such as coatings, manipulated surface layers, complex materials or phases which cannot be solidified as single crystals from the melt [203–205].

A schematic illustration of the application of this method is given in Figure 24 and a review covering its use on a much wider range of brittle crystals may be found in reference [200].

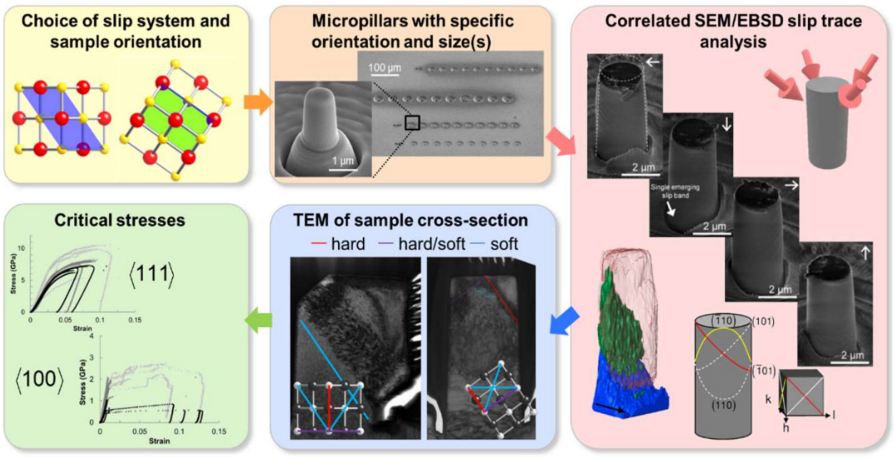

Figure 24. Schematic representation of a study of deformation mechanisms by micro-compression and electron microscopy. After the choice of crystal orientation, pillars or specific size(s) are milled and typically analyzed by SEM and EBSD. Where fracture is successfully suppressed TEM can further elucidate the operative deformation mechanisms to correlate these with the stress–strain curves collected during the experiment. SEM [206] and TEM [201] images as well as 3D-EBSD results [206] and stress–strain curves [201] reprinted with permission from Elsevier and Taylor & Francis.

WD EX1058
Western Digital v IP Bridge
Page 29

This section is divided into three subsections: measurements of CRSS in MgO and related crystals at room temperature using micro-compression, studies of the thermal activation of dislocation motion in micro-compression and the extension of the technique to compression of nanocubes, where dislocation nucleation governs deformation.

4.5.1. Measurements of CRSS in MgO and Other Rock-Salt Crystals at Room Temperature

Micro-compression experiments on single crystals allow the individual activation of the soft and hard slip systems. The <111> orientation requiring the hard slip mode to operate is of particular interest due to the difficulties outlined above in testing macroscopically at low temperatures. The critical resolved shear stress of MgO for both slip modes, using crystals compressed in <100>, <110>, and <111> direction, was determined by Korte and collaborators as shown in Figure 25. Similar results were reported by Zou and Spolenak for compression along <100> in MgO [207]. As expected, the CRSS on the soft mode is strongly overestimated owing to the size effect on dislocation glide. Several studies covered the current understanding of this effect that is generally thought to be governed by the effective dislocation line length and its statistical variation in a small volume [192,208], the exhaustion of dislocation due to escape at the surface [209], image forces [210], the nucleation of partial dislocations without the need to activate the trailing partial for slip distances in the pillar in the order of the dissociation length [211] and finally the effect of Focused Ion Beam (FIB) induced defects on dislocation nucleation and confinement [197]. In contrast to the soft slip system, the CRSS on the hard slip system shows excellent agreement with an extrapolation of the macroscopic values towards room temperature. This is consistent with findings in other hard materials [200] and with the idea that on the hard slip system, the lattice resistance governs the magnitude of the yield stress and the effect of changes in line length is relatively weak [133,200,201] as the relevant dimensions are of the order of a kink pair. This is shown for a selection of materials ranging from metals over semiconductors to oxides.

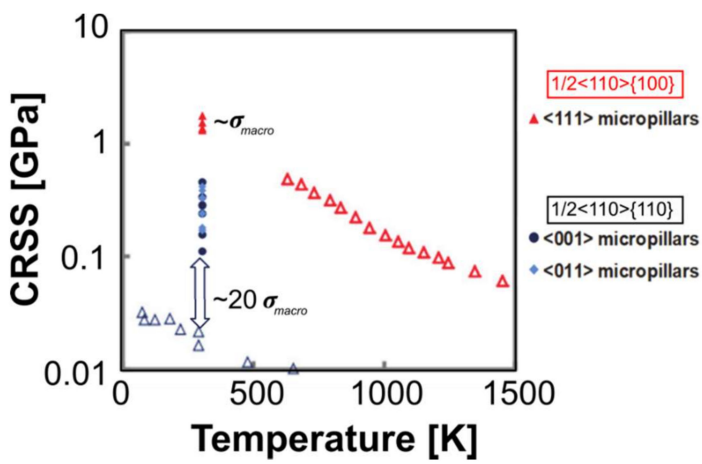

Figure 25. The critical resolved shear stress of the soft 1/2<110>{110} and the hard 1/2<110>{100} slip systems in MgO measured by micro-compression at room temperature along the <100>, <110> and <111> orientations compared with measurements on macroscopic single crystals in <100> and <111> orientation. A size effect on CRSS is observed on the soft slip system, while the previously unavailable data on the hard slip system correspond well to the extrapolation from higher temperatures due to its higher intrinsic stress level. Data from references [3,5,201].

This difference in the effect of size can be rationalized rather simply: most models of plasticity size effect for a size regime of a few micrometers, i.e., where dislocation motion and multiplication rather than nucleation are thought to be the dominant mechanism, consider the importance of only a limited number and truncated single armed sources. Using such a model, a first estimate of the expected effect of size

may be made using the statistical source length suggested by Parthasarathy and colleagues [212] with the average source length λ taken as 0.2 times the pillar diameter. This leads to a stress contribution, most simply assumed to be additive to the bulk strength, of the order of $Gb/2\lambda$, where G is the shear modulus. Taking a commonly used pillar diameter of 2 μm, a shear modulus of $G_{\{110\}}$ = 101 GPa and $G_{\{100\}}$ = 155 GPa for the two slip systems this amounts to 38 and 58 MPa on the soft and hard slip system, respectively. This is of the same order of the expected CRSS in macroscopic crystals in the case of the soft slip mode, while in the case of the hard slip systems, the contribution would be approximately 5% of the room temperature value extrapolated from macroscopic high temperature data. Of course, the effects of ion milling point and line defect densities and types, contributions of dislocation nucleation stresses, the uncertainties in the pillar dimensions at small scales, their taper and the resulting inhomogeneous stress state (which may give much higher local strain rates) are neglected in this simple estimate. Note that, in the data shown in Figure 25, the effect of FIB damage should be approximately constant as the same material is milled and simply compressed in different crystal directions. Despite these simplifications, this estimate does, however, illustrate in an easy manner why a much stronger size effect is to be expected on the soft slip system, even if the exact size of the effect is in fact still under debate in the literature. The importance of the lattice resistance, governing the bulk strength above which a size effect becomes significant or not, was also shown using tests at different temperatures in LiF [133] and other materials, such as bcc metals [213,214]. Owing to the large difference in CRSS it is of course important to verify the operation of the hard slip system (normally achieved by TEM, as in reference [201], see Figure 24) and address potential artefact encountered due to imperfect misalignment. In MgO, 3D-EBSD was used to track deformation on secondary systems not detectable by surface trace analysis [206]. Taking LiF as a model material, Soler and coworkers [215] assessed the effect of misalignment in experiment and finite element models and Kiener and collaborators [216] collated a general review on experimental constraints specific to micro-compression. Across these high strength materials, a challenge remains to clearly distinguish the contributions of dislocation glide and nucleation regarding the measured stresses. Indeed, the underlying activation volumes and critical stresses are much closer than in the metals and surface alteration, e.g., by oxidation or FIB milling, is known to influence the measured stress level and its scatter [197].

4.5.2. Rate and Temperature Dependence in Other Ionic Rock Salt Crystals

Following these initial tests initiated on MgO, there was a wider effort to characterize the ionic rock salt crystals with LiF in the focus [133,215,217] using the same approach and including variable temperatures [206,218,219] and rates [220,221] with a combination with simulation [133]. An excerpt from these works is shown in Figure 26, highlighting the characteristics of the micro-compression tests described above for MgO: an increase in flow stress with size, which becomes more pronounced as the temperature is increased and, hence, the lattice resistance reduced [113,133]. A drop in stress level consistent with thermal activation of lattice resistance controlled flow is confirmed in elevated temperature tests [133] and variable rate tests yield an appropriate activation volume of several b^3 [133]. A fit to a theoretical model describing the bulk strength, lattice resistance and size distributions separately indeed also explains these results quantitatively (Figure 26b) [133].

WD EX1058
Western Digital v IP Bridge
Page 31

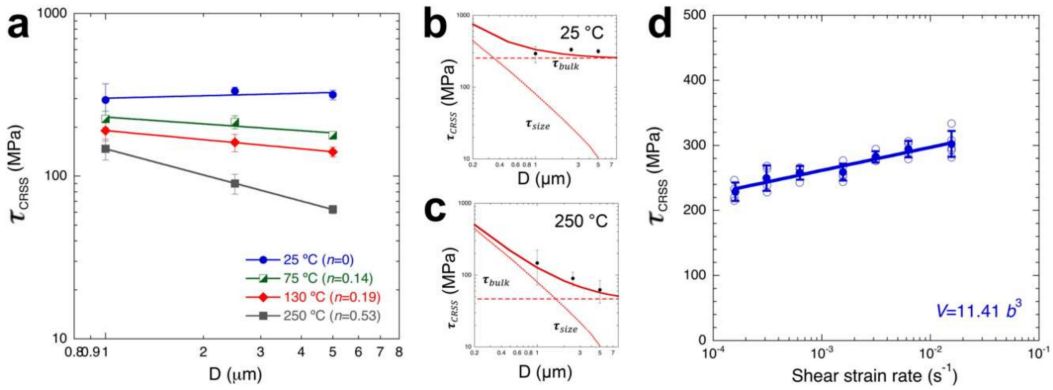

Figure 26. The effects of temperature, strain rate and size in LiF. (**a**) Experiments and discrete dislocation dynamics simulations showing the drop-in flow stress with temperature and increasing size effects towards lower overall stresses. These results are consistent with a size (source controlled) term and a temperature dependent bulk term (governed by the lattice resistance) contributing to the measured stresses at both (**b**) room and (**c**) elevated temperature. (**d**) Strain rate jump tests offer a consistent view with an activation volume of the order of 10 b^3. Figures reproduced from Ref. [133] with permission from Elsevier.

4.5.3. Dislocation Nucleation in Small MgO Volumes

Although the samples tested by micro-compression are very small, the volume is normally not dislocation free, particularly where it was milled by FIB, or possesses a roughened surface from etching [133] or lithography [222]. However, in some cases, it is possible to produce pristine samples which allow the investigation of this rarely accessible regime [223–225]. Issa and colleagues [224] were able to obtain pristine MgO nanocubes from burning Mg chips in air, tested them in-situ in the TEM and compared these results with MD simulations [224,226] (Figure 27). In both simulations and experiments, the expected dislocations on the softer {110} planes are observed and nucleation occurs at the expected locations, i.e., the edges and corners of the cubes. In contrast to other tests, the modeled nucleation stress is very high and a substantial curvature of the dislocation lines is observed (especially in the simulation). Thus, the dislocation microstructures observed at the nanoscale, under a compression stress in the GPa range, may therefore appear more similar those found at high temperatures [224].

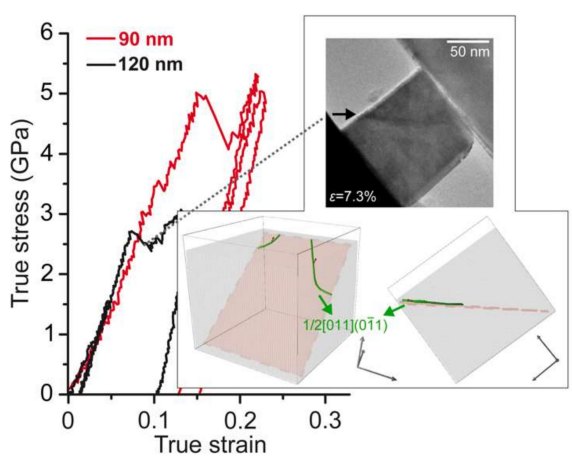

Figure 27. Experiments in initially dislocation free MgO nanocubes inside the TEM. Stress–strain curves and a corresponding TEM image at 7.3% strain with two MD simulation snapshots are showing ½<110>{110} dislocations, which are in green. Figure reproduced from Ref. [224] with permission from Elsevier.

WD EX1058
Western Digital v IP Bridge
Page 32

In this section, we outline how various nano-mechanical methods in conjunction with electron and atomic force microscopy were used to unravel the dominant plastic deformation mechanisms in MgO. The local deformation, when limited to its very early stages, allows individual dislocation analysis. A particular strength of these methods is the ability to extend the measurable range to room temperature even in the hard directions. In micro-compression, a size effect on fracture facilitates the study of plasticity, while, in indentation, it is the confining stress field provided by the surrounding material that suppresses cracking. In this context, and in other common high-pressure situations for MgO, such as in the Earth's mantle, it is important to also understand the effect of hydrostatic pressure on the crystal and the resulting deformation mechanisms. These is reviewed in Section 5.

5. High-Pressure Plasticity in MgO

Hydrostatic pressures in the GPa range induce drastic changes in the electronic, structural, and mechanical properties of materials. A simple ionic salt such as NaCl, for instance, transforms from the classical rock-salt structure (B1) into a cesium chloride structure (B2) at 20 to 30 GPa [227]. CsI, another simple ionic salt at ambient conditions, transforms to a hexagonal-closed-packed structure at ca. 50 GPa [228]. In addition to this structural transition, CsI transforms from an insulator to a semi-conductor at pressure of about 55 GPa and becomes metallic above ~100 GPa [229,230]. As such, hydrostatic pressure can have a profound influence on the properties of matter.

MgO remains in the B1 structure over a wide pressure and temperature range. Recently, it was shown that the B1 to B2 phase transition in MgO occurs at pressures of the order of 400–600 GPa [231,232] and that it becomes metallic at even higher pressures [231]. Nevertheless, pressure already influences the properties of MgO even below these extreme values. For instance, the elastic anisotropy of MgO reverses close to 15 GPa [233]: below 15 GPa, longitudinal and shear-wave propagations are faster along [111] and [100], respectively, whereas above 15 GPa, the corresponding fast directions are [100] and [110]. Based on considerations on elasticity and electronic polarizability, it was suggested that the primary slip plane of MgO would change from {110} to {100} at increasing pressures [234].

The effect of pressure on materials properties can be counter-intuitive. It can also serve as a test of current modeling capabilities and has implications for Earth and planetary sciences. As such, plastic properties are being studied at pressures in the 10s of GPa range and above. This section reviews current methods for such experiments, their capabilities/limitations and application to MgO. Recent outcomes from simulations are be discussed.

5.1. Methods for HP Experiments and Simulations

5.1.1. Experimental Devices

The deformation-DIA (D-DIA) [235], Rotational Drickamer Apparatus (RDA) [236], and newly developed Deformation T-Cup (DT-Cup) [237] are the three main large volume presses (LVP) used for high pressure plasticity studies. All allow the controlled deformation of millimeter size samples. The D-DIA is designed for deformation at constant pressure, both compressional and extensional, at strain rates between 10^{-3} and 10^{-7}/s and, currently, up to 18 GPa and 1900 K [238]. The DT-Cup allows for controlled deformation in axial geometry with experiments at about 20 GPa at 300 K and 10 GPa at 1100 K [237]. Finally, the RDA allows a large rotational shear deformation of the sample up to pressures and temperatures over 27 GPa at 2150 K [239]. In the D-DIA and DT-Cup, the stress boundary acting on the sample is axial [240] while, in the RDA, it may be considered as a combination of simple shear and axial compression [241]. Depending on experiments, strains are measured directly using X-ray radiography or can be reconstructed from changes in sample pressure or based on markers placed inside the sample.

LVP allow for controlled deformation experiments but their P-T range does not yet reach over 30 GPa. The DAC, on the other hand, in combination with heating methods reach the terapascal at ambient temperature [242] and 350 GPa at 6000 K [243]. DAC may not only impose pressure but also

WD EX1058
Western Digital v IP Bridge
Page 33

a compressive stress that produces elastic and plastic deformation. A limitation of the DAC is that pressure and deformation cannot be decoupled. Despite these limitations, the DAC is a useful tool for investigating plastic properties up to 300 GPa at ambient temperature [244] with developments under way to allow for performing high-T experiments, either using resistive heating elements [245] or lasers [246]. Stress in DAC experiments is typically assumed to be axial with cylindrical symmetry around the compression direction [247] and with low pressure gradients across the sample. Note that this assumption relies on the use of small samples and gasket confinement, unlike older experiments that did not confine the sample within gaskets [248]. Sample strain along the diamond direction is compressive. Radial strain is dependent on sample, gasket, and sample loading.

5.1.2. Data Collection

Because of structural and physical changes induced by P and T, analytical methods that can be used in-situ as the sample is being deformed are often preferred. These in-situ analyses rely on synchrotron radiation, either in the form of X-ray diffraction (XRD) or X-ray radiography (Figure 28).

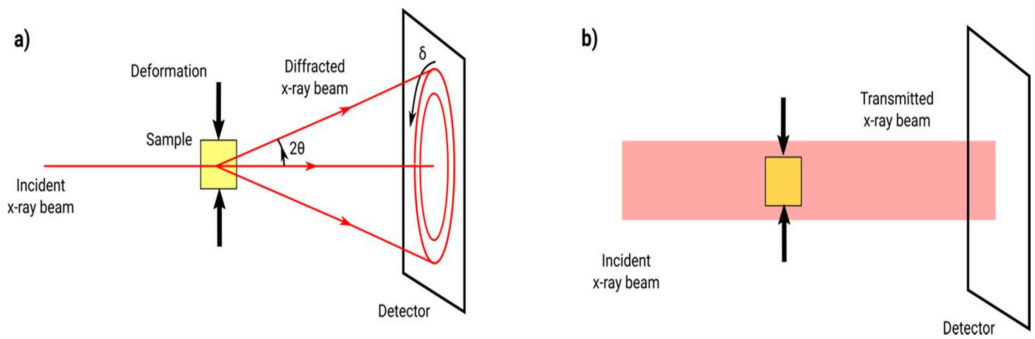

Figure 28. Geometry for in-situ X-ray diffraction and radiography in high pressure deformation experiments. The sample is deformed inside a high-pressure device (not shown) with the direction of deformation perpendicular to the incident X-ray beam. In diffraction mode (**a**), the incident beam is smaller than the sample and diffraction is collected on a detector perpendicular to the incident beam. Features of the diffraction image are analyzed as a function of the azimuth angle δ. In imaging mode (**b**), the incident beam is larger than the sample and its shape and dimensions can be measured on the detector.

Typical experiments tend to investigate average properties inside a polycrystal, including strain and strain rate, average stress, and texture. Others focus on single-crystals. In this case, experiments measure the sample strain, strain rate, and average stress. In the D-DIA, RDA, and DT-Cup, sample strain and strain rates are measured using X-ray radiograph images of the sample [249] (Figure 28). Similar measurements were performed in the DAC in the radial diffraction geometry [250] with limited use, however, since sample deformation is not controlled.

Deviatoric stress and texture are keys to quantify the plasticity of materials such as MgO. The stress itself provides information about strength and can yield flow laws when combined with information on strain rate. In-situ measurements of stress rely on methods derived from XRD residual stress analysis [251]. The basic principle is that the macroscopic sample stress induces a distortion of the Debye diffraction rings, resulting from elastic strains within the sample. The elastic strains vary with orientation relative to the applied stress direction and can be used to invert the macroscopic stress (Figure 29).

When a material deforms plastically, grains rotate under the action of dislocation glide on a given plane. This gives rise to lattice preferred orientations (LPO) or texture. In a textured material, diffraction intensities vary with orientation (Figure 29) and this can be used to invert the sample LPO [252].

WD EX1058
Western Digital v IP Bridge
Page 34

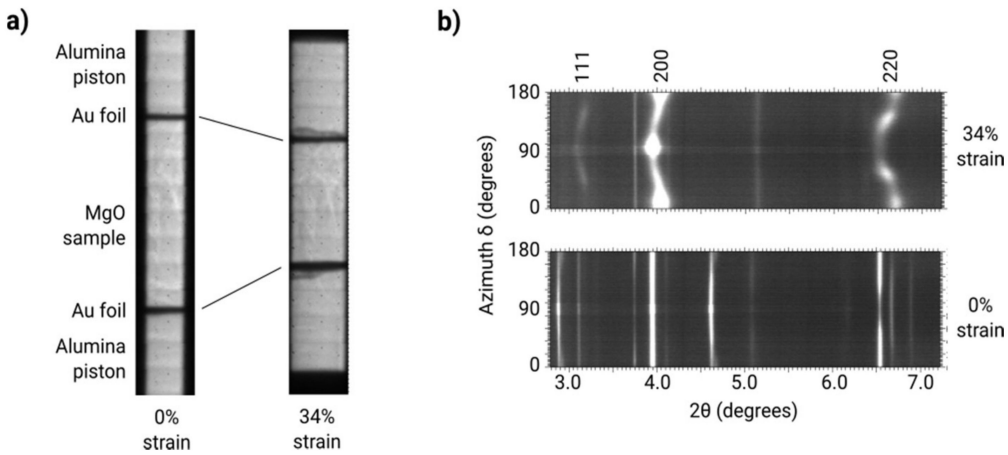

Figure 29. Typical in-situ X-ray data, collected on polycrystalline MgO at 2–5 GPa and 300 K at the ID06 beamline of the ESRF [253]: (**a**) X-ray radiograph for measuring the sample size and macroscopic strain; and (**b**) X-ray diffraction after 0% and 34% axial strain. Diffraction peaks of the MgO sample are labeled. Other peaks are from the sample assembly. Variations of diffraction intensity with azimuth are related to LPO. Variations of peak positions with orientation are a measure of the local state of strain.

5.1.3. Data Analysis and Polycrystalline Simulation Methods

Stress estimation from the diffraction data are often performed using equations derived from linear elasticity [241,252,254]. However, there are limitations, as these equations do not account for plastic deformation. Plastic deformation induces a local relaxation of stress, leading to inconsistent stress interpretations with purely elastic models [255]. Plastic deformation can be modeled, e.g., by comparing the strains measured using XRD to results of elasto-plastic or elasto-visco-plastic self-consistent (EPSC or EVPSC) calculations that account for both elastic and plastic relaxation [253,255,256] (see below). Assuming that the experimental textures arise from plastic deformation, they can also be compared with the same polycrystalline plasticity simulations to obtain information about the deformation modes operating in the sample [252]. Atomistically-informed crystal plasticity finite-element modeling (CPFEM) can also be used to investigate the polycrystalline mechanical response as well as the texture evolution [257].

E(V)PSC calculations rely on effective medium self-consistent methods, which treat each grain of the polycrystal as an inclusion in a homogeneous but anisotropic medium (Figure 30). The properties of the medium are determined by the average of all the inclusions. At each deformation step, the inclusion and medium interact and the macroscopic elasto-plastic properties are updated iteratively until the average strain and stress of all the inclusions equals the macroscopic strain and stress.

CPFEM produces the full-field response of the heterogeneous deformation inside a representative volume element (RVE) of the polycrystalline aggregate [258]. Each grain is discretized into a large number of finite elements and the stress response is computed at each integration point while accounting for the local crystal orientation and constitutive equations. Consequently, each grain deforms heterogeneously and the average stress and strain per grain depend on both the local lattice orientation and the interaction with neighboring grains.

Parameters for both CPFEM and E(V)PSC are the sample starting texture, elasticity, applied deformation, and plastic deformation modes. In their coupled XRD-EVPSC approach, Lin and collaborators [253] optimize the agreement between experiments and simulations adjusting the list of active deformation modes and their physical properties, i.e., their CRSS, including (sometimes) effects of hardening. Comparisons between experimental and simulated textures (using VPSC, for instance) allow constraining the relative CRSS of the deformation modes. Comparison between experimental and simulated microscopic strains (as measured from diffraction) using E(V)PSC allows constraining the absolute values of the CRSS.

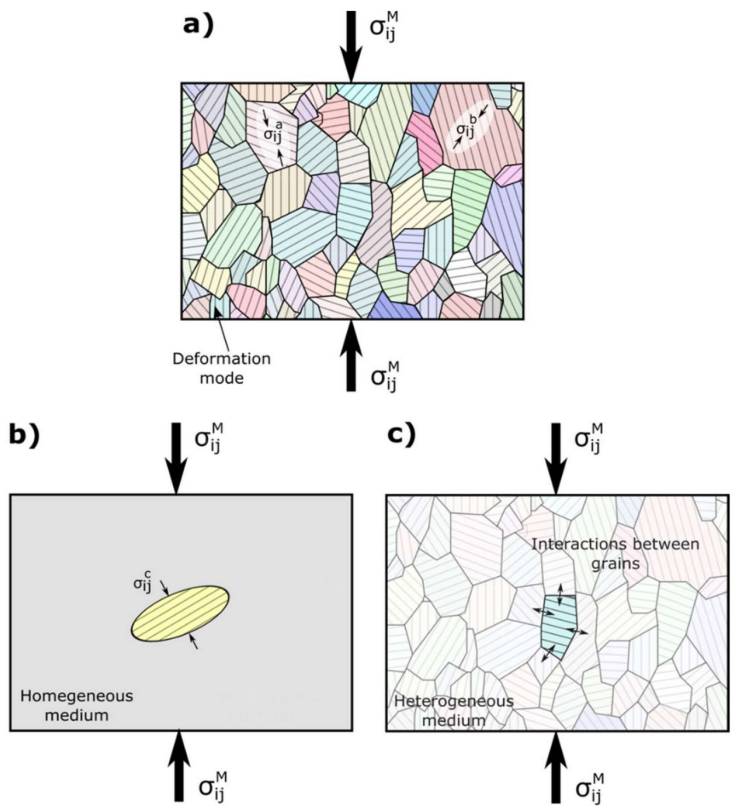

Figure 30. Polycrystalline simulation. (**a**) In a polycrystal, stress and strain distributions are heterogeneous. The behavior of each grain depends on its local environment, elastic, and plastic properties; (**b**) In self-consistent models, each grain is treated as an elliptical inclusion inside a homogeneous medium; (**c**) In CPFEM, while the whole polycrystal deforms according to boundary conditions, each grain deforms due to a full-field approach where all grains are considered.

Finally, TEM is the method of choice for characterizing individual deformation mechanisms such as dislocation types and microstructures for materials that are stable or can be brought back to room pressure [259]. It can be used to analyze the types of deformation modes present in the sample but also their arrangements and interactions [260]. As shown Sections 1 and 4, microscopy in the TEM or in the SEM can also be used to characterize the grain sizes, shapes, and orientation distributions [253].

5.1.4. Effect of Pressure on Rheological Laws

The effect of pressure on materials rheology is typically analyzed using rheological laws such as Equation (16).

$$\dot{\varepsilon} = A\tau^{n} exp\left(-\frac{Q + PV^{*}}{RT}\right) \tag{16}$$

where $\dot{\varepsilon}$ is the strain rate, A is a constant, τ is the differential stress, n is the stress exponent, Q is the activation energy, P is the hydrostatic pressure, V^{*} is the activation volume, R is the gas constant, and T is the temperature. In experiments, $\dot{\varepsilon}$, P, T, and τ are measured. A, n, Q, and V^{*} are obtained using fits of Equation (16). In such formulation, the effect of pressure on rheology is captured by the value of the activation volume.

WD EX1058
Western Digital v IP Bridge
Page 36

5.2. High-Pressure Plasticity of MgO and Iron Bearing (Mg,Fe)O

First, note that all experimental results presented below were performed at the strain rates attainable in a static deformation experiment, between 10^{-6} and 10^{-4}/s. All quoted results are hence given for these ranges of strain rates. Furthermore, the review is extended here to polycrystalline MgO that is more adapted for high pressure plasticity and $(Mg_x,Fe_{1-x})O$ as the effect of Fe is relevant for deep planetary interiors.

5.2.1. Effect of P and T on MgO and (Mg,Fe)O Deformation Textures

Polycrystalline MgO compressed at ambient temperature up to ~50 GPa shows textures with a concentration at 001 (Figure 31). A comparison between these observations and simulations using VPSC models indicate that such textures are compatible with slip on ½<110>{110} [252,253].

In the study of Amodeo and colleagues [261], the authors investigate the pressure sensitivity of dislocation cores in MgO from ambient up to 100 GPa hydrostatic *P* using the multi-scale modeling approach described Section 2. Due to the increase of *P*, the ½<110> screw dislocation (the main character for plasticity in MgO) reconstructs to further spread in the {100} slip planes at pressures larger than 30 GPa. This pressure-induced atomic reconstruction induces a relative hardening of the ½<110>{110} slip mode when compared to ½<110>{100}, i.e., at the grain scale, ½<110>{100} slip becomes easier than ½<110>{110} at high-pressure (see Figures 32 and 33).

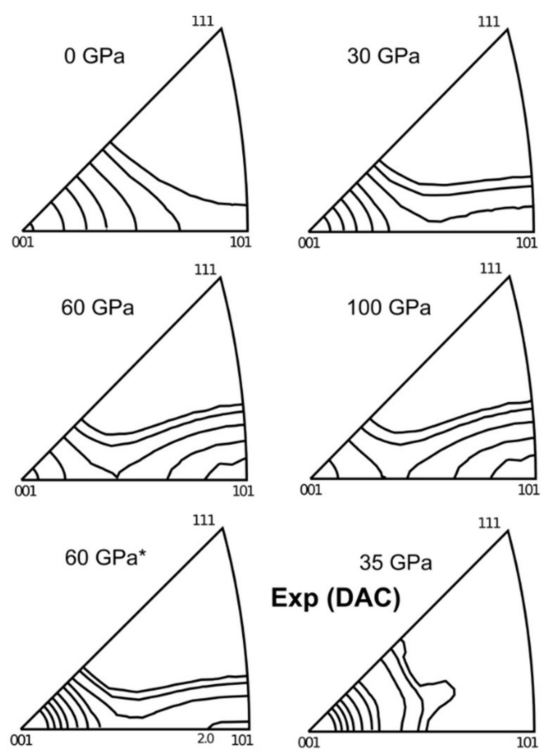

Figure 31. Illustration of polycrystalline MgO compression textures (IPF of the compression axis) at various pressure modeled using the CPFEM approach, starting from a random distribution of crystal orientations. Adapted from Ref. [257]. Black lines refer to grain orientation intensity; hydrostatic pressure is indicated at the top left of each subfigure; and "60 GPa*" refers to a test for which the sample starting texture was focused at 001 rather than random. The Exp (DAC) subfigure is adapted from the experimental work of Merkel and collaborators [252].

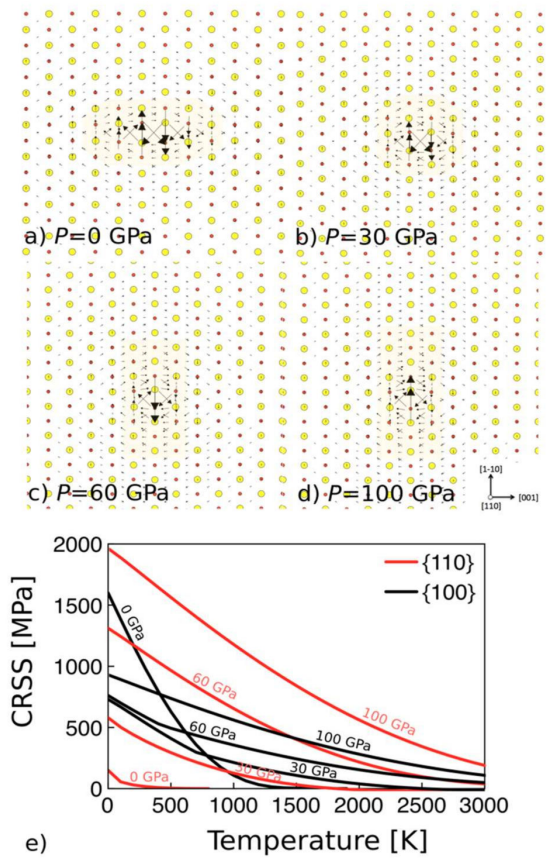

Figure 32. Screw dislocation core (relative displacement mapping) and CRSS evolution under hydrostatic pressure computed using the multiscale modeling approach of Amodeo and collaborators [23,261]. (**a**–**d**) Screw dislocation core structure from ambient up to 100 GPa pressure computed using the PNG model (see Section 2). Size of arrows refer to the relative displacement amplitude of core atoms. Yellow regions emphasize larger atomic displacements. They show the core spread variations i.e., from {110} spread at low-P to {100} at high-P. (**e**) CRSS for ½<110>{110} and ½<110>{100} slip modes computed for various pressure conditions. Results adapted from [23,261].

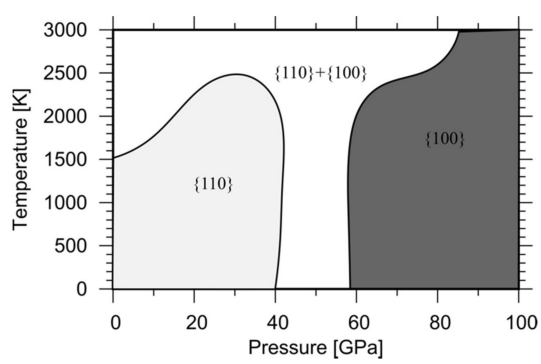

Figure 33. Illustration of the predicted slip system activity in MgO single crystal vs. pressure and temperature based on the multi-scale modeling approach of Amodeo and collaborators. Light and dark grey areas refer to ½<110>{110} and ½<110>{100} as dominant modes, respectively, while the white region draws a PT region where both slip modes are effective. Adapted from [23,261].

WD EX1058
Western Digital v IP Bridge
Page 38

Nevertheless, this pressure-induced transition remains difficult to observe experimentally, with confirmations in single crystal experiments [262] and in (Mg,Fe)O polycrystals at high temperature [263] (see below). At 300 K, the reported texture maxima tend to remain at 001 [252,264]. In fact, recent atomistically-informed CPFEM simulations including a constitutive model parameterization based on Figure 32 data [261] show that polycrystalline textures are not as sensitive to P as expected. Indeed, similar to the discussion in Section 4.5, the plastic activity in MgO polycrystals cannot be restricted to a single mode, neither of the suggested slip modes provides enough freedom degrees to accommodate the polycrystal macroscopic deformation. In CPFEM simulations, the transition from dominant {110} to dominant {100} slip induces only slight texture variations from 001 compression texture at low-P to 001 + 011 texture at high-P rather than a strict mode transition (Figure 31). It should also be noted that the strong 001 compression texture induced by slip on {110} early in the compression in DAC experiments could inhibit further texture evolution in experiments, even if slip on {100} becomes dominant at higher pressures as confirmed by the simulation [257].

The addition of Fe into (Mg,Fe)O lowers the strength of the 001 compression textures with the apparition of a secondary maximum at 011 for large Fe contents [265]. This could be associated to a decrease of activity on ½<110>{110}, but also the fact that, as (Mg,Fe)O is more compressible than pure MgO, a larger portion of the strain is accommodated elastically. Between 40 and 80 GPa, Fe in (Mg,Fe)O undergoes electronic spin-pairing transition from a high-spin to a low-spin state [266]. The pressure at which this transition occurs depends on stress state and exact Fe content of the material. It was shown, however, that the 001 compression texture maximum remains in $(Mg_{0.83}Fe_{0.17})O$ compressed through the spin transition up to 81 GPa [267], indicating that the spin transition in Fe has a limited effect on the plasticity of (Mg,Fe)O.

Deformation textures were also investigated at higher temperatures but lower pressures. At 300 MPa and up to 1400 K, $(Mg_{0.80}Fe_{0.20})O$ shows 001 and 011 compression textures [57]. This suggests that temperature plays a relevant role on deformation mechanisms of this material as this type of textures could be induced by a switch of dominant ½<110>{110} to dominant ½<110>{100} slip at higher temperatures. Shear deformation of (Mg,Fe)O also shows a change of textures with increasing Fe content with a clear transition when the Fe content reaches 50% [264,268]. This indicates that indeed, Fe-content does affect the plastic behavior of (Mg,Fe)O although the microscopic interpretation of this effect of Fe on the fundamentals of plasticity in (Mg,Fe)O and dislocation structure remains to be understood.

High-strain shear deformation of $(Mg_{0.80}Fe_{0.20})O$ at 300 MPa and temperatures between 1300 and 1400 K indicate textures compatible with slip on ½<110>{110} at low strain, with a change dominant ½<110>{100} and ½<110>{111} at intermediate strains and, finally, strong recrystallization at the highest strains [269]. Recrystallization aligns {112} with the shear plane and <110> with the shear direction, which was interpreted again as the action of dominant slip on ½<110>{100} and potentially ½<110>{111}.

Finally, the recent study of Immoor and coworkers [270] shows the compression textures of (Mg,Fe)O up to combined pressures and temperatures of 80 GPa and 1400 K. These experiments indicate a shift from a 001 to a combined (001 + 011) compression texture maximum as pressure and temperature increase. The texture transition, which could be assigned to a change from dominant {110} to dominant {100} slip is observed at ~1400 K at low pressure and for pressures above 50 GPa at ~1200 K.

5.2.2. Effect of P, T, and Fe on the Mechanical Properties of Polycrystalline MgO and $(Mg_x,Fe_{1-x})O$

The effect of hydrostatic pressure on MgO plasticity was first investigated up to 1 GPa and 750 °C [271,272]. These studies showed that: (i) under ambient temperature MgO becomes ductile between 100 and 200 MPa; (ii) that the ambient temperature strength beyond yielding increases with confining pressure; and (iii) that the pressure sensitivity of the stress–strain curve becomes less pronounced above 300 °C. In all cases, the plasticity of MgO was shown to be dominated by slip in ½<110>{110}.

WD EX1058
Western Digital v IP Bridge
Page 39

The effect of hydrostatic pressure on the polycrystalline rheological law was quantified by experiments up to 10 GPa at temperatures up to 1600 K in the D-DIA [255,263,273–277]. Most of these studies focused on establishing the stress–strain behavior and rheological laws for MgO. Under ambient temperature and a pressure of 8 GPa [274] the measured strength is 4 GPa, with a sharp decrease above 1200 K, and down to a strength of ~200 MPa at 1400 K (Figure 34b).

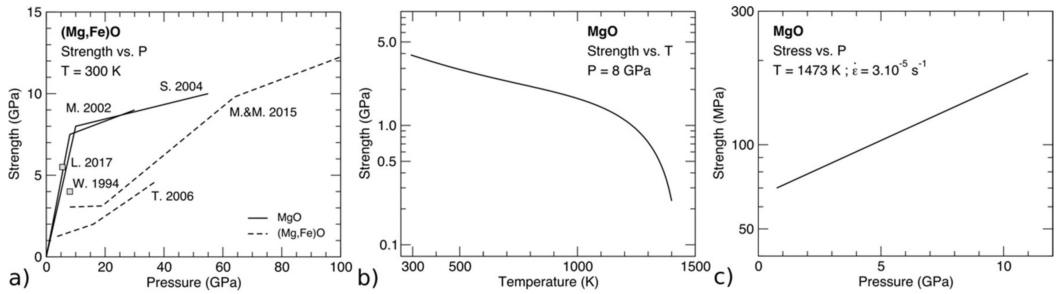

Figure 34. Effect of P, T, and Fe content on the strength of polycrystalline (Mg,Fe)O. (**a**) Ambient T strength of (Mg,Fe)O vs. P and Fe content. Solid lines are the diamond anvil cell experiments for pure MgO of Merkel and colleagues [252] and Singh and collaborators [278]. Squares are the multi-anvil press data for pure MgO of Weidner et al. [263] and Lin and collaborators [253]. Dashed lines are the diamond anvil data for Fe-bearing (Mg,Fe)O of Tommaseo et al. [265] and Marquardt and Miyagi [279]; (**b**) Strength of pure MgO vs. temperature measured at 8 GPa in the multi-anvil press by Weidner and collaborators [263]; (**c**) Flow stress of pure MgO vs. pressure at 1473 K and 3×10^{-5}/s from the multi-anvil press results of Mei and coworkers [273].

More recently, the creep behavior of MgO was investigated up to 10 GPa [273]. Based on their data and stresses evaluated on the 200 diffraction line (see discussion above), the flow strength of MgO at 1473 K and at a strain rate of 3×10^{-5}/s increases from 80 MPa at 2 GPa to 200 MPa at 10 GPa, indicating an activation volume $V^* = 2.4 \pm 0.9 \times 10^{-6}$ m^3/mol (Equation (16), Figure 34c). Other parameters for their rheological law are a stress exponent $n = 3$ and an activation energy $Q = 72 \pm 50$ kJ/mol. Do note, however, that the choice of the 200 diffraction line for stress evaluation is arbitrary and that stresses evaluated using the 111 reflection are about two times higher [273].

Under ambient pressure, pure MgO was studied multiple times up to pressure of 60 GPa [248,252,278,280,281]. From these studies, the strength of polycrystalline MgO was shown to increase from 1 to ca. 8 GPa as the pressure is raised from ambient to about 9 GPa. The increase in strength is much less pronounced at higher pressures, reaching 10 GPa at a pressure of 60 GPa (Figure 34a). Earlier works of [248] lead to lower values of MgO strength but this deduction of stress is probably based on improper assumptions regarding the sample stress state [282].

Interestingly, the addition of Fe into (Mg,Fe)O seems to change this behavior [265,267,279]. Between 40 and 80 GPa, Fe in (Mg,Fe)O undergoes electronic spin-pairing transition from a high-spin to a low-spin state [266]. This transition leads to a reduction of the unit-cell volume which can induce a reduction of the sample stress [267], although it is not always observed [279]. Measurements up to 100 GPa, however, seem to indicate that the strength of (Mg,Fe)O does not follow the same behavior than that of pure MgO (Figure 34a), with a slow increase of strength up 3 GPa at a pressure of 20 GPa, a sharp increase up to 10 GPa at 60 GPa, and a further increase up to 12 GPa at 100 GPa [279].

5.2.3. Experimental Identification of Individual Deformation Mechanisms

Comparisons between deformation textures in polycrystals and simulations such as VPSC are often used to infer dominant deformation mechanisms at the single-crystal scale. There are limitations, however, as: (i) deformation textures are not always sensitive to a change in dominant deformation mechanisms; (ii) the solution from modeling such as VPSC can be non-unique; (iii) textures cannot

be used to evaluate the absolute values of the slip system's CRSS; and (iv) polycrystal deformation includes effects of grain-to-grain interactions, microstructures, and hardening and, hence, can differ from that of a single crystal. The identification of dominant deformation mechanisms in MgO at high pressure can be further addressed using two methods: experiments on single-crystals, and more advanced comparison between experimental results on polycrystals and polycrystalline plasticity simulations.

Recent works in the D-DIA [262] focused on the effect of pressure on slip and dislocation in MgO single crystals with the aim of testing the pressure-induced dominant slip system inversion predicted by numerical models [261]. In these experiments, MgO single crystals are deformed in orientations chosen to activate either slip on {110} or {100}, at temperatures between 1273 K and 1473 rac12<110>{110}, the activation volume is $V^* = 1.0 \times 10^{-6}$ m^3/mol. For single crystals oriented to favor slip on ½<110>{100}, the activation volume is close to zero. This implies that, as pressure increases, the strength of slip on ½<110>{100} does not change while ½<110>{110} slip becomes harder. The predicted inversion of dominant slip system in MgO based on these measurements is at ~23 GPa.

Uncertainties remain, however, on the relative plastic behavior of single-crystal and polycrystalline MgO. Grain-grain interactions in polycrystals can fundamentally change their behavior. Moreover, dislocation interactions between the different slip systems may change the behavior relative to perfectly oriented single crystals. To address this issue, recent studies focused on the behavior of polycrystalline MgO at ambient temperature, at strain rates of ~3×10^{-5} s^{-1} and pressures up to 5.4 GPa [253]. In this case, the experimental data is fully compared to EVPSC models to match not only the measured textures but also the microscopic strains inferred from individual lattice planes. Such a procedure provides much stronger constrains on the active deformation mechanisms and their physical properties, i.e., CRSS and hardening. This study leads to a steady state CRSS of 1.2 and 3.2 GPa for ½<110>{110} and ½<110>{100}, respectively. However, their results are significantly larger than results of numerical models on single crystals [261] and demonstrate the importance of strain hardening or grain size effects in polycrystals.

As highlighted above, there are still many questions regarding the combined effects of pressure, temperature on the plasticity of MgO. At present, works are under way to extend the measurements into several directions: (i) larger P, T, and composition ranges [245,270]; (ii) finer interpretation of the experimental data with polycrystal plasticity models [253]; and (iii) complex deformation history, such as sinusoidal oscillations [283]. These works will allow, in the future, clarifying the combined effects of P and T on MgO and (Mg,Fe)O plasticity.

6. Conclusions and Prospects

This review paper focused on dislocations and plastic deformation in MgO crystals and here is an overview of the key-points covered:

- Standard compression tests helped to describe dislocation-based plasticity processes in MgO in the 1950s. Plasticity is controlled by screw dislocations gliding in soft ½<110>{110} and hard ½<110>{100} slip systems and MgO is referred as a material with high lattice friction.
- Atomistic simulations based on dislocation core calculation confirmed the key role of screw dislocation for MgO plasticity. Multi-scale modeling approaches allow describing MgO plasticity on a wide range of temperatures and pressures, up to the polycrystal.
- The development of existing and novel experimental techniques since the 1990s, especially with the development of tests at the micro- and nano-scales, allows investigating elementary deformation processes providing a better description of dislocation mechanisms.
- Experiments and modeling show that MgO is sensitive to pressure increases. Dislocation cores and elementary deformation processes evolve under pressure inducing a softening of the ½<110>{100} mode when compared to ½<110>{110}. This change has significant consequences on macroscopic mechanical properties such as polycrystalline textures.

The general understanding of MgO plasticity from both experimental tests at different scales and multi-scale modeling opens new avenues to describe its behavior under stress and, in particular, in the case of high hydrostatic pressure. While this is of particular importance for the prediction of deep-Earth rheology, this may impact our view of ceramic plasticity, since it can occur for particular loading conditions and/or small sample sizes in inorganic materials. This is now no longer restricted to MgO, and plasticity of other inorganic materials (e.g., Alumina) in the form of nanoparticles was shown to be possible. New paradigms in the process of ceramics can then be forecast as it is the case of isostatic compression and shaping of ceramic green bodies at low or moderate temperature or the use of external electric field to accelerate dislocation motion and thus improve plasticity. Playing with the plasticity of inorganic crystals may thus to a certain extent open the door towards "plastic ceramics".

Author Contributions: J.A. designed the project. J.A. and J.C. were in charge of the macro-testing section. P.C. (Philippe Carrez), P.C. (Patrick Cordier) and J.A. designed the multi-scale modeling section. C.T. and S.K. were in charge of the micro- and nano-mechanics section. S.M. designed the high-pressure section with J.A. All authors discussed the study and wrote the article.

Funding: Patrick Cordier and Philippe Carrez are supported by funding from the European Research Council under the Seventh Framework Programme (FP7), ERC Grant No. 290424–RheoMan.

Conflicts of Interest: The authors declare no conflict of interest.

References

1. Johnston, W.G.; Gilman, J.J. Dislocation Velocities, Dislocation Densities, and Plastic Flow in Lithium Fluoride Crystals. *J. Appl. Phys.* **1959**, *30*, 1–16. [CrossRef]
2. Stokes, R.J. *Microstructure and Mechanical Properties of Ceramics*; Accession Number: AD0407614; Defense Technical Information Center: Fort Belvoir, VA, USA, 1963.
3. Haasen, P.; Barthel, C.; Suzuki, T. Choice of slip system and Peierls stresses in the NaCl structure. In *Dislocations in solids*; Suzuki, H., Ninomiya, T., Sumino, K., Takeuchi, S., Eds.; University of Tokyo Press: Tokyo, Japan, 1985; pp. 455–462.
4. Takeuchi, S.; Koizumi, H.; Suzuki, T. Peierls stress and kink pair energy in NaCl type crystals. *Mater. Sci. Eng. A* **2009**, *521*, 90–93. [CrossRef]
5. Hulse, C.; Copley, S.; Pask, J. Effect of crystal orientation on plastic deformation of magnesium oxide. *J. Am. Ceram. Soc.* **1963**, *46*, 317–323. [CrossRef]
6. Groves, G.W.; Kelly, A. Independent slip systems in crystals. *Philos. Mag. A* **1963**, *8*, 877–887. [CrossRef]
7. Day, R.; Stokes, R. Mechanical behavior of Magnesium Oxide at high temperatures. *J. Am. Ceram. Soc.* **1964**, *47*, 493–503. [CrossRef]
8. Copley, S.; Pask, J. Plastic deformation of MgO single crystals up to 1600 C. *J. Am. Ceram. Soc.* **1965**, *48*, 139–146. [CrossRef]
9. Washburn, J.; Groves, G.; Kelly, A.; Williamson, G. Electron microscope observations of deformed magnesium oxide. *Philos. Mag. A* **1960**, *5*, 991–999. [CrossRef]
10. Clauer, A.; Wilcox, B. High temperature tensile creep of magnesium oxide single crystals. *J. Am. Ceram. Soc.* **1976**, *59*, 89–96. [CrossRef]
11. Mariani, E.; Mecklenburgh, J.; Wheeler, J.; Prior, D.J.; Heidelbach, F. Microstructure evolution and recrystallization during creep of MgO single crystals. *Acta Mater.* **2009**, *57*, 1886–1898. [CrossRef]
12. Messerschmidt, U.; Appel, F. Dislocation motion and formation of dislocation structures during in situ deformation in a high voltage electron microscope. *Mater. Sci. Eng. A* **1989**, *113*, 409–414. [CrossRef]
13. Tromas, C.; Girard, J.; Woirgard, J. Study by atomic force microscopy of elementary deformation mechanisms involved in low load indentations in MgO crystals. *Phil. Mag. A* **2000**, *80*, 2325–2335. [CrossRef]
14. Hulse, C.; Pask, J. Mechanical Properties of Magnesia Single Crystals Compression. *J. Am. Ceram. Soc.* **1960**, *43*, 373–378. [CrossRef]
15. Appel, F.; Wielke, B. Low temperature deformation of impure MgO single crystals. *Mater. Sci. Eng.* **1985**, *73*, 97–103. [CrossRef]
16. Singh, R.; Coble, R. Dynamic dislocation behavior in "pure" magnesium oxide single crystals. *J. Appl. Phys.* **1974**, *45*, 981–989. [CrossRef]

17. Woo, C.H.; Puls, M.P. The Peierls mechanism in MgO. *Phil. Mag. A J. Theor. Expe. Appl. Phys.* **1977**, *35*, 1641–1652. [CrossRef]
18. May, J.; Kronberg, M. Temperature Dependence of Plastic Yield Stress of Single Crystals of Magnesium Oxide. *J. Am. Ceram. Soc.* **1960**, *43*, 525–530. [CrossRef]
19. Sinha, M.; Lloyd, D.; Tangri, K. Dislocation dynamics and thermally-activated deformation of MgO single crystals. *Philos. Mag. A* **1973**, *28*, 1341–1352. [CrossRef]
20. Srinivasan, M.; Stoebe, T. Temperature dependence of yielding and work-hardening rates in magnesium oxide single crystals. *J. Mat. Sci.* **1974**, *9*, 121–128. [CrossRef]
21. Sato, F.; Sumino, K. The yield strength and dynamic behaviour of dislocations in MgO crystals at high temperatures. *J. Mat. Sci.* **1980**, *15*, 1625–1634. [CrossRef]
22. Barthel, C. Plastiche Anisotropie von Bleisulfid und Magnesiumoxid. Diploma Thesis, University of Gottingen, Göttingen, Germany, 1984.
23. Amodeo, J.; Carrez, P.; Devincre, B.; Cordier, P. Multiscale modelling of MgO plasticity. *Acta Mater.* **2011**, *59*, 2291–2301. [CrossRef]
24. Appel, F.; Bethge, H.; Messerschmidt, U. Dislocation motion and multiplication at the deformation of MgO single crystals in the high voltage electron microscope. *Phys. Status Solidi A* **1977**, *42*, 61–71. [CrossRef]
25. Foitzik, A.; Skrotzki, W.; Haasen, P. Correlation between microstructure, dislocation dissociation and plastic anisotropy in ionic crystals. *Mater. Sci. Eng. A* **1989**, *113*, 399–407. [CrossRef]
26. Messerschmidt, U. *Dislocation Dynamics during Plastic Deformation*; Springer Series in Materials Science: New York, NY, USA, 2010; Volume 129, pp. 1–509.
27. Singh, R.; Coble, R. Dynamic dislocation behavior in iron-doped magnesium oxide crystals. *J. Appl. Phys.* **1974**, *45*, 990–995. [CrossRef]
28. Dorn, J.; Rajnak, S. Nucleation of kink pairs and the Peierls mechanism of plastic deformation. *Trans. Metall. Soc. AIME* **1964**, *230*, 1052–1064.
29. Guyot, P.; Dorn, J. A critical review of the Peierls mechanism. *Can. J. Phys.* **1967**, *45*, 983–1016. [CrossRef]
30. Boudet, A.; Kubin, L.P. Exhaustion mechanisms in the Preyield domain of niobium single crystals at low temperatures. *J. Phys.* **1975**, *36*, 823–833. [CrossRef]
31. Groves, G.; Fine, M. Solid Solution and Precipitation Hardening in Mg-Fe-O Alloys. *J. Appl. Phys.* **1964**, *35*, 3587–3593. [CrossRef]
32. Srinivasan, M.; Stoebe, T. Effect of Impurities on the Mechanical Behavior of MgO Single Crystals. *J. Appl. Phys.* **1970**, *41*, 3726–3730. [CrossRef]
33. Gorum, A.; Luhman, W.; Pask, J. Effect of Impurities and Heat-Treatment on Ductility of MgO. *J. Am. Ceram. Soc.* **1960**, *43*, 241–245. [CrossRef]
34. Davidge, R. The distribution of iron impurity in single-crystal magnesium oxide and some effects on mechanical properties. *J. Mater. Sci.* **1967**, *2*, 339–346. [CrossRef]
35. Messerschmidt, U.; Appel, F. Characterization of precipitation hardening mechanisms by investigating dislocation dynamics in the HVEM. *Czechoslov. J. Phys.* **1985**, *35*, 217–220. [CrossRef]
36. Appel, F.; Messerschmidt, U. Dislocation Processes in MgO Single Crystals Observed by In-situ Deformation in the HVEM. *Krist. Tech.* **1979**, *14*, 1329. [CrossRef]
37. Messerschmidt, U. Line tension model of the interaction between dislocations and extended obstacles to glide. *Mater. Sci. Eng. A* **1988**, *100*, 101–108. [CrossRef]
38. Messerschmidt, U.; Appel, F.; Schmid, H. The radius of curvature of dislocation segments in MgO crystals stressed in the high-voltage electron microscope. *Philos. Mag.* **1985**, *51*, 781–796. [CrossRef]
39. Kardashev, B.K.; Kustov, S.B.; Lebedev, A.B.; Berezhkova, G.V.; Perstnev, P.P.; Appel, F.; Messerschmidt, U. Acoustic and Electron Microscopy Study of the Dislocation Structure in MgO Crystals. *Phys. Status Solidi A* **1985**, *91*, 79–87. [CrossRef]
40. Appel, F.; Bartsch, M.; Messerschmidt, U.; Nadgornyi, E.; Valkovskii, S. Dislocation motion and plasticity in MgO single crystals. *Phys. Status Solidi A* **1984**, *83*, 179–194. [CrossRef]
41. Appel, F.; Berezhkova, G.V.; Messerschmidt, U.; Perstnev, P.P.; Rozhanskii, V.N. HVEM In-Situ Straining Experiments on MgO Specimens Predeformed at High Temperature. *Cryst. Res. Technol.* **1981**, *16*, 1309–1314. [CrossRef]

42. Appel, F.; Messerschmidt, U.; Nadgornyi, E.M.; Zaitsev, S.I. The interaction between dislocations and point obstacles: A comparison of the interaction parameter distributions obtained from computer simulation and from In situ high voltage electron microscopy straining experiments. *Mater. Sci. Eng.* **1982**, *52*, 69–74. [CrossRef]
43. Appel, F.; Bethge, H.; Messerschmidt, U. Distribution of point-obstacle distance during the motion of screw dislocations in MgO single crystals. *Phys. Status Solidi A* **1976**, *38*, 103–108. [CrossRef]
44. Routbort, J.L. Work-Hardening and Creep of MgO. *Acta Metall.* **1979**, *27*, 649–661. [CrossRef]
45. Amodeo, J.; Devincre, B.; Carrez, P.; Cordier, P. Dislocation reactions, plastic anisotropy and forest strengthening in MgO at high temperature. *Mech. Mater.* **2014**, *71*, 62–73. [CrossRef]
46. Kear, B.; Taylor, A.; Pratt, P. Some dislocation interactions in simple ionic crystals. *Philos. Mag. A* **1959**, *4*, 665–680. [CrossRef]
47. Ruano, O.A.; Wolfenstine, J.; Wadsworth, J.; Sherby, O.D. Harper-Dorn and power law creep in uranium dioxide. *Acta Metallurgica et Materialia* **1991**, *39*, 661–668. [CrossRef]
48. Cummerow, R. High-Temperature Steady-State Creep Rate in Single-Crystal MgO. *J. Appl. Phys.* **1963**, *34*, 1724–1729. [CrossRef]
49. Rothwell, W.S.; Neiman, A.S. Creep in Vacuum of MgO Single Crystals and the Electric Field Effect. *J. Appl. Phys.* **1965**, *36*, 2309–2316. [CrossRef]
50. Hüther, W.; Reppich, B. Dislocation structure during creep of MgO single crystals. *Philos. Mag. A* **1973**, *28*, 363–371. [CrossRef]
51. Ramesh, K.S.; Yasuda, E.; Kimura, S.; Urabe, K. High-temperature creep and dislocation structure of MgO single crystals at low stresses. *J. Mater. Sci.* **1986**, *21*, 4015–4018. [CrossRef]
52. Ramesh, K.S.; Yasuda, E.; Kimura, S. Negative creep and recovery during high-temperature creep of MgO single crystals at low stresses. *J. Mater. Sci.* **1986**, *21*, 3147–3152. [CrossRef]
53. Hensler, J.H.; Cullen, G.V. Stress, Temperature, and Strain Rate in Creep of Magnesium Oxide. *J. Am. Ceram. Soc.* **1968**, *51*, 557–559. [CrossRef]
54. Langdon, T.G.; Pask, J.A. The mechanism of creep in polycrystalline magnesium oxide. *Acta Metall.* **1970**, *18*, 505–510. [CrossRef]
55. Bilde-Sörensen, J.B. Dislocation Structures in Creep-Deformed Polycrystalline MgO. *J. Am. Ceram. Soc.* **1972**, *55*, 606–610. [CrossRef]
56. Wolfenstine, J.; Kohlstedt, D.L. Creep of (Mg, Fe)O single crystals. *J. Mater. Sci.* **1988**, *23*, 3550–3557. [CrossRef]
57. Stretton, I.; Heidelbach, F.; Mackwell, S.; Langenhorst, F. Dislocation creep of magnesiowüstite ($Mg_{0.8}Fe_{0.2}$). *Earth Planet. Sci. Lett.* **2001**, *194*, 229–240. [CrossRef]
58. Weertman, J. Steady-state creep through dislocation climb. *J. Appl. Phys.* **1957**, *28*, 362–364. [CrossRef]
59. Poirier, J.P. On the symmetrical role of cross-slip of screw dislocations and climb of edge dislocations as recovery processes controlling high-temperature creep. *Revue de Physique Appliquée* **1976**, *11*, 731–738. [CrossRef]
60. Lewis, G.V.; Catlow, C.R.A. Potential models for ionic oxides. *J. Phys. C Solid State Phys.* **1985**, *18*, 1149–1161. [CrossRef]
61. Sangster, M.J.L. Interionic potentials and force constant models for rocksalt structure crystals—II. *J. Phys. Chem. Solids* **1974**, *35*, 195–200. [CrossRef]
62. Woodward, C. First-principles simulations of dislocation cores. *Mat. Sci. Eng. A* **2005**, *400–401*, 59–67. [CrossRef]
63. Woo, C.H.; Puls, M.P. An improved method of calculating the lattice friction stress using an atomistic model. *J. Phys. C Solid State Phys.* **1976**, *9*, L27. [CrossRef]
64. Puls, M.; Norgett, M. Atomistic calculation of the core structure and Peierls energy of an (a/2)[110] edge dislocation in MgO. *J. Appl. Phys.* **1976**, *47*, 466–477. [CrossRef]
65. Woo, C.H.; Puls, M.P. Atomistic breathing shell model calculations of dislocation core configurations in ionic crystals. *Philos. Mag. A* **1977**, *35*, 727–756. [CrossRef]
66. Watson, G.W.; Kelsey, E.T.; de Leeuw, N.H.; Harris, D.J.; Parker, S.C. Atomistic simulation of dislocations, surfaces and interfaces in MgO. *Faraday Trans.* **1996**, *92*, 433–438. [CrossRef]
67. Lehto, N.; Öberg, S. Effects of Dislocation Interactions: Application to the Period-Doubled Core of the 90° Partial in Silicon. *Phys. Rev. Lett.* **1998**, *80*, 5568–5571. [CrossRef]

68. Carrez, P.; Godet, J.; Cordier, P. Atomistic simulations of ½<110> screw dislocation core in magnesium oxide. *Comput. Mater. Sci.* **2015**, *103*, 250–255. [CrossRef]
69. Christian, J.W.; Vítek, V. Dislocations and stacking faults. *Rep. Prog. Phys.* **1970**, *33*, 307–411. [CrossRef]
70. Peierls, R. The size of a dislocation. *Proc. Phys. Soc.* **1940**, *52*, 34–37. [CrossRef]
71. Nabarro, F. Dislocations in a simple cubic lattice. *Proc. Phys. Soc.* **1947**, *59*, 256–272. [CrossRef]
72. Vítek, V. Intrinsic stacking faults in body-centred cubic crystals. *Philos. Mag. A* **1968**, *18*, 773–786. [CrossRef]
73. Miranda, C.; Scandolo, S. Computational materials science meets geophysics: Dislocations and slip planes of MgO. *Comput. Phys. Commun.* **2005**, *169*, 24–27. [CrossRef]
74. Carrez, P.; Ferré, D.; Cordier, P. Peierls-Nabarro modelling of dislocations in MgO from ambient pressure to 100 GPa. *Model. Sim. Mater. Sci. Eng.* **2009**, *17*, 035010. [CrossRef]
75. Schoeck, G. The Peierls model: Progress and limitations. *Mater. Sci. Eng. A* **2005**, *400*, 7–17. [CrossRef]
76. Denoual, C. Dynamic dislocation modeling by combining Peierls Nabarro and Galerkin methods. *Phys. Rev. B* **2004**, *70*, 024106. [CrossRef]
77. Lu, G. The Peierls–Nabarro model of dislocations: a venerable theory and its current development. In *Handbook of Materials Modeling*; Springer: Dordrecht, The Netherlands, 2005; pp. 773–792.
78. Joos, B.; Ren, Q.; Duesbery, M.S. Peierls-Nabarro model of dislocations in silicon with generalized stacking-fault restoring forces. *Phys. Rev. B* **1994**, *50*, 5890–5898. [CrossRef]
79. Hirth, J.P.; Lothe, J. *Theory of Dislocations*; John Willey and Sons: Hoboken, NJ, USA, 1982.
80. Caillard, D.; Martin, J.L. *Thermally Activated Mechanisms in Crystal Plasticity*; Elsevier: New York, NY, USA, 2003.
81. Kamimura, Y.; Edagawa, K.; Takeuchi, S. Experimental evaluation of the Peierls stresses in a variety of crystals and their relation to the crystal structure. *Acta Mater.* **2013**, *61*, 294–309. [CrossRef]
82. Vitek, V.; Yamaguchi, M. Core structure of nonscrew 1/2 (111) dislocations on (110) planes in bcc crystals. II. Peierls stress and the effect of an external shear stress on the cores. *J. Phys. F Metal Phys.* **1973**, *3*, 537. [CrossRef]
83. Duesbery, M.; Vitek, V. Plastic anisotropy in bcc transition metals. *Acta Mater.* **1998**, *46*, 1481–1492. [CrossRef]
84. Xu, W.; Moriarty, J.A. Accurate atomistic simulations of the Peierls barrier and kink-pair formation energy for ⟨111⟩ screw dislocations in bcc Mo. *Comput. Mater. Sci.* **1998**, *9*, 348–356. [CrossRef]
85. Woodward, C.; Rao, S.I. Flexible Ab Initio Boundary Conditions: Simulating Isolated Dislocations in bcc Mo and Ta. *Phys. Rev. Lett.* **2002**, *88*, 216402. [CrossRef] [PubMed]
86. Wang, G.; Strachan, A.; Çağın, T.; Goddard, W.A. Atomistic simulations of kinks in 1/2a⟨111⟩screw dislocations in bcc tantalum. *Phys. Rev. B Condens. Matter* **2003**, *68*, 558. [CrossRef]
87. Gröger, R.; Bailey, A.; Vitek, V. Multiscale modeling of plastic deformation of molybdenum and tungsten: I. Atomistic studies of the core structure and glide of 1/2<111> screw dislocations at 0 K. *Acta Mater.* **2008**, *56*, 5401–5411. [CrossRef]
88. Rodney, D.; Proville, L. Stress-dependent Peierls potential: Influence on kink-pair activation. *Phys. Rev. B* **2009**, *79*, 1–9. [CrossRef]
89. Proville, L.; Ventelon, L.; Rodney, D. Prediction of the kink-pair formation enthalpy on screw dislocations in α-iron by a line tension model parametrized on empirical potentials and first-principles calculations. *Phys. Rev. B* **2013**, *87*, 244–248. [CrossRef]
90. Edagawa, K.; Koizumi, H.; Kamimura, Y.; Suzuki, T. Temperature dependence of the flow stress of III–V compounds. *Philos. Mag. A* **2000**, *80*, 2591–2608. [CrossRef]
91. Pizzagalli, L.; Pedersen, A.; Arnaldsson, A.; Jonsson, H.; Beauchamp, P. Theoretical study of kinks on screw dislocation in silicon. *Phys. Rev. B* **2008**, *77*, 064106. [CrossRef]
92. Pedersen, A.; Pizzagalli, L.; Jónsson, H. Finding mechanism of transitions in complex systems: Formation and migration of dislocation kinks in a silicon crystal. *J. Phys. Condens. Matter* **2009**, *21*, 084210. [CrossRef] [PubMed]
93. Mitchell, T.E.; Anderson, P.M.; Baskes, M.I.; Chen, S.P.; Hoagland, R.G.; Misra, A. Nucleation of kink pairs on partial dislocations: A new model for solution hardening and softening. *Philos. Mag. A* **2003**, *83*, 1329–1346. [CrossRef]
94. Carrez, P.; Ferré, D.; Denoual, C.; Cordier, P. Modelling thermal activation of <110>{110} slip at low temperature in SrTiO3. *Scr. Mater.* **2010**, *63*, 434–437. [CrossRef]
95. Castillo-Rodríguez, M.; Sigle, W. The kink-pair mechanism and low-temperature flow-stress behaviour of strontium titanate single crystals. *Scr. Mater.* **2011**, *64*, 241–244. [CrossRef]

96. Celli, V.; Kabler, M.; Ninomiya, T.; Thomson, R. Theory of Dislocation Mobility in Semiconductors. *Phys. Rev.* **1963**, *131*, 58–72. [CrossRef]
97. Seeger, A.; Schiller, P. Bildung und diffusion von kinken als grundprozess der versetzungsbewegung bei der messung der inneren reibung. *Acta Metall.* **1962**, *10*, 348–357. [CrossRef]
98. Koizumi, H.; Kirchner, H.; Suzuki, T. Kink pair nucleation and critical shear stress. *Acta Metallurgica et Materialia* **1993**, *41*, 3483–3493. [CrossRef]
99. Koizumi, H.; Kirchner, H.O.K.; Suzuki, T. Nucleation of trapezoidal kink pairs on a Peierls potential. *Philos. Mag. A* **1994**, *69*, 805–820. [CrossRef]
100. Southgate, P.D.; Mendelson, K.S. Kilocycle-Range Dislocation Damping in Magnesium Oxide. *J. Appl. Phys.* **1966**, *37*, 206–215. [CrossRef]
101. Joos, B.; Zhou, J. The Peierls-Nabarro model and the mobility of the dislocation line. *Philos. Mag. A* **2001**, *81*, 1329–1340. [CrossRef]
102. Ventelon, L.; Willaime, F.; Leyronnas, P. Atomistic simulation of single kinks of screw dislocations in α-Fe. *J. Nucl. Mater.* **2009**, *386–388*, 26–29. [CrossRef]
103. Proville, L.; Rodney, D.; Marinica, M.-C. Quantum effect on thermally activated glide of dislocations. *Nat. Mater.* **2012**, *11*, 845–849. [CrossRef] [PubMed]
104. Fitzgerald, S.P. Kink pair production and dislocation motion. *Sci. Rep.* **2016**, *6*, 1–7. [CrossRef] [PubMed]
105. Nabarro, F. One-dimensional models of thermal activation under shear stress. *Philos. Mag. A* **2003**, *83*, 3047–3054. [CrossRef]
106. Devincre, B.; Madec, R.; Monnet, G.; Queyreau, S.; Gatti, R.; Kubin, L. Modeling crystal plasticity with dislocation dynamics simulations: The "microMegas" code. In *Mechanics of Nano-Objects*; Presse des Mines: Paris, France, 2011; pp. 81–100.
107. Arsenlis, A.; Cai, W.; Tang, M.; Rhee, M.; Oppelstrup, T.; Hommes, G.; Pierce, T.; Bulatov, V. Enabling strain hardening simulations with dislocation dynamics. *Model. Sim. Mater. Sci. Eng.* **2007**, *15*, 553–595. [CrossRef]
108. Chang, H.-J.; Fivel, M.; Rodney, D.; Verdier, M. Multiscale modelling of indentation in FCC metals: From atomic to continuum. *Comptes Rendus Physique* **2010**, *11*, 285–292. [CrossRef]
109. Queyreau, S.; Monnet, G.; Devincre, B. Orowan strengthening and forest hardening superposition examined by dislocation dynamics simulations. *Acta Mater.* **2010**, *58*, 5586–5595. [CrossRef]
110. Mohles, V. Simulations of dislocation glide in overaged precipitation-hardened crystals. *Philos. Mag. A* **2001**, *81*, 971–990. [CrossRef]
111. Monnet, G. Investigation of precipitation hardening by dislocation dynamics simulations. *Philos. Mag. A* **2006**, *86*, 5927–5941. [CrossRef]
112. Shin, C.; Fivel, M.; Verdier, M.; Robertson, C. Dislocation dynamics simulations of fatigue of precipitation-hardened materials. *Mater. Sci. Eng. A* **2005**, *400*, 166–169. [CrossRef]
113. Chang, H.-J.; Segurado, J.; Molina-Aldareguía, J.M.; Soler, R.; LLorca, J. A 3D dislocation dynamics analysis of the size effect on the strength of [1 1 1] LiF micropillars at 300K and 600K. *Model. Sim. Mater. Sci. Eng.* **2016**, *24*, 035009. [CrossRef]
114. Cui, Y.; Po, G.; Ghoniem, N. Controlling Strain Bursts and Avalanches at the Nano- to Micrometer Scale. *Phys. Rev. Lett.* **2016**, *117*, 155502. [CrossRef] [PubMed]
115. El-Awady, J.; Woodward, C.; Dimiduk, D.; Ghoniem, N. Effects of focused ion beam induced damage on the plasticity of micropillars. *Phys. Rev. B* **2009**, *80*, 104104. [CrossRef]
116. Amodeo, R.J.; Ghoniem, N.M. Dislocation Dynamics. 1. A Proposed Methodology for Deformation Micromechanics. *Phys. Rev. B Condens. Matter* **1990**, *41*, 6958–6967. [CrossRef] [PubMed]
117. Amodeo, R.J.; Ghoniem, N.M. Dislocation Dynamics. 2. Applications to the Formation of Persistent Slip Bands, Planar Arrays and Dislocation Cells. *Phys. Rev. B Condens. Matter* **1990**, *41*, 6968–6976. [CrossRef] [PubMed]
118. Van der Giessen, E.; Needleman, A. Discrete dislocation plasticity: a simple planar model. *Model. Sim. Mater. Sci. Eng.* **1995**, *3*, 689–735. [CrossRef]
119. Keralavarma, S.M.; Curtin, W.A. Strain hardening in 2D discrete dislocation dynamics simulations—A new "2.5D" algorithm. *J. Mech. Phys. Solids* **2016**, *95*, 132–146. [CrossRef]
120. Wickham, L.; Schwarz, K.; Stölken, J. Rules for forest interactions between dislocations. *Phys. Rev. Lett.* **1999**, *83*, 4574–4577. [CrossRef]

121. Madec, R.; Kubin, L.P. Dislocations interactions and symmetries in BCC crystals. In *IUTAM Symposium on Mesoscopic Dynamics of Fracture Process and Materials Strength*; Springer: Dordrecht, The Netherlands, 2004; pp. 69–79.
122. Madec, R.; Devincre, B.; Kubin, L.P. On the nature of attractive dislocation crossed states. *Comput. Mater. Sci.* **2002**, *23*, 219–224. [CrossRef]
123. Monnet, G.; Devincre, B.; Kubin, L.P. Dislocation study of prismatic slip systems and their interactions in hexagonal close packed metals: application to zirconium. *Acta Mater.* **2004**, *52*, 4317–4328. [CrossRef]
124. Capolungo, L. Dislocation junction formation and strength in magnesium. *Acta Mater.* **2011**, *59*, 2909–2917. [CrossRef]
125. Devincre, B. Dislocation dynamics simulations of slip systems interactions and forest strengthening in ice single crystal. *Philos. Mag. A* **2012**, *93*, 235–246. [CrossRef]
126. Durinck, J.; Devincre, B.; Kubin, L.P.; Cordier, P. Modeling the plastic deformation of olivine by dislocation dynamics simulations. *Am. Mineral.* **2007**, *92*, 1346–1357. [CrossRef]
127. Carrez, P.; Cordier, P.; Devincre, B.; Kubin, L.P. Dislocation reactions and junctions in MgO. *Mater. Sci. Eng. A* **2005**, *400*, 325–328. [CrossRef]
128. Devincre, B.; Hoc, T.; Kubin, L.P. Collinear interactions of dislocations and slip systems. *Mater. Sci. Eng. A* **2005**, *400*, 182–185. [CrossRef]
129. Madec, R.; Devincre, B.; Kubin, L.P.; Hoc, T.; Rodney, D. The role of collinear interaction in dislocation-induced hardening. *Science* **2003**, *301*, 1879–1882. [CrossRef] [PubMed]
130. Cordier, P.; Amodeo, J.; Carrez, P. Modelling the rheology of MgO under Earth's mantle pressure, temperature and strain rates. *Nature* **2012**, *481*, 177–180. [CrossRef] [PubMed]
131. Boioli, F.; Carrez, P.; Cordier, P.; Devincre, B.; Marquille, M. Modeling the creep properties of olivine by 2.5-dimensional dislocation dynamics simulations. *Phys. Rev. B* **2015**, *92*, 014115-1–014115-12. [CrossRef]
132. Reali, R.; Boioli, F.; Gouriet, K.; Carrez, P.; Devincre, B.; Cordier, P. Modeling plasticity of MgO by 2.5D dislocation dynamics simulations. *Mat. Sci. Eng. A* **2017**, *690*, 52–61. [CrossRef]
133. Soler, R.; Wheeler, J.M.; Chang, H.-J.; Segurado, J.; Michler, J.; LLorca, J.; Molina-Aldareguía, J.M. Understanding size effects on the strength of single crystals through high-temperature micropillar compression. *Acta Mater.* **2014**, *81*, 50–57. [CrossRef]
134. Keralavarma, S.M.; Benzerga, A.A. High-temperature discrete dislocation plasticity. *J. Mech. Phys. Solids* **2015**, *82*, 1–22. [CrossRef]
135. Yoo, H. Oxygen self-diffusion in single-crystal MgO: Secondary-ion mass spectrometric analysis with comparison of results from gas–solid and solid–solid exchange. *Solid State Ion.* **2002**, *150*, 207–221. [CrossRef]
136. Fischer-Cripps, A.C. *Nanoindentation*; Mechanical Engineering Series; Springer: New York, NY, USA, 2004.
137. Oliver, W.C.; Pharr, G.M. An improved technique for determining hardness and elastic modulus using load and displacement sensing indentation experiments. *J. Mater. Res.* **1992**, *7*, 1564–1583. [CrossRef]
138. Tromas, C.; Stinville, J.C.; Templier, C.; Villechaise, P. Hardness and elastic modulus gradients in plasma nitrided 316l polycrystalline stainless steel investigated by nanoindentation tomography. *Acta Mater.* **2012**, *60*, 1965–1973. [CrossRef]
139. Woirgard, J.; Tromas, C.; Girard, J.C.; Audurier, V. Study of the mechanical properties of ceramic materials by the nanoindentation technique. *J. Eur. Ceram. Soc.* **1998**, *18*, 2297–2305. [CrossRef]
140. Gilman, J.J.; Johnston, W.G. Dislocations in lithium fluoride crystals. *Solid State Phys.* **1961**, *13*, 147–222.
141. Stokes, R.J.; Johnston, T.L.; Li, C.H. Effect of surface condition on the initiation of plastic flow in MgO. *Trans. AIME* **1959**, *215*, 437.
142. Keh, A.S. Dislocations in indented magnesium oxide crystals. *J. Appl. Phys.* **1960**, *31*, 1538–1545. [CrossRef]
143. Newey, C.; Davidge, R.W. *Dislocations in Lithium Fluoride*; Metallurgical Services: Betchworth, UK, 1965.
144. Velednitskaya, M.A.; Rozhanskii, V.N.; Comolova, L.F.; Saparin, G.V.; Schreiber, J.; Brümmer, O. Investigation of the deformation mechanism of MgO crystals affected by concentrated load. *Phys. Status Solidi A* **1975**, *32*, 123–132. [CrossRef]
145. Armstrong, R.W.; Wu, C.C. Lattice Misorientation and Displaced Volume for Microhardness Indentations in MgO Crystals. *J. Am. Ceram. Soc.* **1978**, *61*, 102–106. [CrossRef]
146. Chaudhri, M.M. The displacement of material and the formation of {1l0}90, cracks around spherical indentations in MgO crystals. *Philos. Mag. A* **1986**, *53*, L55–L63. [CrossRef]

147. Keh, A.S. Cracks due to the piling-up of dislocations on two intersecting slip planes in MgO crystals. *Acta Metall.* **1959**, *7*, 694–696. [CrossRef]
148. Hammond, B.L.; Armstrong, R.W. Recovered elastic and plastic strains at residual micro-indentations in an MgO crystal. *Philos. Mag. Lett.* **1988**, *57*, 41–47. [CrossRef]
149. Gaillard, Y. Initiation de la Plasticité sous Nanoindentation dans MgO et LiF: Etude de L'organisation des Dislocations et des Contraintes Associées. PhD Thesis, Université de Poitiers, Poitiers, France, 2004.
150. Tromas, C.; Girard, J.; Audurier, V.; Woirgard, J. Study of the low stress plasticity in single-crystal MgO by nanoindentation and atomic force microscopy. *J. Mater. Sci.* **1999**, *34*, 5337–5342. [CrossRef]
151. Egberts, P.; Bennewitz, R. Atomic-scale nanoindentation: detection and identification of single glide events in three dimensions by force microscopy. *Nanotechnology* **2011**, *22*, 425703. [CrossRef] [PubMed]
152. Filleter, T.; Maier, S.; Bennewitz, R. Atomic-scale yield and dislocation nucleation in KBr. *Phys. Rev. B Condens. Matter Mater. Phys.* **2006**, *73*, 155433. [CrossRef]
153. Tromas, C.; Gaillard, Y.; Woirgard, J. Nucleation of dislocations during nanoindentation in MgO. *Philos. Mag. A* **2006**, *86*, 5595–5606. [CrossRef]
154. Gaillard, Y.; Tromas, C.; Woirgard, J. Study of the dislocation structure involved in a nanoindentation test by atomic force microscopy and controlled chemical etching. *Acta Mater.* **2003**, *51*, 1059–1065. [CrossRef]
155. Gilman, J.J.; Johnston, W.G.; Sears, G.W. Dislocation etch pit formation in lithium fluoride. *J. Appl. Phys.* **1958**, *29*, 747–754. [CrossRef]
156. Shaw, M.; Brookes, C. Dislocations produced in magnesium oxide crystals due to contact pressures developed by softer cones. *J. Mater. Sci.* **1989**, *24*, 2727–2734. [CrossRef]
157. Nix, W.D.; Gao, H. Indentation size effects in crystalline materials: A law for strain gradient plasticity. *J. Mech. Phys. Solids* **1998**, *46*, 411–425. [CrossRef]
158. Feng, G.; Nix, W.D. Indentation size effect in MgO. *Scr. Mater.* **2004**, *51*, 599–603. [CrossRef]
159. Huang, Y.; Zhang, F.; Hwang, K.C.; Nix, W.D.; Pharr, G.M.; Feng, G. A model for size effect in nano-indentation. *J. Mech. Phys. Sol.* **2006**, *54*, 1668–1986.
160. Sadrabadi, P.; Durst, K.; Göken, M. Study on the indentation size effect in CaF2: Dislocation structure and hardness. *Acta Mater.* **2009**, *57*, 1281–1289. [CrossRef]
161. Ren, X.J.; Hooper, R.M.; Griffiths, C.; Henshall, J.L. Indentation-size effects in single-crystal MgO. *Philos. Mag. A* **2002**, *82*, 2113–2120. [CrossRef]
162. Richter, A.; Wolf, B.; Nowicki, M.; Usov, I.O.; Valdez, J.A.; Sickafus, K. Multi-cycling nanoindentation in MgO single crystal before and after ion irradiation. *J. Appl. Phys. D Appl. Phys.* **2006**, *39*, 3342–3349. [CrossRef]
163. Bahr, D.F.; Kramer, D.E.; Gerberich, W.W. Non-linear deformation mechanisms during nanoindentation. *Acta Mater.* **1998**, *46*, 3605–3617. [CrossRef]
164. Chiu, Y.L.; Ngan, A.H.W. Time-dependent characteristics of incipient plasticity in nanoindentation of a Ni_3Al single crystal. *Acta Mater.* **2002**, *50*, 1599–1611. [CrossRef]
165. Gerberich, W.W.; Nelson, J.C.; Lilleodden, E.T.; Anderson, P.; Wyrobek, J.T. Indentation induced dislocation nucleation: The initial yield point. *Acta Mater.* **1996**, *44*, 3585–3598. [CrossRef]
166. Page, T.F.; Oliver, W.C.; McHargue, C.J. Deformation behavior of ceramic crystals subjected to very low load (nano)indentations. *J. Mater. Res.* **1992**, *7*, 450–473. [CrossRef]
167. Schuh, C.A.; Mason, J.K.; Lund, A.C. Quantitative insight into dislocation nucleation from high-temperature nanoindentation experiments. *Nat. Mater.* **2005**, *4*, 617–621. [CrossRef] [PubMed]
168. Tymiak, N.I.; Daugela, A.; Wyrobek, T.J.; Warren, O.L. Acoustic emission monitoring of the earliest stages of contact-induced plasticity in sapphire. *Acta Mater.* **2004**, *52*, 553–563. [CrossRef]
169. Kelchner, C.L.; Plimpton, S.J.; Hamilton, J.C. Dislocation nucleation and defect structure during surface indentation. *Phys. Rev. B* **1998**, *58*, 11085–11088. [CrossRef]
170. Van Vliet, K.; Li, J.; Zhu, T.; Yip, S.; Suresh, S. Quantifying the early stages of plasticity through nanoscale experiments and simulations. *Phys. Rev. B* **2003**, *67*, 104105. [CrossRef]
171. Lilleodden, E.T.; Zimmerman, J.A.; Foiles, S.M.; Nix, W.D. Atomistic simulations of elastic deformation and dislocation nucleation during nanoindentation. *J. Mech. Phys. Solids* **2003**, *51*, 901–920. [CrossRef]
172. Gaillard, Y.; Tromas, C.; Woirgard, J. Pop-in phenomenon in MgO and LiF: Observation of dislocation structures. *Philos. Mag. Lett.* **2003**, *83*, 553–561. [CrossRef]
173. Hertz, H. Über die Berührung fester elastischer Körper. *J. Reine Angew. Mat.* **1882**, *92*, 156–171.
174. Johnson, K.L. *Contact Mechanics*; Cambridge University Press: Cambridge, UK, 1987.

WD EX1058
Western Digital v IP Bridge
Page 48

175. Hanson, M.T.; Johnson, T. Elastic field for spherical Hertzian contact of isotropic bodies revisited. Some alternative expressions. *J. Tribol.* **1993**, *115*, 327–332. [CrossRef]
176. Booth, A.S.; Ellis, M.; Roberts, S.G.; Hirsch, P.B. Dislocation-controlled stable crack growth in Mo and MgO. *Mater. Sci. Eng. A* **1993**, *164*, 270–274. [CrossRef]
177. Burns, S.J.; Webb, W.W. Fracture surface energies and dislocation processes during dynamical cleavage of LiF. I. Theory. *J. Appl. Phys.* **1970**, *41*, 2078–2085. [CrossRef]
178. Burns, S.J.; Webb, W.W. Fracture surface energies and dislocation processes during dynamical cleavage of LiF. II. Experiments. *J. Appl. Phys.* **1970**, *41*, 2086–2095. [CrossRef]
179. Gilman, J.J. Nucleation of dislocation loops by cracks in crystals. *J. Metall.* **1957**, *9*, 449–454. [CrossRef]
180. Gilman, J.J.; Knudsen, C.; Walsh, W.P. Cleavage cracks and dislocations in LiF crystals. *J. Appl. Phys.* **1958**, *29*, 601–607. [CrossRef]
181. Robins, J.L.; Rhodin, T.N.; Gerlach, R.L. Dislocation structures in cleaved magnesium oxide. *J. Appl. Phys.* **1966**, *37*, 3893–3903. [CrossRef]
182. Montagne, A.; Audurier, V.; Tromas, C. Influence of pre-existing dislocations on the pop-in phenomenon during nanoindentation in MgO. *Acta Mater.* **2013**, *61*, 4778–4786. [CrossRef]
183. Gaillard, Y.; Tromas, C.; Woirgard, J. Quantitative analysis of dislocation pile-ups nucleated during nanoindentation in MgO. *Acta Mater.* **2006**, *54*, 1409–1417. [CrossRef]
184. Jouiad, M.; Pettinari, F.; Coujou, A.; Clément, N. Evaluation of friction stresses in the γ phase of a nickel-base superalloy "In situ" deformation experiments. *Mater. Sci. Eng. A* **1997**, *234–236*, 1041–1044. [CrossRef]
185. Bridgman, P.W.; Simon, I. Effects of Very High Pressures on Glass. *J. Appl. Phys.* **1953**, *24*, 405–413. [CrossRef]
186. Paterson, M.S.; Wong, T. *Experimental Rock Deformation-the Brittle Field*; Springer: Berlin, Germany, 2005.
187. Zambaldi, C.; Zehnder, C.; Raabe, D. Orientation dependent deformation by slip and twinning in magnesium during single crystal indentation. *Acta Mater.* **2015**, *91*, 267–288. [CrossRef]
188. Lloyd, S.J.; Molina-Aldareguia, J.M.; Clegg, W.J. Deformation under nanoindents in sapphire, spinel and magnesia examined using transmission electron microscopy. *Philos. Mag. A* **2002**, *82*, 1963–1969. [CrossRef]
189. McLaughlin, K.K. *TEM Diffraction Analysis of the Deformation Underneath Low Load Indentations*; University of Cambridge: Cambridge, UK, 2007.
190. Howie, P.R.; Korte, S.; Clegg, W.J. Fracture modes in micropillar compression of brittle crystals. *J. Mater. Res.* **2011**, *27*, 141–151. [CrossRef]
191. Uchic, M.D.; Dimiduk, D.M.; Florando, J.N.; Nix, W.D. Sample Dimensions Influence Strength and Crystal Plasticity. *Science* **2004**, *305*, 986–989. [CrossRef] [PubMed]
192. Uchic, M.D.; Shade, P.A.; Dimiduk, D.M. Plasticity of Micrometer-Scale Single Crystals in Compression. *Annu. Rev. Mater. Res.* **2009**, *39*, 361–386. [CrossRef]
193. Östlund, F.; Howie, P.R.; Ghisleni, R.; Korte, S.; Leifer, K.; Clegg, W.J.; Michler, J. Ductile–brittle transition in micropillar compression of GaAs at room temperature. *Philos. Mag. A* **2011**, *91*, 1190–1199. [CrossRef]
194. Kendall, K. Impossibility of comminuting small particles by compression. *Nature* **1978**, *272*, 710–711. [CrossRef]
195. Östlund, F.; Rzepiejewska-Malyska, K.; Leifer, K.; Hale, L.M.; Tang, Y.; Ballarini, R.; Gerberich, W.W.; Michler, J. Brittle-to-Ductile Transition in Uniaxial Compression of Silicon Pillars at Room Temperature. *Adv. Funct. Mater.* **2009**, *19*, 2439–2444. [CrossRef]
196. Cottrell, P.A.H. Lectures. 1961. Available online: https://link.springer.com/article/10.1007%2FBF00812985 (accessed on 29 March 2018).
197. Korte, S.; Barnard, J.S.; Stearn, R.J.; Clegg, W.J. Deformation of silicon–insights from microcompression testing at 25–500 C. *Int. J. Plasticity* **2011**, *27*, 1853–1866. [CrossRef]
198. Korte, S.; Clegg, W.J. Micropillar compression of ceramics at elevated temperatures. *Scr. Mater.* **2009**, *60*, 807–810. [CrossRef]
199. Uchic, M.; Shade, P.; Dimiduk, D. Micro-compression testing of fcc metals: A selected overview of experiments and simulations. *J. Miner. Metals Mater. Soc.* **2009**, *61*, 36–41. [CrossRef]
200. Korte-Kerzel, S. Microcompression of brittle and anisotropic crystals: Recent advances and current challenges in studying plasticity in hard materials. *MRS Commun.* **2017**, *7*, 109–120. [CrossRef]
201. Korte, S.; Clegg, W. Discussion of the dependence of the effect of size on the yield stress in hard materials studied by microcompression of MgO. *Philos. Mag. A* **2011**, *91*, 1150–1162. [CrossRef]

202. Zou, Y. Materials selection in micro- or nano-mechanical design: Towards new Ashby plots for small-sized materials. *Mat. Sci. Eng. A* **2017**, *680*, 421–425. [CrossRef]
203. Gibson, J.S.K.L.; Rezaei, S.; Rueß, H.; Hans, M.; Music, D.; Wulfinghoff, S.; Schneider, J.M.; Reese, S.; Korte-Kerzel, S. From quantum to continuum mechanics: Studying the fracture toughness of transition metal nitrides and oxynitrides. *Mater. Res. Lett.* **2017**, *6*, 142–151. [CrossRef]
204. Armstrong, D.E.J.; Hardie, C.D.; Gibson, J.S.K.L.; Bushby, A.J.; Edmondson, P.D.; Roberts, S.G. Small-scale characterisation of irradiated nuclear materials: Part II nanoindentation and micro-cantilever testing of ion irradiated nuclear materials. *J. Nucl. Mater.* **2015**, *462*, 374–381. [CrossRef]
205. Korte-Kerzel, S.; Schnabel, V.; Clegg, W.J.; Heggen, M. Room temperature plasticity in m-$Al_{13}Co_4$ studied by microcompression and high resolution scanning transmission electron microscopy. *Scr. Mater.* **2018**, *146*, 327–330. [CrossRef]
206. Korte, S.; Ritter, M.; Jiao, C.; Midgley, P.; Clegg, W. Three-dimensional electron backscattered diffraction analysis of deformation in MgO micropillars. *Acta Mater.* **2011**, *59*, 7241–7254. [CrossRef]
207. Zou, Y.; Spolenak, R. Size-dependent plasticity in micron- and submicron-sized ionic crystals. *Philos. Mag. Lett.* **2013**, *93*, 431–438. [CrossRef]
208. Kraft, O.; Gruber, P.A.; Mönig, R. Plasticity in confined dimensions. *Annu. Rev. Mater. Res.* **2010**, *40*, 293–317. [CrossRef]
209. Kiener, D.; Minor, A.M. Source Truncation and Exhaustion: Insights from Quantitative in situ TEM Tensile Testing. *Nano Lett.* **2011**, *11*, 3816–3820. [CrossRef] [PubMed]
210. Kaufmann, D.; Mönig, R.; Volkert, C.A.; Kraft, O. Size dependent mechanical behaviour of tantalum. *Int. J. Plasticity* **2011**, *27*, 470–478. [CrossRef]
211. Michler, J.; Wasmer, K.; Meier, S.; Östlund, F.; Leifer, K. Plastic deformation of gallium arsenide micropillars under uniaxial compression at room temperature. *Appl. Phys. Lett.* **2007**, *90*, 043123. [CrossRef]
212. Parthasarathy, T.A.; Rao, S.I.; Dimiduk, D.M.; Uchic, M.D.; Trinkle, D.R. Contribution to size effect of yield strength from the stochastics of dislocation source lengths in finite samples. *Scr. Mater.* **2007**, *56*, 313–316. [CrossRef]
213. Schneider, A.S.; Frick, C.P.; Arzt, E.; Clegg, W.J.; Korte, S. Influence of test temperature on the size effect in molybdenum small-scale compression pillars. *Philos. Mag. Lett.* **2013**, *93*, 331–338. [CrossRef]
214. Torrents Abad, O.; Wheeler, J.M.; Michler, J.; Schneider, A.S.; Arzt, E. Temperature-dependent size effects on the strength of Ta and W micropillars. *Acta Mater.* **2016**, *103*, 483–494. [CrossRef]
215. Soler, R.; Molina-Aldareguia, J.M.; Segurado, J.; LLorca, J.; Merino, R.I.; Orera, V.M. Micropillar compression of LiF [112] single crystals: Effect of size, ion irradiation and misorientation. *Int. J. Plasticity* **2012**, *36*, 50–63. [CrossRef]
216. Kiener, D.; Motz, C.; Dehm, G. Micro-compression testing: A critical discussion of experimental constraints. *Mater. Sci. Eng. A* **2009**, *505*, 79–87. [CrossRef]
217. Zou, Y.; Spolenak, R. Size-dependent plasticity in KCl and LiF single crystals: influence of orientation, temperature, pre-straining and doping. *Philos. Mag. A* **2015**, 1–19. [CrossRef]
218. Gibson, J.S.K.L.; Schröders, S.; Zehnder, C.; Korte-Kerzel, S. On extracting mechanical properties from nanoindentation at temperatures up to 1000°C. *Extreme Mech. Lett.* **2017**, *17*, 43–49. [CrossRef]
219. Kang, W.; Merrill, M.; Wheeler, J.M. In situ thermomechanical testing methods for micro/nano-scale materials. *Nano* **2017**, *9*, 2666–2688. [CrossRef] [PubMed]
220. Durst, K.; Maier, V. Dynamic nanoindentation testing for studying thermally activated processes from single to nanocrystalline metals. *Curr. Opin. Solid State Mater. Sci.* **2015**, *19*, 340–353. [CrossRef]
221. Maier, V.; Durst, K.; Mueller, J.; Backes, B.; Höppel, H.W.; Göken, M. Nanoindentation strain-rate jump tests for determining the local strain-rate sensitivity in nanocrystalline Ni and ultrafine-grained Al. *J. Mater. Res.* **2011**, *26*, 1421–1430. [CrossRef]
222. Moser, B.; Wasmer, K.; Barbieri, L.; Michler, J. Strength and fracture of Si micropillars: A new scanning electron microscopy-based micro-compression test. *J. Mater. Res.* **2007**, *22*, 1004–1011. [CrossRef]
223. Bei, H.; Shim, S.; George, E.P.; Miller, M.K.; Herbert, E.G.; Pharr, G.M. Compressive strengths of molybdenum alloy micro-pillars prepared using a new technique. *Scr. Mater.* **2007**, *57*, 397–400. [CrossRef]
224. Issa, I.; Amodeo, J.; Réthoré, J.; Joly-Pottuz, L.; Esnouf, C.; Morthomas, J.; Perez, M.; Chevalier, J.; Masenelli-Varlot, K. In situ investigation of MgO nanocube deformation at room temperature. *Acta Mater.* **2015**, *86*, 295–304. [CrossRef]

WD EX1058
Western Digital v IP Bridge
Page 50

225. Maaß, R.; Meza, L.; Gan, B.; Tin, S.; Greer, J.R. Ultrahigh strength of dislocation-free Ni3Al nanocubes. *Small* **2012**, *8*, 1869–1875. [CrossRef] [PubMed]
226. Amodeo, J.; Lizoul, K. Mechanical properties and dislocation nucleation in nanocrystals with blunt edges. *Mater. Des.* **2017**, *135*, 223–231. [CrossRef]
227. Nishiyama, N.; Katsura, T.; Funakoshi, K.-I.; Kubo, A.; Kubo, T.; Tange, Y.; Sueda, Y.-I.; Yokoshi, S. Determination of the phase boundary between the B1 and B2 phases in NaCl by in situx-ray diffraction. *Phys. Rev. B Condens. Matter* **2003**, *68*, 319. [CrossRef]
228. Mao, H.K.; Wu, Y.; Hemley, R.J.; Chen, L.C.; Shu, J.F.; Finger, L.W.; Cox, D.E. High-pressure phase transition and equation of state of CsI. *Phys. Rev. Lett.* **1990**, *64*, 1749–1752. [CrossRef] [PubMed]
229. Williams, Q.; Jeanloz, R. Measurements of CsI band-gap closure to 93 GPa. *Phys. Rev. Lett.* **1986**, *56*, 163–164. [CrossRef] [PubMed]
230. Jeanloz, R. Physical Chemistry at Ultrahigh Pressures and Temperatures. *Ann. Rev. Phys. Chem.* **1989**, *40*, 237–259. [CrossRef]
231. McWilliams, R.S.; Spaulding, D.K.; Eggert, J.H.; Celliers, P.M.; Hicks, D.G.; Smith, R.F.; Collins, G.W.; Jeanloz, R. Phase Transformations and Metallization of Magnesium Oxide at High Pressure and Temperature. *Science* **2012**, *338*, 1330–1333. [CrossRef] [PubMed]
232. Coppari, F.; Smith, R.F.; Eggert, J.H.; Wang, J.; Rygg, J.R.; Lazicki, A.; Hawreliak, J.A.; Collins, G.W.; Duffy, T.S. Experimental evidence for a phase transition in magnesium oxide at exoplanet pressures. *Nat. Geosci.* **2013**, *6*, 926–929. [CrossRef]
233. Karki, B.; Stixrude, L.; Clark, S.; Warren, M.; Ackland, G.; Crain, J. Structure and elasticity of MgO at high pressure. *Am. Mineral.* **1997**, *82*, 51–60. [CrossRef]
234. Karato, S.-I. Some remarks on the origin of seismic anisotropy in the D" layer. *Earth Planets Space* **1998**, *50*, 1019–1028. [CrossRef]
235. Wang, Y.; Durham, W.; Getting, I.; Weidner, D. The deformation-DIA: A new apparatus for high temperature triaxial deformation to pressures up to 15 GPa. *Rev. Sci. Instrum.* **2003**, *74*, 3002–3011. [CrossRef]
236. Yamazaki, D.; Karato, S. High-pressure rotational deformation apparatus to 15 GPa. *Rev. Sci. Instrum.* **2001**, *72*, 4207–4211. [CrossRef]
237. Hunt, S.A.; Weidner, D.J.; McCormack, R.J.; Whitaker, M.L.; Bailey, E.; Li, L.; Vaughan, M.T.; Dobson, D.P. Deformation T-Cup: A new multi-anvil apparatus for controlled strain-rate deformation experiments at pressures above 18 GPa. *Rev. Sci. Instrum.* **2014**, *85*, 085103. [CrossRef] [PubMed]
238. Kawazoe, T.; Ohuchi, T.; Nishihara, Y.; Nishiyama, N.; Fujino, K.; Irifune, T. Seismic anisotropy in the mantle transition zone induced by shear deformation of wadsleyite. *Phys. Earth Planet. Int.* **2013**, *216*, 91–98. [CrossRef]
239. Girard, J.; Amulele, G.; Farla, R.; Mohiuddin, A.; Karato, S.I. Shear deformation of bridgmanite and magnesiowustite aggregates at lower mantle conditions. *Science* **2016**, *351*, 144–147. [CrossRef] [PubMed]
240. Raterron, P.; Merkel, S.; Holyoke, C.W. Axial temperature gradient and stress measurements in the deformation-DIA cell using alumina pistons. *Rev. Sci. Instrum.* **2013**, *84*, 043906. [CrossRef] [PubMed]
241. Xu, Y.; Nishihara, Y.; Karato, S.-I. Development of a rotational Drickamer apparatus for large-strain deformation experiments at deep Earth conditions. In *Advances in High-Pressure Technology for Geophysical Applications*; Chen, J., Wang, Y., Duffy, T.S., Shen, G., Dobrzhinetskaya, L.F., Eds.; Elsevier: Amsterdam, The Netherlands, 2005; pp. 167–182.
242. Dubrovinskaia, N.; Dubrovinsky, L.; Solopova, N.A.; Abakumov, A.; Turner, S.; Hanfland, M.; Bykova, E.; Bykov, M.; Prescher, C.; Prakapenka, V.B.; et al. Terapascal static pressure generation with ultrahigh yield strength nanodiamond. *Sci. Adv.* **2016**, *2*, e1600341. [CrossRef] [PubMed]
243. Tateno, S.; Hirose, K.; Ohishi, Y.; Tatsumi, Y. The Structure of Iron in Earth's Inner Core. *Science* **2010**, *330*, 359–361. [CrossRef] [PubMed]
244. Hemley, R.J.; Mao, H.K.; Shen, G.; Badro, J.; Gillet, P.; Hanfland, M.; Häusermann, D. X-ray imaging of stress and strain of diamond, iron, and tungsten at megabar pressures. *Science* **1997**, *276*, 1242–1245. [CrossRef]
245. Liermann, H.P.; Merkel, S.; Miyagi, L.; Wenk, H.R.; Shen, G.; Cynn, H.; Evans, W.J. New Experimental Method for In Situ Determination of Material Textures at Simultaneous High-Pressure and Temperature by Means of Radial Diffraction in the Diamond Anvil Cell. *Rev. Sci. Instrum.* **2009**, *80*, 104501. [CrossRef] [PubMed]

246. Hirose, K.; Nagaya, Y.; Merkel, S.; Ohishi, Y. Deformation of $MnGeO_3$ post-perovskite at lower mantle pressure and temperature. *Geophys. Res. Lett.* **2010**, *37*, L20302. [CrossRef]
247. Merkel, S. X-ray diffraction evaluation of stress in high pressure deformation experiments. *J. Phys. Condens. Matter* **2006**, *18*, S949–S962. [CrossRef] [PubMed]
248. Meade, C.; Jeanloz, R. Yield strength of MgO to 40 GPa. *J. Geophys. Res.* **1988**, *93*, 3261–3269. [CrossRef]
249. Vaughan, M.; Chen, J.; Li, L.; Weidner, D.; Li, B. *Use of X-ray Imaging Techniques at High Pressure and Temperature for Strain Measurements*; Manghnani, M.H., Nellis, W.J., Nicol, M.F., Eds.; Universities Press (India) Limited: Hyderabad, India, 2000; pp. 1097–1098.
250. Merkel, S.; Yagi, T. X-ray transparent gasket for diamond anvil cell high pressure experiments. *Rev. Sci. Instrum.* **2005**, *76*, 046109. [CrossRef]
251. Noyan, I.C.; Cohen, J.B. *Residual Stress: Measurements by Diffraction and Interpretation*; Springer-Verlag: New York, NY, USA, 1987.
252. Merkel, S.; Wenk, H.R.; Shu, J.; Shen, G.; Gillet, P.; Mao, H.K.; Hemley, R.J. Deformation of polycrystalline MgO at pressures of the lower mantle. *J. Geophys. Res.* **2002**, *107*, 2271. [CrossRef]
253. Lin, F.; Hilairet, N.; Raterron, P.; Addad, A.; Immoor, J.; Marquardt, H.; Tomé, C.N.; Miyagi, L.; Merkel, S. Elasto-viscoplastic self consistent modeling of the ambient temperature plastic behavior of periclase deformed up to 5.4 GPa. *J. Appl. Phys.* **2017**, *122*, 205902. [CrossRef]
254. Singh, A.K.; Balasingh, C.; Mao, H.K.; Hemley, R.J.; Shu, J. Analysis of lattice strains measured under non-hydrostatic pressure. *J. Appl. Phys.* **1998**, *83*, 7567–7575. [CrossRef]
255. Li, L. X-ray strain analysis at high pressure: Effect of plastic deformation in MgO. *J. Appl. Phys.* **2004**, *95*, 8357–8365. [CrossRef]
256. Merkel, S.; Tomé, C.N.; Wenk, H.R. A modeling analysis of the influence of plasticity on high pressure deformation of hcp-Co. *Phys. Rev. B* **2009**, *79*, 064110. [CrossRef]
257. Amodeo, J.; Dancette, S.; Delannay, L. Atomistically-informed crystal plasticity in MgO polycrystals under pressure. *Int. J. Plasticity* **2016**, *82*, 177–191. [CrossRef]
258. Roters, F.; Eisenlohr, P.; Hantcherli, L.; Tjahjanto, D.D.; Bieler, T.R.; Raabe, D. Overview of constitutive laws, kinematics, homogenization and multiscale methods in crystal plasticity finite-element modeling: Theory, experiments, applications. *Acta Mater.* **2010**, *58*, 1152–1211. [CrossRef]
259. Cordier, P. Dislocations and slip systems of mantle minerals. In *Pastic Deformation of Minerals and Rocks*; Karato, S., Wenk, H.R., Eds.; Reviews in Mineralogy and Geochemistry; Mineralogical Society of America: Chantilly, VA, USA, 2002; Volume 51, pp. 137–179.
260. Mussi, A.; Cordier, P.; Demouchy, S.; Hue, B. Hardening mechanisms in olivine single crystal deformed at 1090 °C: an electron tomography study. *Philos. Mag.* **2017**, *97*, 3172–3185. [CrossRef]
261. Amodeo, J.; Carrez, P.; Cordier, P. Modelling the effect of pressure on the critical shear stress of MgO single crystals. *Philos. Mag. A* **2012**, *92*, 1523–1541. [CrossRef]
262. Girard, J.; Chen, J.; Raterron, P. Deformation of periclase single crystals at high pressure and temperature: Quantification of the effect of pressure on slip-system activities. *J. Appl. Phys.* **2012**, *111*, 112607. [CrossRef]
263. Weidner, D.J.; Li, L.; Davis, M.; Chen, J. Effect of plasticity on elastic modulus measurements. *Geophys. Res. Lett.* **2004**, *31*, L06621. [CrossRef]
264. Yamazaki, D.; Karato, S. Fabric development in (Mg, Fe) O during large strain, shear deformation: implications for seismic anisotropy in Earth's lower mantle. *Phys. Earth Planet. Inter.* **2002**, *131*, 251–267. [CrossRef]
265. Tommaseo, C.E.; Devine, J.; Merkel, S.; Speziale, S.; Wenk, H.R. Texture development and elastic stresses in magnesiowustite at high pressure. *Phys. Chem. Miner.* **2006**, *33*, 84–97. [CrossRef]
266. Badro, J.; Fiquet, G.; Guyot, F.; Rueff, J.-P.; Struzhkin, V.V.; Vankó, G.; Monaco, G. Iron partitioning in Earth's mantle: toward a deep lower mantle discontinuity. *Science* **2003**, *300*, 789–791. [CrossRef] [PubMed]
267. Lin, J.F.; Wenk, H.R.; Voltolini, M.; Speziale, S.; Shu, J.; Duffy, T.S. Deformation of lower-mantle ferropericlase (Mg,Fe)O across the electronic spin transition. *Phys. Chem. Min.* **2009**, *36*, 585–592. [CrossRef]
268. Long, M.D.; Xiao, X.; Jiang, Z.; Evansa, B.; Karato, S. Lattice preferred orientation in deformed polycrystalline (Mg,Fe)O and implications for seismic anisotropy in D''. *Phys. Earth Planet. Inter.* **2006**, *156*, 75–88. [CrossRef]
269. Heidelbach, F.; Stretton, I.; Langenhorst, F.; Mackwell, S. Fabric evolution during high shear strain deformation of magnesiowüstite ($Mg_{0.8}Fe_{0.2}O$). *J. Geophys. Res.* **2003**, *108*, 2154. [CrossRef]

270. Immoor, J.; Marquardt, H.; Miyagi, L.; Lin, F.; Speziale, S.; Merkel, S.; Buchen, J.; Kurnosov, A.; Liermann, H.P. Evidence for {100}<011> slip in ferropericlase in Earth's lower mantle from high-pressure/high-temperature experiments. *Earth. Planet. Sci. Lett.* **2018**, *489*, 251–257. [CrossRef]
271. Weaver, C.W.; Paterson, M.S. Deformation of cube-oriented MgO crystals under pressure. *J. Am. Ceram. Soc.* **1969**, *52*, 293–302. [CrossRef]
272. Paterson, M.; Weaver, C. Deformation of polycrystalline MgO under pressure. *J. Am. Ceram. Soc.* **1970**, *53*, 463–471. [CrossRef]
273. Mei, S.; Kohlstedt, D.L.; Durham, W.B.; Wang, L. Experimental investigation of the creep behavior of MgO at high pressures. *Phys. Earth Planet. Inter.* **2008**, *170*, 170–175. [CrossRef]
274. Weidner, D.J.; Wang, Y.B.; Vaughan, M.T. Yield Strength at High-Pressure and Temperature. *Geophys. Res. Lett.* **1994**, *21*, 753–756. [CrossRef]
275. Uchida, T.; Funamori, N.; Ohtani, T.; Yagi, T. *Differential Stress of MgO and Mg2SiO4 under Uniaxial Stress Field: Variation with Pressure, Temperature, and Phase Transition*; Trzeciatowski, W.A., Ed.; World Scientific Publishing: Singapore, 1996; pp. 183–185.
276. Uchida, T.; Wang, Y.; Rivers, M.L.; Sutton, S.R. Yield strength and strain hardening of MgO up to 8 GPa measured in the deformation-DIA with monochromatic X-ray diffraction. *Earth. Planet. Sci. Lett.* **2004**, *226*, 117–126. [CrossRef]
277. Weidner, D.J.; Li, L. Measurement of stress using synchrotron X-rays. *J. Phys. Condens. Matter* **2006**, *18*, S1061–S1067. [CrossRef] [PubMed]
278. Singh, A.K.; Liermann, H.P.; Saxena, S.K. Strength of magnesium oxide under high pressure: Evidence for the grain-size dependence. *Solid State Commun.* **2004**, *132*, 795–798. [CrossRef]
279. Marquardt, H.; Miyagi, L. Slab stagnation in the shallow lower mantle linked to an increase in mantle viscosity. *Nat. Geosci.* **2015**, *8*, 311–314. [CrossRef]
280. Kinsland, G.; Bassett, W. Strength of MgO and NaCl polycrystals to confining pressures of 250 kbar at 25 C. *J. Appl. Phys.* **1977**, *48*, 978–985. [CrossRef]
281. Duffy, T.; Hemley, R.; Mao, H. Equation of state and shear strength at multimegabar pressures: Magnesium oxide to 227 GPa. *Phys. Rev. Lett.* **1995**, *74*, 1371–1374. [CrossRef] [PubMed]
282. Reynard, B.; Caracas, R.; Cardon, H.; Montagnac, G.; Merkel, S. High-pressure yield strength of rocksalt structures using quartz Raman piezometry. *C. R. Geosci.*. in press. [CrossRef]
283. Li, L.; Weidner, D.J. In situ analysis of texture development from sinusoidal stress at high pressure and temperature. *Rev. Sci. Instrum.* **2015**, *86*, 125106. [CrossRef] [PubMed]

© 2018 by the authors. Licensee MDPI, Basel, Switzerland. This article is an open access article distributed under the terms and conditions of the Creative Commons Attribution (CC BY) license (http://creativecommons.org/licenses/by/4.0/).